Argelander Institut für Astronomie der Universität Bonn

Old Globular Clusters in Dwarf Irregular Galaxies

Dissertation

zur

Erlangung des Doktorgrades (Dr. rer. nat.)

der

Mathematisch-Naturwissenschaftlichen Fakultät

der

Rheinischen Friedrich-Wilhelms-Universität Bonn

vorgelegt von

Iskren Y. Georgiev

aus

Bulgarien

Bonn, July 2008

Angefertigt mit Genehmigung der Mathematisch-Naturwissenschaftlichen Fakultät der Rheinischen Friedrich-Wilhelms-Universität Bonn

1. Referent: Prof. Dr. Klaas S. de Boer
2. Referent: Prof. Dr. Pavel Kroupa

Tag der Promotion: 17.9.2008

Diese Dissertation ist auf dem Hochschulschriftenserver der ULB Bonn
unter http://hss.ulb.uni-bonn.de/diss_online elektronisch publiziert.

Erscheinungsjahr 2008

"We are star-stuff",
Carl Sagan

To my caring family

Summary

One of the most pressing questions in astrophysics to date is resolving the history of galaxy assembly and their subsequent evolution. In the currently popular "hierarchical merging" scenario, massive galaxies are believed to grow via numerous galaxy mergers. Present day dwarf irregular (dIrr) galaxies are widely regarded as the pristine analogs being the closest to resemble those pre-galactic building blocks. One way to approach this question is through studying the oldest stellar population in a given galaxy, and in particular the ancient globular star clusters whose properties unveil the conditions at the time of their early formation.

To address the question of galaxy assembly the current work deals with studying the old globular clusters (GCs) in dIrr galaxies. By comparing the characteristics of GCs in massive galaxies an attempt is made to quantify the contribution of dIrr galaxies to the assembly of massive present-day galaxies and their globular cluster systems (GCSs). In particular, the Galactic GCS is known to harbor sub-populations of GCs whose properties (colors, luminosities, horizontal branch morphologies, structural parameters and orbital kinematics) suggest that they might have formed in low-mass satellites and were later incorporated into the Milky Way GCS.

A starting point of my PhD thesis was to see if the GC formation in dIrrs is influenced by the cluster environment. Therefore, based on deep multi-wavelength observations with the eight meter "European Southern Observatory" (ESO) "Very Large Telescope" (VLT) with the FORS1 instrument in $U, B, V, I, H\,\alpha$ and J filters, we studied the old GCs of the Magellanic-type dIrr galaxy NGC 1427A in the central regions of Fornax galaxy cluster.

We showed (Georgiev et al. 2006, and presented in Chapter 1) that this galaxy, which is as massive as the Large Magellanic Cloud (LMC), hosts $\sim 38 \pm 8$ old metal-poor GCs, more than two times more than the equally massive Large Magellanic Cloud (LMC). This translates into a present-day GC specific frequency $S_N = 1.6 \pm 0.23$, which is significantly higher than $S_N \sim 0.5$ for Local Group dIrrs. Therefore, the increased S_N value in galaxies in dense environments versus the low S_N values for galaxies of similar mass in low-density group environments might be the effect of the dense cluster environment. This finding was recently confirmed by Peng et al. (2008) studying 100 early-type giant and dwarf galaxies in the Virgo galaxy cluster. They showed that galaxies closer to the cluster center tend to have higher GC mass fractions. Another result of our study came from the contamination analysis which indicated that the density distribution of GCs in the outskirts of the Fornax central cD galaxy NGC 1399 may not be spherically symmetric. This was proved to be the case (Firth et al. 2007) by the spectroscopically obtained radial velocity distribution of NGC 1399 and NGC 1427A GCs.

Since NGC 1427A resides in a dense cluster environment a necessary comparison,

in order to access the impact of the environment, is to study the GCSs of dIrrs in "field" environments. Taking advantage of the supreme resolution of the "Advanced Camera for Surveys" (ACS) on board "Hubble Space Telescope" (HST) to probe down to three magnitudes beyond the expected GC luminosity function (GCLF) turnover magnitude $M_{V,TO}$, we have performed a search for old GCs in 70 dIrrs on archival $F606W$ and $F814W$ images (results are published in Georgiev et al. (2008a) and in Georgiev et al. (2008c), in prep., and presented in Chapter 3). The entire sample consists of 55 dIrrs, 3 dEs, 5 dSphs and 5 low-mass late-type dwarf spirals). Those galaxies reside in nearby (2 - 8 Mpc) associations containing only dwarf galaxies or in the remote halo regions of the galaxy group. All galaxies have absolute magnitudes fainter than or equal to the Small Magellanic Cloud (SMC) ($M_V = -16.2$ mag). NGC 121 is the only old ($\sim$ 11 Gyr, Glatt et al. 2008) GC in the SMC, which is about one magnitude brighter ($M_V = -8.33$ mag) than the typical GCLF turnover magnitude. Hence, one would expect to find, on average, no more than one GC in each of these galaxies. However, we detect old GC candidates (GCCs) in 30 dIrrs, 2 dEs, 2 dSphs and in 4 Sms.

In the studied galaxies we found in total 175 GC candidates, being old and metal-poor according to their colors and magnitudes. The total sample contains 97 metal-poor "blue" ($0.7 < (V-I)_0 < 1.0$ mag) GCs (bGCs), 63 red ($1.0 < (V-I)_0 < 1.0$ mag) GCs (rGCs) and the rest are very likely background contaminants. The total number of GCCs in our sample dIrrs is 119, of which 64 bGCs, 42 rGCs; in dEs/dSphs GCCs sums up to 31, with 21 bGCs and 10 rGCs; the low-mass late-type spirals contain 26 GCCs in total, 13 bGCs and 11 rGCs. The color distribution of all bGCs in dIrrs peaks at $(V-I) = 0.96$ mag and their luminosity function turnover peaks at $M_{V,TO} = -7.6$ mag, similar to that of the old LMC GCs. Gaussian fits to the histogram distributions of bGCs return $M_V = -7.53 \pm 0.17$ mag and $\sigma = 1.15 \pm 0.11$ for dIrrs, $M_V = -7.12 \pm 0.10$ mag and $\sigma = 1.09 \pm 0.11$ for dE/dSph, and $M_V = -7.41 \pm 0.08$ mag and $\sigma = 0.92 \pm 0.12$ for Sm galaxies. The general trend of $M_{V,TO}$ is such that it becomes fainter from late- to early-type galaxies and σ narrower (with the cautionary note of the low statistical confidence due to small numbers). Given the completeness tests performed, the brighter $M_{V,TO}$ for dwarf galaxies and the lack of faint blue GCs is not due to incompleteness and might reflect relatively young GC systems in these dIrrs. Hence, a subsequent stellar evolutionary fading will make the $M_{V,TO}$ fainter. Also the destructive dynamical processes (mass loss due to stellar evolution, relaxation, tidal shocking, encounters with giant molecular clouds) shaping the GC mass function have to be taken into account. These destroy preferentially low-mass clusters, an effect suggested to shape the GC characteristic mass function (e.g. Gnedin & Ostriker 1997; Fall & Zhang 2001; Kroupa & Boily 2002; Lamers et al. 2005; Lamers & Gieles 2006; Parmentier et al. 2008; Baumgardt et al. 2008; McLaughlin & Fall 2008). It is interesting to note that the cluster disruption time-scale varies with the ambient density and can be shorter in starburst regions where encounters with GMCs are shown to be very destructive (Lamers et al. 2005; Lamers & Gieles 2006).

We have discovered that nine dIrrs are nucleated harboring bright ($M_V \sim -8$ to -11 mag) central GCs, similar to nuclear clusters of dEs. These nuclear GCs have luminosity, color, and structural parameters similar to those of the peculiar Galactic clusters ω Cen and M 54, suggesting that the latter might have had their origin in

the central regions of similar Galactic building blocks as the dIrrs in this study. A comparison between half-light radii and ellipticities of bGCs in our sample, old GCs in the LMC and Galactic "Young Halo" (YH) GCs, suspected to have originated from similar dIrrs, is performed. The cluster half-light radius ($r_{\rm h}$) versus cluster mass plane shows a very similar distribution between bGCs in dIrrs, LMC GCs and YH clusters, which indicates evolution in similar environments. Comparison with theoretical models of cluster dissolution indicates that GCs in low-mass galaxies dynamically evolve mainly as self-gravitating systems, i.e. their $r_{\rm h}$ and M_{cl} primarily evolves due to internal processes, like two-body relaxation. GCs in dIrrs as well as in the old LMC GCs differ in their ellipticity distributions from Galactic GCs, being on average more flattened ($\bar{\epsilon} = 0.1$). Dynamical models of clusters evolving in isolation show that they reach this asymptotic ϵ value after few cluster relaxation times ($> 5t_{\rm rh}$). This is another indication that old GCs in low-mass galaxies are dynamically evolved stellar systems which evolved in a weak tidal environments.

Considering all the similarities found between old GCs in dIrrs and Galactic GCs with complex stellar populations (ω Cen, M 54, NGCs 2808, 6388, 6441 etc.) our results support the suggested accretion origin of a fraction of the Galactic GCs, later incorporated into the Galactic GCS. Quantitatively, we conclude that about 10 dwarf galaxies such as the dIrrs studied here are enough to populate the sub-population of 30 old metal-poor GCs in the halo of our Galaxy. In order for this scenario to apply to other massive and distant galaxies, where such a detailed comparison with their GCs is currently not possible, it is required that the accreted dwarfs have high specific frequencies such as to preserve the observed high ratio between metal-poor GCs and metal-poor field stars in massive galaxies. The high specific frequencies found by us and others in dIrrs (Seth et al. 2004; Georgiev et al. 2006, 2008a; Puzia & Sharina 2008) and in early-type dwarf ellipticals (Miller et al. 1998; Strader et al. 2006; Miller & Lotz 2007; Peng et al. 2008) is inline with this view. Thus, accretion of dwarf galaxies is a feasible mechanism which contributes to the build up of the blue (metal-poor) GCs in massive galaxies. Indeed, a manifestation of such accretion process are the observed high GC "specific frequencies" (the number of GCs per unit galaxy light) among massive and central cluster galaxies.

We showed that the behavior of increasing the number of GCs per unit luminosity or mass (including HI gas mass) of the host (the specific frequency/mass, S_N,S_M) with decreasing host galaxy mass holds irrespective of galaxy type. An apparent maximum and minimum bound for both S_N as a function of galaxy luminosity seems to be present. This will suggest that the maximum and minimum GC formation efficiency scales with galaxy luminosity/mass in the sense that lower-mass galaxies are more efficient in forming GCs per unit luminosity/mass of the host. When the S_M is considerd I find a relation which could be interpreted as a lower GC formation efficiency or GC survival limit, i.e. when a galaxy managed to form GCs of which at least one ($N_{\rm GC} = 1$ with mass $M_{\rm GCS} = 1\,[10^4\,{\rm M}_\odot]$) survived dissolution processes for a Hubble time. The already observed deviation from S_N bounds toward higher-mass galaxies can be accounted for by accretion or merger events with galaxies with lower masses and high S_N or S_M. McLaughlin (1999) found a constant GC formation efficiency (GCFE) across three massive galaxies (M 87, M 49 and NGC 1399) when gas and X-ray mass is taken into account. However, the dynamical range in our study is much larger and lower-mass galaxies are not reported to have significant

mass in hot X-ray gas, which suggests that the GCFE might scale with the star formation efficiency and host galaxy mass.

Our very intriguing finding of bright and massive GCs in the nuclear regions of dIrr galaxies provided us with the possibility to test the suggested accretion origin of the massive Galactic GCs such as ω Cen and M 54, the latter being the nucleus of the already accreted Sagittarius dwarf galaxy. In Chapter 4 I have outlined the future directions in my planned research, namely to probe the above hypothesis. I find that the escape velocity ($\nu_{\rm esc}$) required for matter to leave the cluster potential can be used as a promising indicator and proxy for the degree of cluster self-enrichment which is believed to be responsible for the observed age/metallicity spreads and hot horizontal branch stars in the peculiar sub-population of Galactic GCs. My preliminary work shows that $\nu_{\rm esc}$ correlates with the cluster metallicity for those peculiar GCs. I would like to test if a similar correlation holds for the nuclear GCs (nGCs) in our dIrrs sample. If so, this will add an additional match to the other properties in common between nGCs and the peculiar Galactic clusters, thus suggesting that both have formed/evolved under very similar initial conditions. Our analysis has shown that the cluster $\nu_{\rm esc}$-metallicity relation can provide an explanation (based on metal self-enrichment) for the observed and presently unsolved phenomenon of a mass-metallicity relation among the brightest and most massive GCs in the rich GCSs of massive galaxies.

Contents

List of Figures

List of Tables

Chapter 1

Old Globular Clusters in Dwarf Irregular Galaxies in Cluster Environments

Contents

1.1 Introduction

Old Globular Clusters (GCs) are complexes of stars which have been formed almost simultaneously out of material with basically the same initial chemical composition. They form during major star formation episodes in virtually every galaxy.Hence they are regarded as a fossil record of the initial conditions of the early host galaxy formation history.

With respect to the formation and/or assembly of early-type galaxies and their globular cluster systems (GCSs) three main competing scenarios emerged. The first assumes a hierarchical build-up of massive galaxies from a (large) population of pregalactic gaseous cloud fragments. In this scenario two major epochs of star formation occurred, with both the blue (metal-poor) and the red (metal-rich) GC populations formed *in situ* with a pause in between the two bursts of GC formation (Forbes et al. 1997). Another possibility,within the same scenario, is to have a long series of smaller star-forming events with the metal-poor clusters as first generation and the metal-rich ones formed in mini-mergers at high redshifts (Beasley et al. 2002). The second scenario regards major mergers of disk galaxies (Schweizer 1987; Ashman & Zepf 1992) in which the metal-poor GC population form early in "Searle-Zinn" fragments in the halos of the progenitor disk galaxies, while most of the metal-rich GCs form during later progenitor mergers, and thus are younger. The third scenario, dissipationless satellite accretion, assumes that the host galaxy forms by classical monolithic collapse and then accretes smaller galaxies (Côté et al. 1998). The GCs of these dwarf galaxies are being captured and/or tidally stripped (Hilker

et al. 1999; Côté et al. 2002). For a thorough discussion of the GCS formation scenarios we refer the reader to the reviews by Ashman & Zepf (1998); Carney & Harris (1998); Elmegreen (1999); Kissler-Patig (2000); van den Bergh (2000a) and Harris (2003).

In all these models, the GCSs of low-mass dwarf galaxies, the most numerous galaxy type in galaxy clusters (Sandage 2005, and references therein), are envisioned as the building blocks of the GCSs of the more massive galaxies. At present the role of the GCSs of dIrr galaxies in the frame of galaxy formation is unclear. A recent study by Sharina et al. (2005) compared the GCS properties of dE, dSph, and dIrr in field and group environments and found that all three dwarf galaxy types host a population of old GCs with very similar $(V-I)$ colors. The mean color of this population is almost identical to the $(V-I)$ colors of the blue GC population in massive early-type galaxies. One way to address the evolutionary connection between dE, dSph, dIrr, and massive galaxies is to study the specific frequency S_N (the number of GCs ($N_{\rm GC}$) normalized by the galaxy's luminosity, Harris & van den Bergh 1981, $S_N = N_{\rm GC}10^{0.4(M_V+15)}$) of such galaxies. Generally, the mean S_N values of dE, dSph, and dIrr galaxies in the Virgo and Fornax cluster are comparable (Seth et al. 2004) and very similar to S_N values of giant elliptical galaxies, which implies that all form GCs in the same proportion (per galaxy magnitude). However, the S_N of dwarf galaxies in clusters is significantly higher than for dE, dSph, and dIrr in the field environment (eg. $S_N = 0.5$ for LMC, Harris 1991). The mechanisms that drive the transition between the GCSs of field and cluster dwarf galaxies are unclear.

Here we study the globular cluster system of NGC 1427A, is the brightest dwarf irregular galaxy in the Fornax galaxy cluster. Throughout this work we adopt a distance modulus of $(m-M) = 31.39\pm0.20$ mag (19 ± 1.8 Mpc) to the Fornax cluster, as measured with Cepheids (HST Key Project, Freedman et al. 2001). NGC 1427A has a mean radial velocity of 2027.8 ± 0.8 km/s (Bureau et al. 1996), which is ~ 600 km/s higher than that of the cD elliptical NGC 1399 (1430 ± 9 km/s), located at the cluster center, and twice larger than the cluster velocity dispersion ($\sigma_v = 325$ km/s, Ferguson & Sandage 1990). Such a large peculiar velocity is shared also by other cluster members, such as NGC 1404, as shown by the double-peaked redshift distribution of the Fornax cluster and the distinct group of dwarf galaxies falling toward the cluster center (Drinkwater et al. 2001). NGC 1427A shows a ring-like pattern of star formation with prominent distinct starburst complexes ionizing their immediate surroundings. One of the first studies of NGC 1427A by Hilker et al. (1997), relying on its morphological appearance and the apparent proximity to the cluster center, suggested that the interaction with the cluster environment is responsible for the observed active star formation and its future morphological evolution. Cellone & Forte (1997) envisioned a collision with one of the many dwarf ellipticals populating the cluster center to be responsible for the ring-like appearance of NGC 1427A and speculated that the bright complex in the Northern part of the galaxy could be the intruder. A study by Chanamé et al. (2000) of the ionized gas kinematics of NGC 1427A showed that this Northern object shares the same general kinematical pattern as the rest of the galaxy body, hence making unlikely its external origin. They also argued that the most likely scenario explaining the morphological features of NGC 1427A is due to its passage through the hot intracluster medium of Fornax.

Overall, this galaxy represents an ideal target to probe the influence of the cluster environment on its globular cluster population. In order to more firmly study the role of the dwarf galaxies in the context of galaxy and GCS formation scenarios, and the environment impact on their GCSs, a larger sample of dwarf galaxies should be considered, which is our goal for a future study.

In Section 1.2 we describe the observational data and its reduction. Section 1.3 is devoted to the globular cluster candidate selection and contamination estimates, and in Sect. 1.4 we analyze the properties of the selected GC candidates. Finally, in Sect. 2.4 the main conclusions are presented.

1.2 Observations, reduction and photometry

1.2.1 Observational data

Deep optical images of NGC 1427A in U, B, V, I, and Hα band passes were taken with the Focal Reducer and Low Dispersion Spectrograph 1 (FORS1) on the UT2 of the ESO Very Large Telescope (VLT) at Cerro Paranal, Chile. In addition, near-infrared (NIR) images in J-band (1.5 μm) were taken with the Infrared Spectrometer And Array Camera (ISAAC) attached to the UT1 of the ESO/VLT. The complete NIR data set includes H and K_s imaging, however only the J-band was deep enough to perform this study. The FORS1 instrument has a 2048×2048 CCD detector with $0\farcs2$/pixel resolution providing a $6\farcm8 \times 6\farcm8$ field of view. The ISAAC imager is equipped with 1024×1024 array with pixel scale of $0\farcs15$/pixel covering a $2\farcm5 \times 2\farcm5$ field. Two adjacent fields were taken in the NIR in order to cover NGC 1427A. All observations of NGC 1427A were performed under photometric conditions.

Table 1.1: Log of observations.

Date	Filter	Center Position RA; DEC (J2000)	Exp.time [sec]	FWHM [pixels]	Seeing [″]
2003-09-29	U	03:40:10.0 -35:36:57.9	7×1595	3.0	0.60
2002-11-06	B	03:40:10.0 -35:36:57.9	8×450	2.4	0.48
2002-11-02	V	03:40:10.0 -35:36:57.9	10×150	2.9	0.58
2002-11-02	I	03:40:10.0 -35:36:57.9	20×165	2.7	0.54
2003-01-02	Hα	03:40:10.0 -35:36:57.9	6×1000	2.7	0.54
2002-10-05	J	03:40:15.0 -35:37:14.0	30×40	2.8	0.42
2002-11-06	J	03:40:05.0 -35:37:14.0	24×40	3.3	0.49

The observation dates, the exposure times and the average seeing are listed in Table 1.1. The seeing (FWHM) was measured on the combined final images using the IRAF[1] routine PSFMEASURE. The different seeing in the Ks band for the two fields (observed in the same night) is mainly due to the low number of stars used for its computation.

The six Hα images were obtained with the FORS1 Hα/2500+60 filter with central wavelength at $\lambda = 6604$ Å and FWHM = 64 Å.Given the radial heliocentric velocity of $V_r = 2027.8 \pm 0.8$ km/s (Bureau et al. 1996), NGC 1427A is placed at redshift

[1]IRAF is distributed by the National Optical Astronomy Observatories, which are operated by the Association of Universities for Research in Astronomy, Inc., under cooperative agreement with the National Science Foundation.

$z = 0.00676$. Hence, the Hα emission lines of NGC 1427A (rest frame wavelength at 6563 Å) are redshifted by 44 Å, which is 3 Å above the central wavelength of the Hα filter used.

1.2.2 Reduction and photometry

The basic image reduction was performed in a standard way using IRAF software packages. The bias subtraction and flat field corrections were applied using the CCDRED package taking into account the CCD noise parameters. The IR images were taken in the usual object-sky-object-sky sequences. Both object and sky exposures were bias- and flatfield-corrected in the same manner. The sky images were cleaned from all detected sources with a SExtractor object map, and object residuals were manually replaced with nearby empty sky patches. Then, these cleaned sky images were subtracted from the associated object exposures to obtain a background corrected science frame. Before combination, each single exposure in each filter was shifted by integer pixels to a defined reference image to provide the image flux conservation during the transformations. For cosmic rays rejection we used the laplacian cosmic-ray identification algorithm described and provided as IRAF cl-script[2] by van Dokkum (2001). Examination of the output rejected pixel map showed that this routine did a nice work cleaning all cosmic rays without touching the sharp tips of the point sources. Given the sharpness of the images (see FWHM in Table 1) this was a major problem when using the IRAF built-in rejection algorithms, which cut the stars' tips, during the image combining process. This is why we preferred first to clean the reduced images in each filter and then to combine them to a single image without rejection algorithms. From the final average combined images a color image of NGC 1427A was produced (Fig. 1.1[3]) using U, V and Hα filters.

Point sources in NGC 1427A were identified using the DAOFIND routine of the DAOPHOT package (Stetson 1987), adopting a detection threshold of $5\,\sigma$ above the sky level. Lower thresholds were found to give too many spurious detections. Visual image inspection showed that no objects were missed and only few false detections were included in the lists.

In order to improve the faint object photometry the underlying and extended galaxy light was subtracted form the original images. This was done with a ring aperture median filtering on images from which bright objects had been previously subtracted. A smoothing kernel of 41 pixels radius proved to give the best results, i.e., the wings of the bright, well-exposed stars were not affected. This was confirmed by the comparison between magnitudes of stars measured in the subtracted and non-subtracted images (see below). The filtered images in each pass-band were subtracted from the original ones, and the resulting images then were used for photometry. Due to the complex structure of this irregular galaxy it was impossible to fit and subtract a simple model.

An example of the V-band images passed through the filtering procedure is shown in Fig. 1.2. With this choice of ring radius only the brightest overexposed foreground stars and extended background galaxies were affected. The residual image on the

[2] http://www.astro.yale.edu/dokkum/lacosmic

[3] Figure 1.1 appeared on the cover of the Astronomy & Astrophysics journal. Parts of the research from Georgiev et al. (June II, 2006) were included in a press release of ESO (ESO 27/06; 26 July 2006). See also "The ESO Messenger" 125, p.40; Sept. 2006.

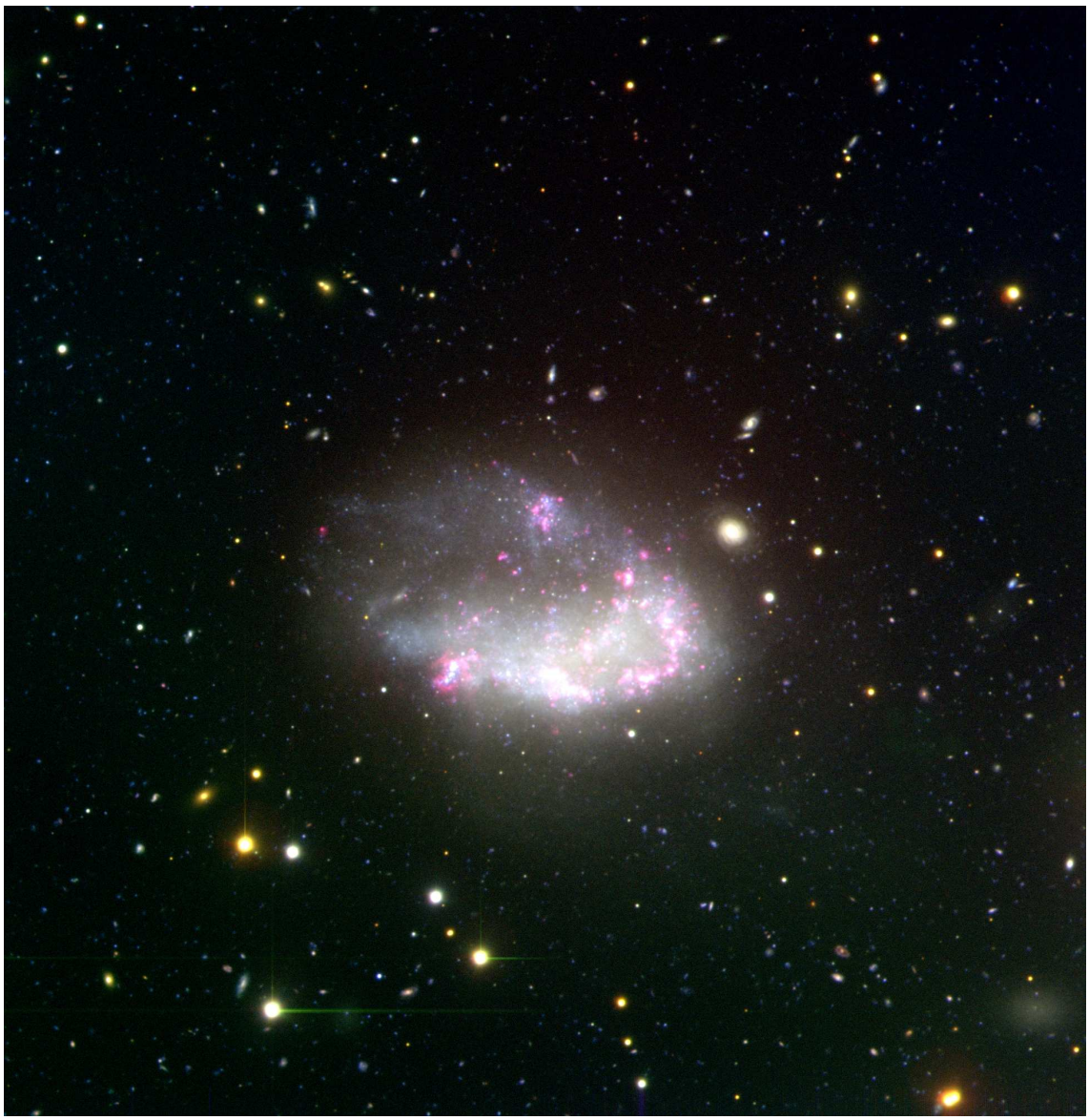

Figure 1.1: NGC 1427A color composite image. For the blue, green and red channels the U, V and Hα filters were used, respectively. North is up, East is on the left. The entire field of view of this image is $\sim 6\farcm7 \times 6\farcm7$ which corresponds to $\sim 37 \times 37$ kpc at the Fornax Cluster distance.

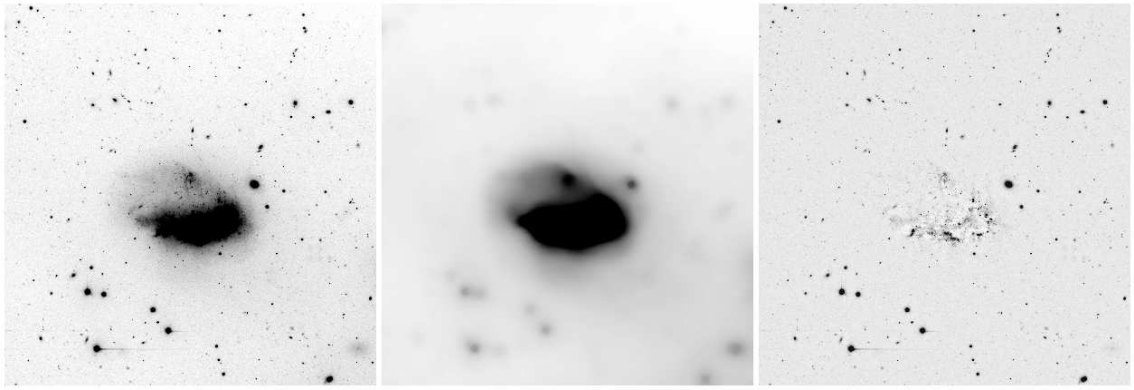

Figure 1.2: Left: V band image of NGC 1427A. Middle: median-filter smoothed image (using smoothing kernel of 41 pixels radius). Right: median-filter subtracted residual image.

right panel was used for the final photometry. In order to obtain reliable photometry for all objects, especially those in the most crowded regions, a point-spread function (PSF) photometry was performed. To create the PSF model we selected between 7 and 15 (depending on the filter) well-isolated PSF stars. The PSF photometry was performed with the DAOPHOT/ALLSTAR procedure.

To account for the star light lost due to the PSF model fitting and smoothed image subtraction, the differences between the aperture photometry and the PSF photometry magnitudes were determined using curves of growth for various aperture sizes in all filters. These curves of growth proved that the median filtering, with this choice of of kernel radius, did not affect the stellar profiles significantly. Hence, the correction to be applied is mainly due to PSF-model fitting effects. We adopted a radius of 16 pixels (corresponding to $> 5\times$FWHM) for all filters. The corrections are listed in Table 1.2.

Table 1.2: Listed are the PSF magnitude corrections ($r_{ap} = 16 \rightarrow \infty$); the accuracy of the fits to the transformation equations and the completeness limits in U, B, V, I and J bands.

Filter	U	B	V	I	J	
					Field1	Field2
Corr.	-0.099	-0.058	-0.087	-0.074	-0.074	-0.057
rms	0.058	0.042	0.023	0.026	0.050	0.045
90%	26.21	26.95	25.65	25.66	21.12	20.67
50%	26.85	27.41	26.55	26.28	21.99	21.59

Photometric calibrations of each data set from instrumental to standard magnitudes were performed in a standard way using Landolt (1992) standard stars which were observed in the corresponding nights. After fitting the zero points, extinction coefficients and color terms (as given by the ESO Quality Control for the corresponding nights), the resultant rms of the fits for the $UBVI$ and J photometry are shown in Table 1.2.

The main objects of interest for the current paper are the old globular clusters associated with NGC 1427A. At the adopted distance of the Fornax Cluster, one FORS1 pixel ($0\farcs2$) corresponds to ~ 19 pc projected size. Given the mean FWHM

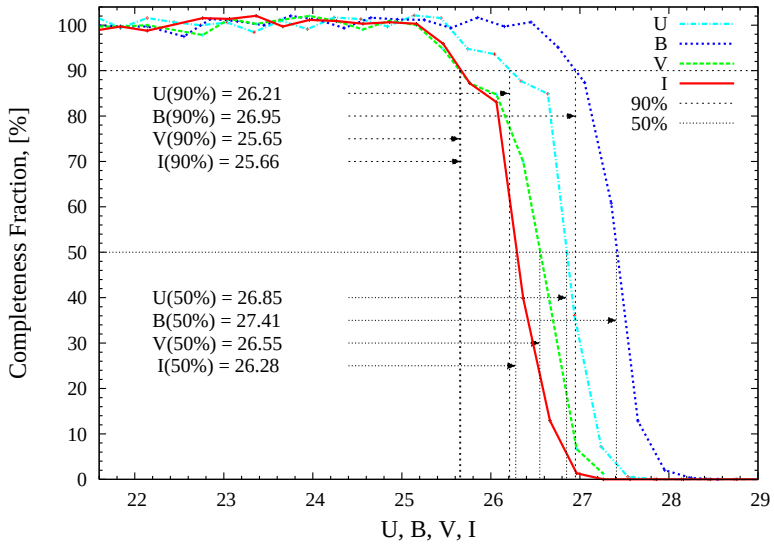

Figure 1.3: Completeness functions estimated with the add-star experiment.

(≤ 3 pixels) of our images all compact sources associated with NGC 1427A (SCs, rich OB associations, compact H II regions, or very luminous giant stars) are expected to have a star-like profile and the adopted PSF photometry is a good choice.

1.2.3 Completeness determination

At the distance of the Fornax Cluster the expected universal turnover magnitude of the globular cluster luminosity function (absolute value $M_{V,TO} \simeq -7.4$ mag; Harris 1996, 2001) is expected at $V_{TO} \sim 24$ mag. To estimate up to which limiting magnitude our observations are complete we used the final combined and background subtracted images and the IRAF/DAOPHOT/ADDSTAR procedure.

To avoid artificial crowding in the images we added 100 stars per image with magnitudes ranging from 21 to 29 mag in the optical and 14 to 25 mag in the IR images in 100 runs. Thus, the total number of stars that were added per filter is 10 000. The artificial objects were generated from the PSF of each correspondent field. Detection and photometry of the artificial objects was performed in the same manner as described in Sect. 1.2.2. The recovered number of objects divided by the number of the input artificial stars then gave us the completeness fraction. In Fig. 3.4 we show the completeness functions for the optical and IR data. The completeness is a function of the background level, hence it is expected to be variable toward the central galaxy regions. This effect should be accounted for if the photometric study is devoted mainly to the objects in those inner most regions. However, the GCs which we study here are typically located at large galactocentric distances and this effect is expected to be not so significant. The long exposure times and the photometric conditions resulted in deep images in the optical wavelengths (see Fig. 3.4 and Table. 1.2). In the UBV and I-bands we easily reach > 1 mag beyond the expected turnover of the GC luminosity function , while in the near-IR we reach only its bright end (e.g., $M_{J,TO} = -9.21$ mag; Barmby et al. 2001, thus $J_{TO} \simeq 22.2$ mag).

1.2.4 H_α calibration and results

The calibration of the Hα images was based on the spectro-photometric standard star LTT 1020 (Hamuy et al. 1992, 1994). As initial guess for the extinction coefficient we used the observatory value for the R filter and then computed our zero point. Using the magnitude and luminosity of LTT1020 we obtained the following relation

$$m_{\mathrm{H}_\alpha} = -2.5 \times \log(\mathrm{F}_{\mathrm{H}\alpha}) - 21.51 \pm 0.11 \tag{1.1}$$

where $\mathrm{F}_{\mathrm{H}\alpha}$ is the flux in erg $\mathrm{s}^{-1}\,\mathrm{cm}^{-2}\,\mathrm{\AA}^{-1}$. This relation was subsequently used to convert from magnitude to H_α luminosity in order to derive the star formation rate (SFR) for NGC 1427A (see below).

The raw Hα images were reduced, aligned, registered, and a final combined and background subtracted Hα image was produced (Sect. 1.2.2). In order to subtract the continuum emission from our Hα image we follow Knapen et al. (2004) and use as reference the I-band image (due to the lack of a R-band image). To determine the scaling factor, which tells how the continuum image must be scaled to match the intensity level of the continuum emission in the Hα image, we followed the approach described by Böker et al. (1999). The determination of the scaling factor between the images was done by fitting the intensity (counts/sec/pix) of each pixel in Hα versus the intensity of the same pixel in the continuum image. In the absence of emission and no color variations across the image the pixel relation should be a straight line (Böker et al. 1999). Pixels deviating from the straight relation trace intrinsic color variations, differential extinction, Hα emission or a mixture of all. The slope of the line gives the scaling factor and its intercept yields an additional estimate for the background level in both images. The plot of the flux distribution illustrates the galaxy's complexity. The large scatter is caused by the ionized gas contribution (e.g., Böker et al. 1999).

We applied the so determined scaling relation to the I-band image and subtracted it from the Hα image. This gave us the resulting pure Hα emission-line image. As expected, sources without Hα emission disappeared to the background level whereas sources having Hα in absorption were over-subtracted. A check for young embedded star clusters or compact H II regions contaminating the GC candidate sample revealed no emission in excess or in absence at the GC candidate's positions on the residual H_α images. Our conclusion is that the selected GC candidates are hardly if at all polluted by young compact sources from the inner starburst galaxy regions.

The brightest background/foreground objects were masked out on the so obtained residual Hα images and the Hα magnitude of the galaxy was measured using the IRAF/STSDAS task ELLIPSE. For the conversion from magnitude to luminosity we used the adopted distance of 19 Mpc (Freedman et al. 2001). The star formation rate was derived from the Hα flux using the improved relation given by Hunter & Elmegreen (2004):

$$\dot{M} = 5.96 \times 10^{-42} L_{H_\alpha} 10^{0.4 A_{H_\alpha}}\ \mathrm{M}_\odot/\mathrm{yr} \tag{1.2}$$

where L_{H_α} is the H_α flux in erg/s, $A_{H_\alpha} = 0.811 A_V$ is the extinction coefficient in H_α. We derived $\dot{M} = 0.057\ \mathrm{M}_\odot/\mathrm{yr}$. This is a typical value for a starburst dIrr galaxy (Hunter & Elmegreen 2004; Seth et al. 2004). This estimate should be regarded as

an upper limit for the SFR since, due to the lack of flux calibrated emission-line spectra for N 1427A, no care was taken for the N II 6548,6583 emission-line doublet, which partly falls within the H_α filter pass-band.

1.2.5 Foreground and intrinsic extinction

Absorption caused by the Galactic interstellar medium (ISM) that affects the objects' magnitudes, hence colors, have to be taken into account in order to compare the object's colors (magnitudes) with those of stellar evolutionary models (Sect. 1.3.1).

In order to calculate the extinction correction towards NGC 1427A for each filter we adopted[4] $E(B-V) = 0.012$ (Schlegel et al. 1998), $A_V = 3.1 \times E(B-V)$, formulae (2) and (3) in Cardelli et al. (1989) and the central wavelengths for the FORS1 and ISAAC filters taken from the ESO web page.

Although the purpose of the J, H, K imaging was to determine the extinction map of NGC 1427A, the images turned out to be too shallow for this goal. Therefore, we can not apply individual internal reddening correction, which could be large for clusters located inside or behind the galaxy body. Nevertheless, we do not expect this to be a significant effect because of the following reasons. First, as will be seen in Fig. 1.9, we observe $\sim 10 - 15$ candidates in the innermost galaxy regions, and only a fraction of these are expected to be inside or behind, and therefore affected by internal extinction. Second, James et al. (2005), studying the extinction on the H_α flux as a function of the galaxy type, show that the mean extinction correction for dIrrs is $A_{H_\alpha} \simeq 0.4$ mag, which transforms to $E_{B-V} \simeq 0.06$ (or $V - I \simeq 0.07$ mag). The overall internal reddening therefore is expected to be small and this is why we consider in the following only the foreground extinction.

1.3 Globular cluster candidates selection

Our final photometry list contains stars, star clusters and extended objects (galaxies, H II regions, OB-associations, etc.). In order to select globular cluster candidates we apply color, magnitude and size selection criteria according to the expected properties of these old stellar systems at the distance of NGC 1427A.

1.3.1 Color and magnitude selection

The globular cluster candidate selection is mainly based on the colors of the objects in the color-color diagrams. The adopted distance modulus to the Fornax cluster limits the expected brightest globular cluster magnitude to be $m_V \simeq 21$ mag assuming $M_V = -10.29$ for the brightest Milky Way (MW) globular cluster ω Centauri (Harris 1996).

To constrain a region of typical GC colors we use the 2003 updated version of the Harris (1996) catalog of MW GCs [5]. The color selection limits, which we chose as first selection criterion, are defined as an ellipse that approximately encompasses the colors within $-0.16 \leq (U - B) \leq 0.7$ and $0.72 \leq (V - I) \leq 1.4$ (see Fig. 1.5). These color ranges are found to be typical for GCs in a large variety of galaxy types

[4] http://nedwww.ipac.caltech.edu/

[5] http://www.physics.mcmaster.ca/Globular.html

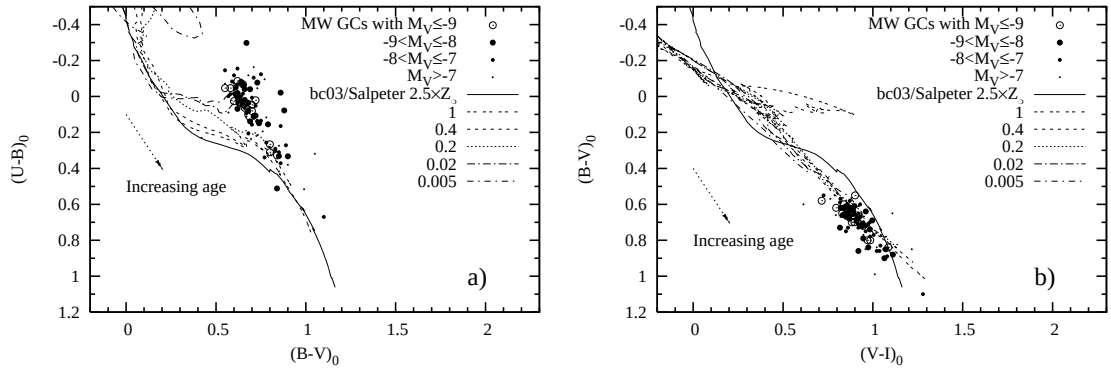

Figure 1.4: Milky Way globular clusters' $(U-B)_0$ vs. $(B-V)_0$ (**a**) and $(B-V)_0$ vs. $(V-I)_0$ (**b**) color-color the power of a color-color selection". (readers can see that anyway) diagrams. The clear metallicity separation of the MW globular cluster system can easily be seen in (**a**), while in (**b**) the objects' metallicity separation smears out and the SSP models for different metallicities are indistinguishable.

(eg. Ashman & Zepf 1998; Larsen et al. 2001; Lotz et al. 2004; Chandar et al. 2004; Sharina et al. 2005, and ref's therein).

The $(U-B)$ vs. $(V-I)$ and the $(U-B)$ vs. $(B-V)$ color combinations proved to be the most distinctive when disentangling ages and metallicities. Any color combination *not* including the U-band makes the models almost indistinguishable (compare the two panels in Fig. 1.4), hence leading to large uncertainties in assessing ages and/or metallicities. Due to line blanketing effects in the stellar atmospheres the $(U-B)$ color is very sensitive to metallicity variations. Therefore, inclusion of the U-band in photometric studies aiming at accurate age/metallicity determinations is very important. A detailed discussion on the right filter selection when comparing observations with evolutionary synthesis models is provided by Anders et al. (2004). Indeed, as shown in Fig.1.4, the well established bimodal metallicity distribution of the MW globular cluster system (e.g., van den Bergh 1993; Carney & Harris 1998; Mackey & van den Bergh 2005, and references therein) can easily be seen when using $(U-B)$ color.

In Fig. 1.5 we show the colors of all point sources detected in the FORS1 field, corrected only for foreground Galactic extinction. The different symbol types indicate different V-band magnitudes of the objects. The arrow shows the direction and the magnitude with which the color of an object would have to be shifted if an extinction of $A_V = 1$ mag intrinsic to NGC 1427A is applied.

Representative photometric errors are shown in Fig. 1.5 to demonstrate the accuracy of our photometry for objects in the magnitude bins around the expected GC luminosity function turnover at ~ 24 mag and obeying the GC candidate selection criteria (see Sect. 1.3.2).

In the color-color diagram one can see a large number of blue objects. Examination of the positions of these objects showed that most of them are found in the inner starburst regions of NGC 1427A. The rest of the blue objects are associated with faint sources, likely background galaxies and sources associated with them: An example is the background spiral galaxy westward of NGC 1427A (Fig. 1.1). The visual inspection of the observed very red and bright objects with $(V-I) > 1.5$

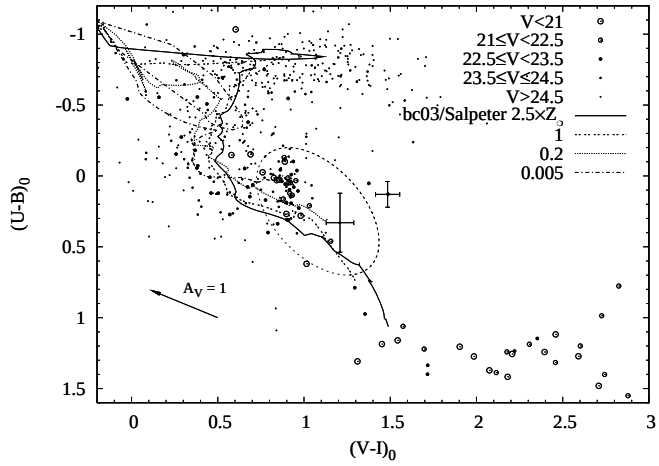

Figure 1.5: $(U-B)_0$ vs. $(V-I)_0$ diagram showing the colors of all point sources (Sect. 1.3.2) found in the FORS1 field. The different point types indicate objects with different magnitudes. The arrow shows the magnitude and the direction that would have to be applied to the colors of objects subject to an intrinsic extinction of $A_V = 1$ mag. With lines are plotted the Bruzual & Charlot (2003) SSP models for different metallicities. Representative photometric errors are shown for two GCs with luminosities around the expected GCLF turnover magnitude.

showed that they are saturated foreground stars and likely background elliptical galaxies. In the color region where GCs are expected a high density of objects is observed.

1.3.2 Point source selection criterion

As pointed out in Sect. 1.2.2 the distance to NGC 1427A puts an additional constraint to the expected sizes of the GCs associated with NGC 1427A. The typical GC half-light radii are in the range 1 to 20 pc (eg. Kundu & Whitmore 2001; van den Bergh & Mackey 2004; Jordán et al. 2005). Given the adopted distance to the Fornax cluster, 1 pixel of our images corresponds to ~ 19 pc projected size. Therefore, GCs are expected to be unresolved and to have point source radial profiles. As point source selection criterion we used the IRAF ALLSTAR task output parameter "sharp". Sharp is computed during the fit of the PSF model and estimates the intrinsic angular size of the object. It is roughly defined as the difference between the square of the width of the object and the square of the width of the PSF. It has values close to zero for unresolved point sources, large positive values for blended sources and partially resolved galaxies and large negative values for cosmic rays and blemishes.

As first selection criterion we used the color-color limits explained in Sect. 1.3.1. Then for the color-color selected objects we plotted the V-band sharp value against V_0, $(U-B)_0$ and $(V-I)_0$. Plots of the sharp values for the other filters were produced and showed insignificant differences. However, such differences might be expected between U-band and V-band sharp values for example if in the selected color-color region highly reddened bright compact H II regions embedded in the NGC 1427A starburst regions are observed. Such objects can have different profiles in the U and in the V filter due to the enhanced contribution of the ionized gas in

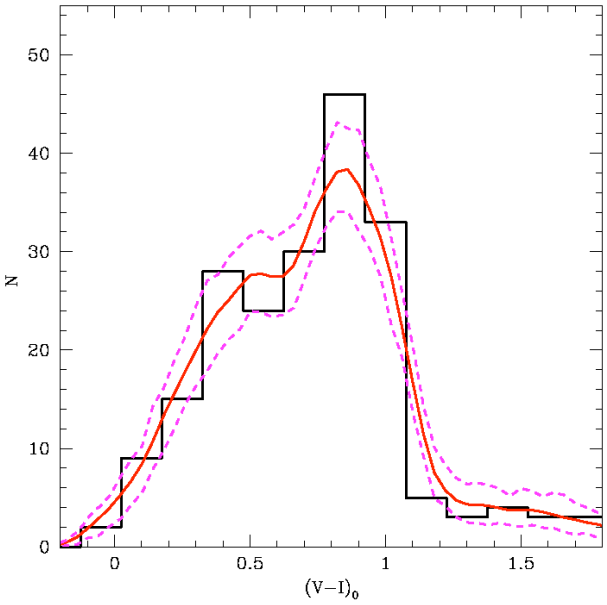

Figure 1.6: $(V-I)_0$ color distribution of all point sources with $(U-B)_0 \geq -0.3$ (see Fig. 1.5). The $U-B$ color cutoff was introduced to lower the contamination from faint or objects with highly uncertain photometry in the starburst regions. The Epanechnikov-kernel probability density estimate and its 90% confidence limits are plotted with thick/red and dashed/magenta lines, respectively. Similar color distributions are observed in star cluster systems of field dIrrs Sharina et al. (2005).

U-band which is invisible in V.

The shape of the functions defining the upper and lower cutoff sharp values were determined from the sharp value distribution of artificially added stars previously used for the completeness tests (Sect. 1.2.3). The scatter of the sharp value increases towards fainter magnitudes due to increasing uncertainties in the PSF fitting procedure. At approximately $V_0 = 24.3$ and $(V-I)_0 = 0.86$ mag couple of objects slightly above the sharp cut-off function are observed. A visual inspection of these objects revealed that they are somewhat extended sources embedded in the central starburst regions, which suggests at their young nature. An additional check was made using available HST/ACS images which ultimately revealed their morphology as diffuse and blended sources. The final list of our GC *candidates* contains 60 objects.

The $(V-I)$ color distribution for all point sources (presumably star clusters) with $(U-B) \geq -0.3$ is shown in Fig. 1.6. The $U-B$ cutoff was introduced to lower the contamination from very faint unresolved amorphous objects with $V-I$ colors within the old GCCs range (compare with Fig. 1.5). An Epanechnikov-kernel probability density estimate shows a clear indication for (at least) two characteristic $(V-I)$ color peaks at ~ 0.4 and 0.9 mag. These color peaks are similar to those found in the colors distributions of star cluster systems in field dIrr galaxies (Sharina et al. 2005). However, the contamination effects in our sample prevent us from a more detailed analysis.

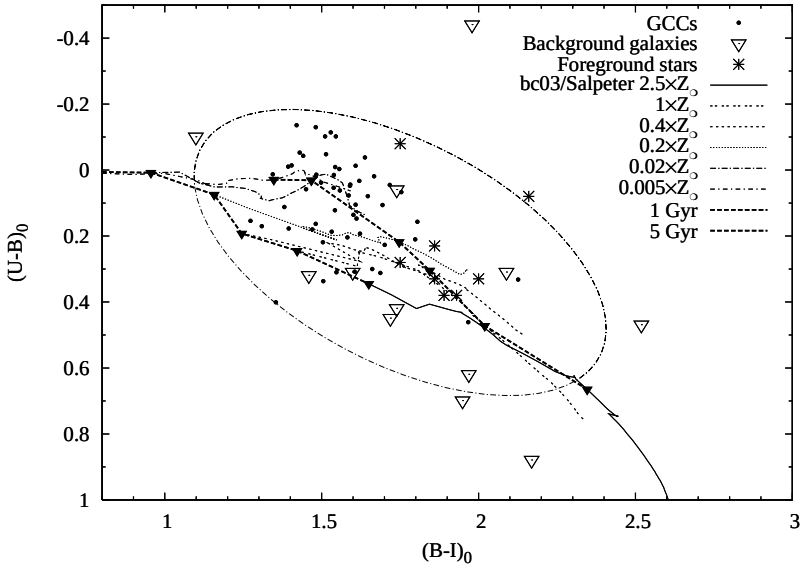

Figure 1.7: $(U-B)_0$ vs. $(B-I)_0$ color-color diagram of the selected globular cluster candidates (dots), foreground stars (asterisk) and background galaxies from the FDF catalog (open triangles). The ellipse indicates the transformed GC candidate color-color selection region as indicated in Fig. 1.5. Lines show iso-metallicity tracks and isochrones for various ages and metallicities.

1.3.3 Contamination and GC numbers

Despite the applied globular cluster selection criteria, there can still be sources contaminating our final GC candidate sample in the selected color limits. Possibilities are faint ($V \geq 21$ mag) Galactic halo stars, distant and compact bulges of unresolved background galaxies, and unresolved low-redshift ($z \sim 0.1 - 1.0$) starburst galaxies with ages ≤ 300 Myr (Puzia et al. 2004). Highly reddened ($A_V \geq 1$ mag) young compact sources (H II regions, OB associations, young star clusters) in the inner regions of NGC 1427A are potential contaminants as well. This is estimated in Sect. 1.3.3 below.

Another source of contamination to the list of GC candidates of NGC 1427A is contamination from possible Fornax intracluster globulars (Bassino et al. 2003) and the GC population of NGC 1399 which is thought to extend to large distances (Dirsch et al. 2003). We discuss this in Sect. 1.3.3.

Foreground/background

To estimate the foreground star contamination we used a synthetic Galaxy stellar population model[6] (Robin et al. 2003). For the specified color and magnitude ranges (Sect. 1.3.1 and 1.3.2) and within the FORS1 field of view the model predicts a total number of 7 foreground stars towards NGC 1427A (see Fig. 1.7).

We estimate the contamination by background galaxies using the FORS Deep Field (FDF) data (Heidt et al. 2003). The main criterion for selecting objects from the FDF cataloged as galaxies is the limiting bright magnitude cutoff $I \geq 20.1$ mag and the completeness limit of our observations in the I-band (Fig. 3.4). However,

[6] http://bison.obs-besancon.fr/modele/

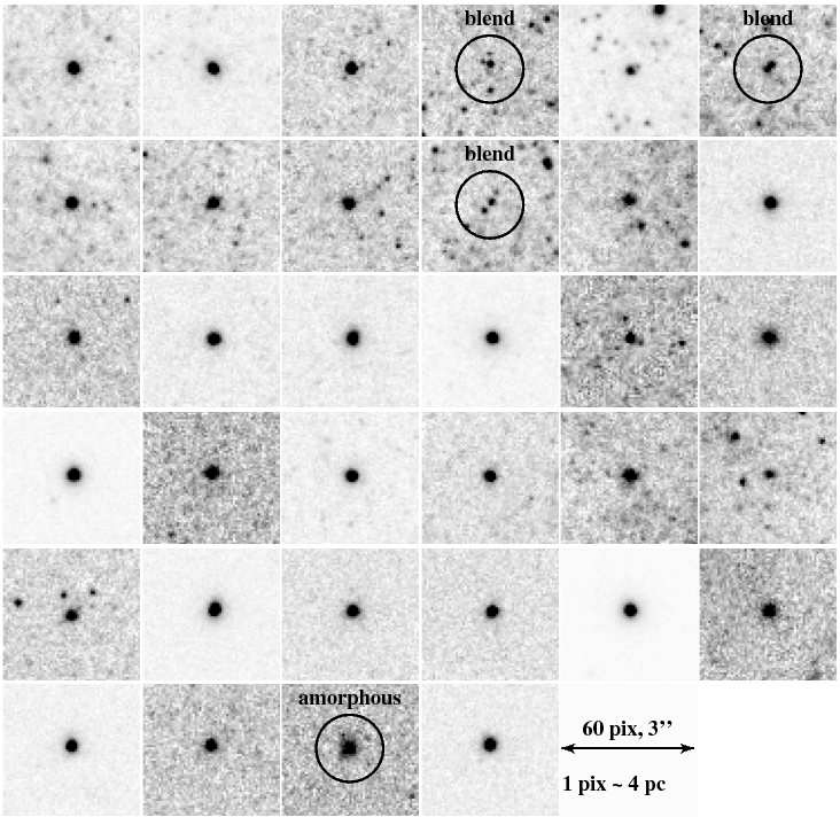

Figure 1.8: F625W-band mosaic of the GC candidates as seen using HST/ACS. Circles indicate the three blends and the amorphous objects which were rejected from the original ground-based GC candidate list based on these ACS data.

the inspection of our final globular cluster candidate sample shows that there are no candidates with $I \geq 24.5$ mag, which actually represents the faint end of the GC luminosity function. Therefore, in Fig. 1.7, due to the lack of V-band photometry in the FDF, we present the $(U-B)_0$ vs. $(B-I)_0$ color distribution of the background galaxies in the range $20.1 \leq I \leq 24.5$ mag (triangles). It can be seen that ~ 7 background galaxies are expected in the GC candidate color-color region.

As an attempt to identify these background galaxies, as well as contamination from blended sources in the crowded galaxy regions, we take advantage of the high spatial resolution of archival HST/ACS images of NGC 1427A taken with the F625W filter (Program GO-9689, PI: M. Gregg), which were combined using MultiDrizzle (Koekemoer et al. 2002). A visual examination shows that none of the 34 GC candidates (out of 60) in common for the FORS1 and ACS fields are resolved as obvious background galaxies. The appearance of the GC candidates on the ACS chips are presented in Fig. 1.8. This shows that our point-source selection criteria performed well and only a fraction of the seven BG galaxies estimated above could remain unresolved by ACS. However, three of our GCCs turned out to be blended sources and one seems amorphous (possibly a compact OB-association, see Fig. 1.8). The latter is located in the inner starburst regions of the galaxy and passed the point-source selection criteria at the faint magnitude end. The blends and the amorphous object were excluded from subsequent analysis.

Due to the smaller field of view of HST/ACS relative to the FORS1 field, not all candidates could be examined this way, especially those far from the galaxy body. Thus we can not extrapolate the above conclusions to the rest of the candidates, and unresolved background objects could still be present among the remaining 26 GCCs. Discrimination between GCs and foreground stars is also not an easy task since one ACS pixel corresponds to ∼4 pc projected size at the Fornax distance. Thus, GCs more compact than this would have a stellar appearance. Only spectroscopy can fully address the true foreground/background contamination fraction. A detailed analysis of the NGC 1427A HST/ACS data will be presented in a forthcoming study.

Fornax cluster GC contamination

Figure 1.9 shows the spatial distribution of GC candidates around NGC 1427A across the V-band FORS1 field of view. It can be seen that the number of GC candidates increases towards the galaxy's center, which suggests that they are really associated with NGC 1427A. The surface density of all GCCs is shown in Fig. 1.10 with red/solid histogram together with the Poisson errors.

However, the relatively close projected distances (see Fig. 1.9) between NGC 1427A and the giant elliptical galaxy NGC 1399 (22.′9) and the other nearby elliptical NGC 1404 (15.′7) raise the question whether all found GC candidates really belong to NGC 1427A. A study of the NGC 1399 GCS by Dirsch et al. (2003) concludes that even in their (most distant) studied field (which extends up to $\leq$ 23 arcmin from NGC 1399) the number counts have not yet reached the background value. However, as they point out, at such large distances their fields could contain possible intracluster GCs (ICGC) as proposed by Bassino et al. (2003) in their search for GCs around dwarf elliptical galaxies in the Fornax cluster. The latter study derived an intracluster GC surface density of $\sim$ 0.25 and 0.13 GCs/arcmin^{-2} at distances of 40′and 110′from the cluster center, respectively. The existence of intracluster globulars is further supported by recent simulations by Yahagi & Bekki (2005).

The estimated GC number density contamination from the NGC 1399 GCS is shown as a green/dashed histogram in Fig. 1.10. At the distance of NGC 1427A, 22.′9, $\sim$ 1.26 globular clusters per arcmin^2 are predicted (Dirsch et al. 2003). Fig. 1.10 shows that at large galactocentric distance from NGC 1427A, our number counts are considerably below the expected contamination from NGC 1399, though still within the errorbars.

There are three possibilities that could account for this discrepancy between the observed and expected contamination level from NGC 1399. The first one is that we are missing a number of GCs. However, according to the completeness analysis (Sect. 1.2.3) we are confident that this is not the case. The second possibility is that the Dirsch et al. (2003) values might not be applicable toward NGC 1427A, which is likely, because the fields studied by Dirsch et al. (2003) extend towards the nearby elliptical galaxy NGC 1387 (their Fig. 1) which could give rise to an enhanced GC number density. The third possibility is to suggest a non-spherical distribution of GCs around NGC 1399 or ICGCs, resulting in a lower number density towards NGC 1427A as compared to other directions. We think that a combination of the last two is the more plausible explanation. A possible GC contamination from the even closer (15.′7) elliptical NGC 1404 seems to be ruled out as well, since its GCS is not as extended as that of NGC 1399. Indeed, at a distance from NGC 1404 of only 3 arcmin

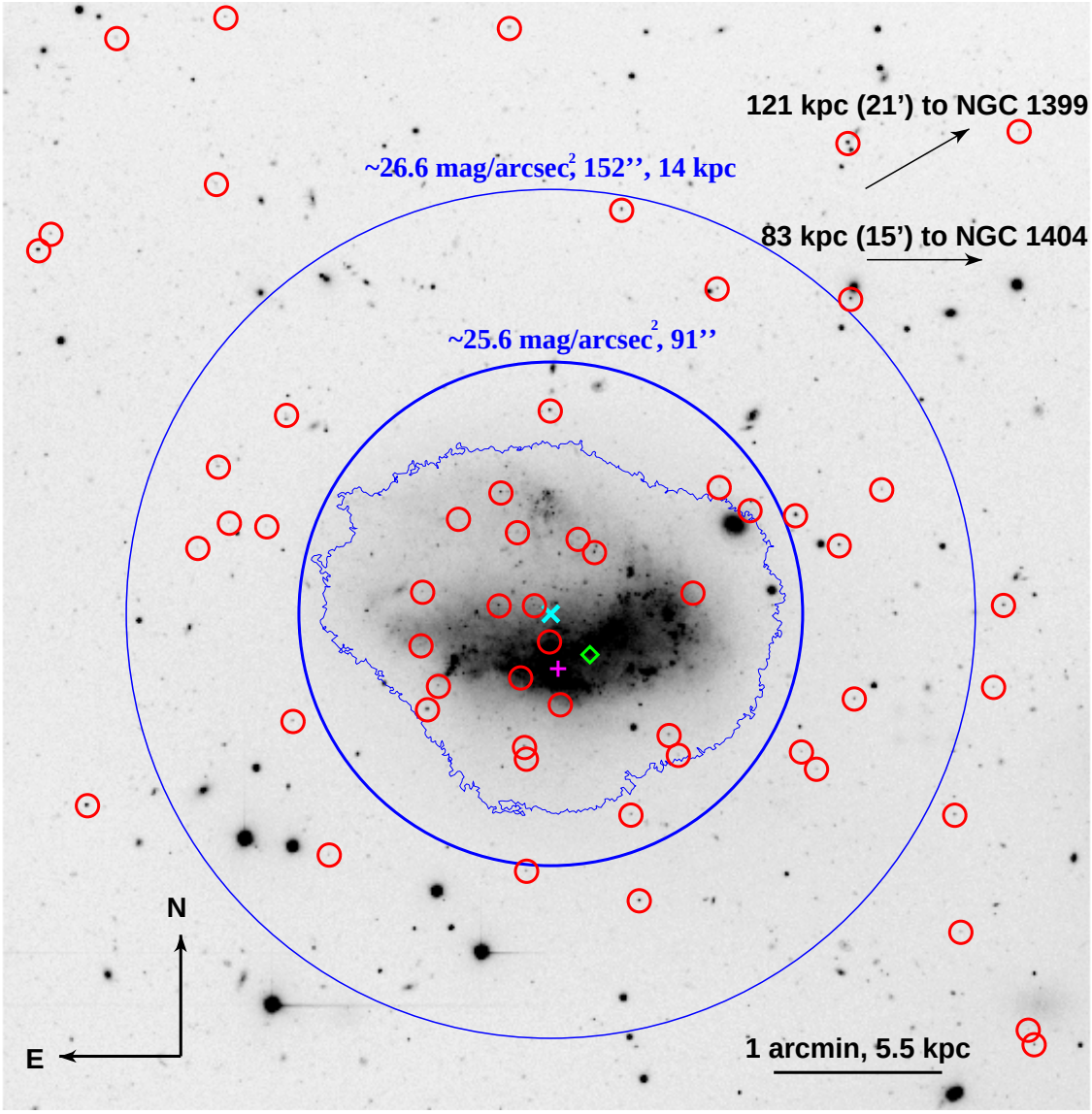

Figure 1.9: 6′.8 × 6′.8 V-band VLT/FORS1 image. The positions of the selected (see Sect. 1.3.2 and 1.3.3) GC candidates are indicated with (red) circles. With arrows the directions and projected distances towards the Fornax cD galaxy NGC 1399 and the elliptical NGC 1404 are shown. With a "×" the adopted center of NGC 1427A is marked, with a "+" the fitted center derived from the median smoothed image and with a diamond the kinematical center determined from the ionized gas kinematics (Chanamé et al. 2000). The two large circles approximately encompass the μ_V isophotes at $\mu_V = 25.6\,\mathrm{mag/arcsec^2}$ (the true contours of that isophote is shown as well) and at $\mu_V = 26.6\,\mathrm{mag/arcsec^2}$ (see Sect. 1.4.3 and Fig. 1.14).

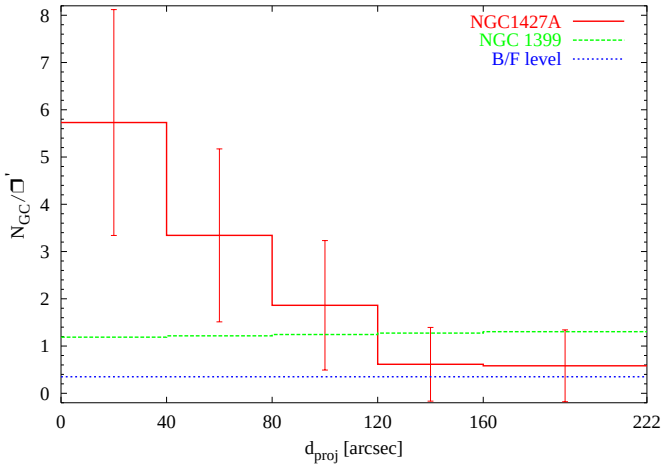

Figure 1.10: Plot of the radial number density distribution of the NGC 1427A GC candidates (thick line histogram) and the correspondent Poisson errors, the expected level of contamination by the NGC 1399 GCS at the distance of NGC 1427A (dashed/green line) and the background/foreground contamination level (dotted/blue line).

the number density is already 0.63 arcmin^{-2} (Richtler et al. 1992; Forbes et al. 1998) which, when extrapolated to the position of NGC 1427A, becomes irrelevant.

The estimated total number density of background/foreground objects (Sect. 1.3.3) shown in Fig. 1.10 (0.35 ± 0.59 objects/arcmin^2) is below the levels we reach in our outermost radial bins (0.61 ± 0.78 GCCs/arcmin^2). Although this values are within the errorbars the difference could be interpreted as: (*i*) either the local BG/FG is enhanced, or (*ii*) that there exist genuine GCs associated with either NGC 1427A, NGC 1399 or the ICGSs population at those galactocentric distances. Although the latter possibility seems more plausible to us, this is irrelevant for our purposes because the maximum contamination that we could possibly assume would be what we measure at the outermost bins (ideally containing no GCs from NGC 1427A). Thus we adopt 0.61 ± 0.78 counts/arcmin^2 as our best-estimate for the contamination level.

Final GCC number

Recalling the total of 60 candidates (Sect. 1.3.2) here we determine what fraction of these are contaminating objects. As was shown in Sect. 1.3.3 we expect 7 foreground stars, which are indistinguishable from actual GCs with our data. The expected number of background galaxy contamination (Sect. 1.3.3) is a fraction of the 7 objects predicted by FDF. Therefore we end up with a number between 10 and 14 BG/FG contaminants.

In Sect. 1.3.3 we estimated a maximum density of 0.61 objects/arcmin^2 contamination, which when multiplied by the 43 arcmin^2 FORS1 field of view, results in 26 contaminating objects. Therefore we expect a total number of contaminants between 10 and 26. Taking the mean value of 18 and the four objects rejected by ACS (Sect. 1.3.3) the final number of GCCs is $N_{\rm GC} = 60 - 4 - 18 = 38 \pm 8$, where the error encompasses the minimum and maximum number of contaminants quoted above.

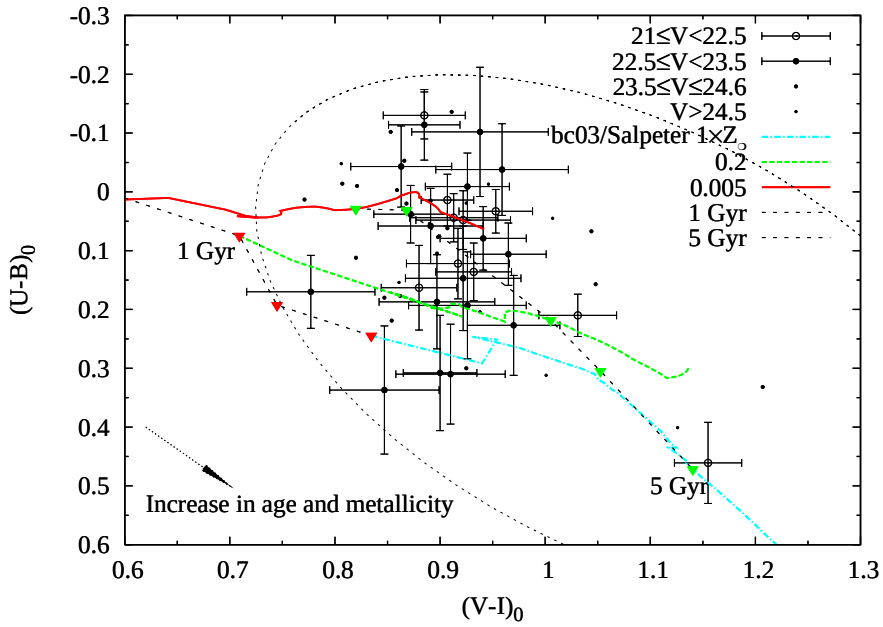

Figure 1.11: The final selected globular cluster candidate sample. Dashed lines connect the SSP models with different metallicities (in solar units) for ages 1 Gyr and 5 Gyr. With an ellipse is shown the GC color selection locus.

1.4 Analysis of the GC candidates' properties

1.4.1 Colors

In a previous study of NGC 1427A with the 2.5m DuPont telescope at Las Campanas Observatory by Hilker et al. (1997) a selection of globular cluster candidates on the basis of their $V-I$ colors only was made. The introduction of the $U-B$ color in our study significantly improved the discrimination between globular clusters and highly reddened young star clusters. Only 7 globulars are in common between the current and the previous study. The larger number of GC candidates we derive is due to the significantly larger field of view of the FORS1 CCD detector and the much deeper exposures.

The final colors of the GC candidates are shown in Fig. 1.11. They cluster around low metallicities ($Z = 0.0001$ and 0.0004) and old or intermediate ages (~ 5 Gyr) according to the Bruzual & Charlot (2003) SSP models. With dashed lines the 1 and 5 Gyr isochrones connecting SSP models with different metallicities are indicated. The photometric errors at these magnitudes and the convergence of the theoretical models prohibit accurate age and metallicity derivations for the individual globular cluster candidates. However, we can conclude that the ages and metallicities of the GC candidates around NGC 1427A as whole are comparable to the ages and metallicities of the old metal-poor Milky Way GCs.

The mean color $(V-I)_0 = 0.92 \pm 0.08$ of all GC candidates is similar to what was found for the globular cluster systems in dIrr, dSph and dE galaxies (Sharina et al. 2005; Seth et al. 2004; Lotz et al. 2004). This color corresponds to the blue GC population found in giant early-type galaxies and also obeys the relation between

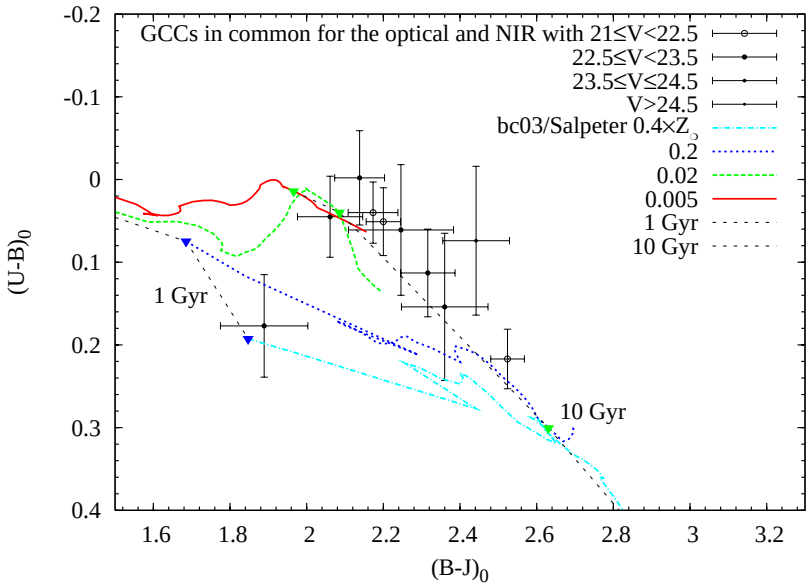

Figure 1.12: Near IR color-color diagram for GC candidates in common for the FORS1 and ISAAC fields. Overplotted are the Bruzual & Charlot (2003) SSP models for ages ≥ 1 Gyr and metallicities lower than $0.4 \times Z_{\odot}$. With dotted lines the 1 and 10 Gyr isochrones are indicated.

the host galaxy luminosity and the mean GC color (NGC 1427A: $M_V = -18.13$, see Sect. 2.3.4) (Harris et al. 2005; Peng et al. 2005; Larsen et al. 2001; Lotz et al. 2004).

In Figure 1.12 we show the properties of the GC candidates in the $(U-B)_0$ vs.$(B-J)_0$ color-color plane. This color-color selection provides the best age/metallicity discrimination governed by the filters' transmission curves. The different line types in Figure 1.12 represent Bruzual & Charlot (2003) SSP models formetallicities lower than $0.4 \times Z_{\odot}$ ($Z = 0.008$). Although the IR images were not deep enough, a simple comparison with the 1 and 10 Gyr isochrones (dotted lines in Fig. 1.12) reveals the predominantly old ages (≥ 10 Gyr) and low metallicities ($\leq 0.2 \times Z_{\odot}$) of the GC candidates. Hilker et al. (1997) showed that in integral properties NGC 1427A is similar to the Large Magellanic Cloud (LMC). Hence, taking into account the LMC metallicity of $Z = 0.04 \times Z_{\odot}$ we can set the expected upper metallicity limit to this value. This is consistent with what is observed in Fig. 1.12.

1.4.2 Luminosity function

of the original and contamination corrected GCCs sample in bins of 0.4 mag. The dashed (green) histogram shows the GCLF for the original GC candidate sample while the solid (red) histogram represents the number counts corrected for contamination using the luminosity distribution of the contaminating objects in the outermost bins as estimated in Sect. 1.3.3.

Globular cluster luminosity functions have been studied for many galaxies (eg. Ashman & Zepf 1998; Kissler-Patig 2000; Richtler 2003; McLaughlin 2003, and ref's therein). It seems that the shape of the GCLF is universal among "old" GC systems and can be represented by a Gaussian or a t_5 function. In Fig. 1.13 the Gaussian fit to the corrected GCLF is shown. Due to the low number statistics we kept the width of the Gaussian fixed to $\sigma = 1.2$ which is a typical value that

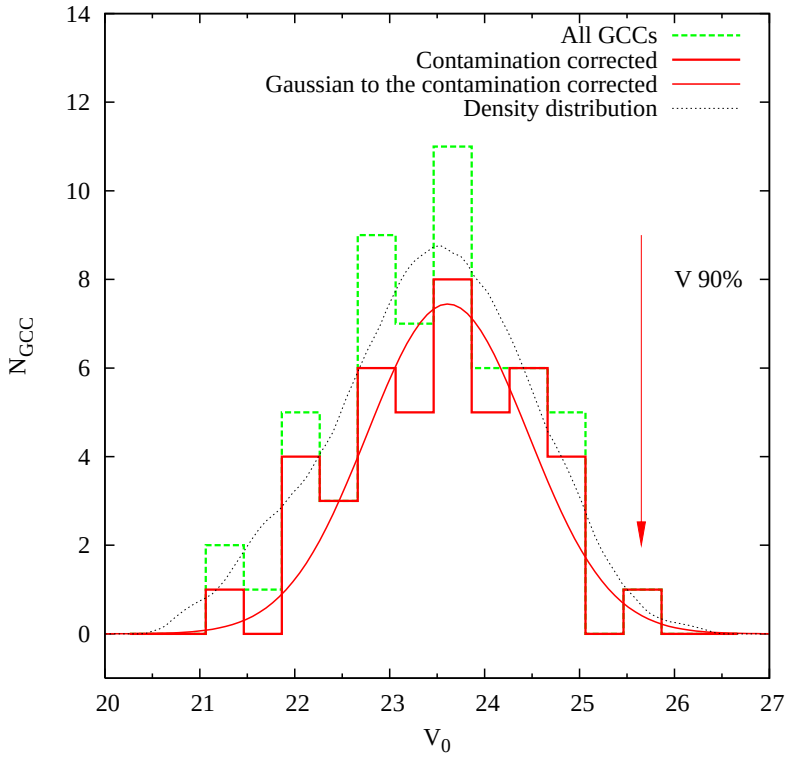

Figure 1.13: NGC 1427A globular cluster luminosity function (GCLF). The solid (red) histogram represents the contamination corrected GCLF, the dashed histogram the uncorrected one. The curves are a Gaussian fit to the corrected GCLF (solid line) and the probability density estimate of the uncorrected GCLF using an Epanechnikov kernel (dotted curve). The arrow indicates the 90% completeness limit in V-band.

fits most of the studied galaxies' GCLFs (eg. Barmby et al. 2001). This choice of the dispersion gave $V_{TO} = 23.61 \pm 0.10$ for the turnover magnitude of the BG/FG corrected sample. If we do not fix σ we obtain $\sigma = 1.45 \pm 0.16$ and $V_{TO} = 23.59 \pm 0.11$. The probability density function of the non-parametric density estimate using an Epanechnikov kernel (dotted line in Fig. 1.13) of the uncorrected GCLF has its maximum value at $V_{TO} = 23.53 \pm 0.07$ mag. The quoted uncertainties above include only the photometric errors and the uncertainty in the fit. The effect of the uncertainty in the number counts is reflected in the small difference in the final turnover magnitudes of the two distributions, which is within the errorbars. Figure 1.13 shows the NGC 1427A globular cluster luminosity function (GCLF)

Due to its universality the GCLF was frequently used as a distance indicator (for details see Richtler 2003), originally proposed by Hanes (1977). Assuming a universal turnover magnitude of $M_V = -7.40 \pm 0.11$, as derived for the MW GCS (Harris 2001) and those of other galaxies (eg. Larsen et al. 2001; Ashman & Zepf 1998, and ref's therein), the distance modulus to NGC 1427A is $(m-M) = 31.01 \pm 0.21$ mag (15.9 ± 1.6 Mpc). Our most shallow observation is in U-band with the 90 % completeness limit at $U = 26.21$, which is however still ~ 1.4 mag deeper than the expected $U_{TO} \sim 24.8$ mag (assuming a mean $U-B \sim 0.1$, $(B-V) \simeq 0.7$, $M_{V_{TO}} = -7.40$, and a distance modulus of 31.39 mag). The last bin of the histogram ($V \simeq 25.8$ mag) corresponds to $U \simeq 26.6$ mag which is approximately at the 85% completeness level. This implies a correction which makes the V_{TO} fainter by 0.01 mag, which is well

within the error and therefore we do not consider it further.

A recent study by Di Criscienzo et al. (2006) presents a new calibration of the GCLF performed on the basis of RR Lyrae in the MW, M31 and close-by galaxies as "primary" standard candles. They derive a GCLF turnover magnitudes of $V_{TO} = -7.66 \pm 0.11$ for the MW, $V_{TO} = -7.65 \pm 0.19$ for M31 and $V_{TO} = -7.67 \pm 0.23$ for the other nearby galaxies. The weighted mean for the combined turnover magnitude then is $M_{V_{TO}} = -7.66 \pm 0.09$ mag. If we apply this value to the GCS of NGC 1427A we obtain a distance modulus of $(m - M) = 31.25 \pm 0.20$ mag (17.8 ± 1.7 Mpc).

Finally, independently of which absolute GCLF turnover magnitude is adopted, the direct comparison of the apparent GCLF turnovers for NGC 1399 ($V_{TO} = 24.01 \pm 0.1$, Dirsch et al. 2003) and NGC 1427A places the latter approximately at 3.2 ± 2.5 (statistic) $\pm$ 1.6 (systematic) Mpc in front of NGC 1399. The statistical error is determined from the photometric and our fitting routine uncertainties of the turnover magnitude; the systematic error includes the uncertainties of the absolute magnitude and the GCLF method itself (Richtler 2003). It should be noted that the giant elliptical NGC 1404 is located even closer in projection to NGC 1427A. Unfortunately, the GCLF turnover magnitude for NGC 1404 (Blakeslee & Tonry 1996; Richtler et al. 1992) is not as accurately determined as that of NGC 1399, and thus we can not perform a similar comparison.

1.4.3 Specific frequency

The 'specific frequency' (S_N) is a quantity introduced by Harris & van den Bergh (1981) to intercompare the GCSs between different elliptical galaxies. The S_N is defined as the total GC ($N_{\rm GC}$) population normalized to a galaxy luminosity of $M_V = -15$ mag:

$$S_N = N_{\rm GC} 10^{0.4(M_V+15)} \tag{1.3}$$

In order to derive the specific frequency properly one needs to correct for background and foreground contamination, the unobserved part of the GCS (and the parent galaxy) and the completeness of the observations at the faint end of the GCLF. One of the most important issues is that S_N should be derived from GC counts and total galaxy light both estimated within the same area. Otherwise systematics in the GCS and/or galaxy profile could affect the estimated S_N values (Dirsch et al. 2003; Ostrov et al. 1998).

Having the V-band 90 % completeness limit ~ 1.5 mag (see Sect. 1.4.2 and Fig. 3.4) beyond the expected GCLF turnover magnitude, completeness corrections are insignificant for the estimate of S_N. Due to the complete coverage of the galaxy including its outer parts we do not need to make any geometrical corrections. In order to measure the total galaxy light of NGC 1427A we used the IRAF/STSDAS task ELLIPSE on the background subtracted images. The bright, obvious background and foreground sources were masked out. Due to the complex morphology of this irregular galaxy the definition of its center was a complicated task. We adopted the center which best represents the diffuse galaxy light distribution at the radius of the $\mu_B = 26$ mag arcsec^{-2} isophote (marked with "×" in Fig. 1.9). This is the common center for the both circles drawn in Fig. 1.9 in which we estimate the S_N. The V-band isophote ($\mu_V = 25.6$ mag arcsec^{-2}) shown in Fig. 1.9 is determined at the

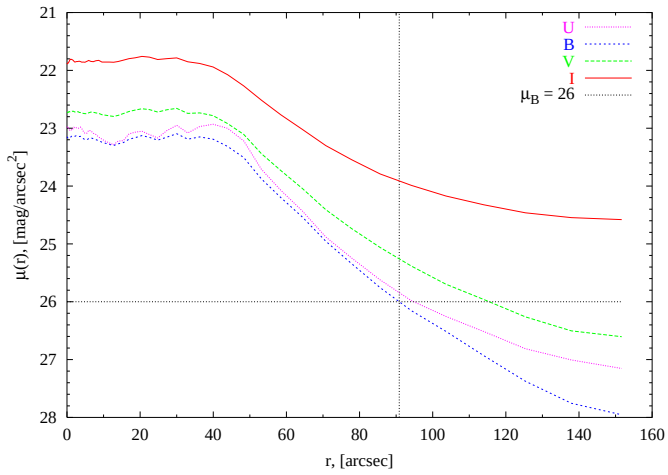

Figure 1.14: The NGC 1427A surface brightness profile in $U, B, V,$ and I-bands. The vertical dotted line indicates the radius of the $\mu_B = 26\,\mathrm{mag/arcsec^2}$ isophote, at which the V-band $\mu_V = 25.6\,\mathrm{mag\ arcsec^{-2}}$ was determined and plotted in Fig. 1.9.

radius of the B-band $\mu_B = 26$ isophote (compare with Fig. 1.14). Another approach was to fit the center on the 41 pix ring aperture smoothed image (see Sect. 1.2.2) using the IRAF centroid algorithm. The result of this centering is shown with a "+" symbol in Fig. 1.9. Based on the NGC 1427A ionized gas kinematics, Chanamé et al. (2000) defined a kinematical center which is indicated with a diamond symbol in Fig. 1.9. The latter two center coordinates are offset with respect to the center defined by the diffuse galaxy light while the adopted geometrical V-band isophote center does not only represent the center of the diffuse galaxy light (stars) but also is the most symmetrical center of the GC candidate distribution around NGC 1427A. In order to check the centering effect we measured the differences of the total galaxy magnitudes assuming the different centers and found negligible deviations below 2 % (0.02 mag). Thus we adopted the isophotal center as a good enough approximation. In Fig. 1.14 the galaxy surface brightness profiles for $U, B, V,$ and I are shown. With the dotted lines the extension of the $\mu_B = 26$ isophote (at $r_1 = 90\farcs9$) is indicated, for which the total magnitude $V_{TOT,1} = 13.06 \pm 0.02$ mag was determined. As can be seen, the surface brightness profile reaches the background level in the I-band approximately at $r_2 = 151\farcs7$. We adopt this truncation radius for the other passbands. The total magnitude at that radius would be $V_{TOT,2} = 12.88 \pm 0.02$ mag. The determination of S_N for both radii will give us information on the radial dependence of the specific frequency in NGC 1427A. Inside r_1 and r_2 we count 23 and 40, respectively.

The correction for contamination is based on the determined level of 0.61 objects/arcsec^{-2} (see Sect. 1.3.3). Thus, for the two radii we determine a correction of 4 and 12 contaminants leading to $N_{\mathrm{GC}} = 19$ and 28, respectively.

Using the adopted distance to Fornax we obtain $M_{V,1} = -18.33 \pm 0.20$ and $M_{V,2} = -18.51 \pm 0.20$ mag. The calculated specific frequencies are $S_N = 0.88$ and 1.09 ± 0.23. Using the distance modulus determined from the GCLF turnover we compute $M_{V,1} = -17.95 \pm 0.21$ and $M_{V,2} = -18.13 \pm 0.21$ mag, which results in the following specific frequencies, $S_N = 1.3$ and 1.6 ± 0.23 for the smaller and larger

aperture, respectively. These S_N-values should be considered as lower limits for NGC 1427A's specific frequency since an age-fading of the galaxy light should be applied to compare it with the S_N of giant early-type galaxies. As Miller et al. (1998) estimated, the final total V magnitude of a galaxy that is forming stars for 5 Gyr at constant rate and then is fading for another 5 Gyr will be fainter by ~ 1.5 mag as during the star forming phase. Assuming that the number of old GCs is conserved, this luminosity evolution will increase the S_N by a factor of ~ 4 during this time. Also, the number of the old GCs could increase of the most massive and/or compact young star clusters, present in the starburst regions, survive the disruptive dynamical evolution.

The S_N value measured here (≥ 1) is higher than typical values for dIrrs (e.g. $S_N \simeq 0.5$ for LMC, Harris 1991) in the Local Group. However, our estimates are comparable with results by Seth et al. (2004) for dIrrs in the Virgo and Fornax clusters, $S_N > 2$, which suggests that the environment influences the GC formation efficiency in dIrr galaxies.

Another approach avoiding the uncertain galaxy light age-fading estimate is to use the T parameter proposed by Zepf & Ashman (1993) which relates the total GC number to the total galaxy mass:

$$T = \frac{N_{\rm GC}}{M_G/10^9 M_\odot} \tag{1.4}$$

where M_G is the total galaxy mass. Chanamé et al. (2000), using a rigid-body rotation model, determined the NGC 1427A angular velocity of $\omega = 12.8 \pm 1\,{\rm km\,s^{-1}\,kpc^{-1}}$. They derive a lower limit of the dynamical mass of $M_G = (9 \pm 3) \times 10^9 M_\odot$ within 6.2 kpc radius corresponding to $\mu_V = 24.7\,{\rm mag/arcsec^2}$. This isophote corresponds to $77\farcs8$ distance from the dynamical center. Within this aperture, after correction for the contamination of 3 objects, we count 19 GC candidates and thus obtain the local T value of 2.1 ± 1. However, the total T value should be used for comparison. We calculate at $r_2 = 151\farcs7 \simeq 12$ kpc the NGC 1427A dynamical mass of $M_G = (6 \pm 3) \times 10^{10} M_\odot$ and $N_{\rm GC} = 28$, which gives $T = 0.5 \pm 1$. This GC formation efficiency per unit mass is smaller but comparable to the T values of spiral galaxies (e.g., Chandar et al. 2004; Goudfrooij et al. 2003; Barmby & Huchra 2001; Kissler-Patig et al. 1999).

1.5 Conclusions

Based on deep VLT observations, we study the old GC population of the dwarf irregular galaxy NGC 1427A. The results of our analysis are as follows. After applying various selection criteria, namely color cuts, point source selection, exclusion of Hα-emitting sources, and a visual inspection of HST/ACS images resulted in 56 GCCs. Accounting for contamination (Sect. 1.3.3) this finally leads to 38 ± 8 globular cluster candidates, likely associated with NGC 1427A. Their radial number density distribution is concentrated towards the galaxy center, which suggests that they belong to this galaxy. The colors of the selected GC candidates show that most of them are metal-poor ($Z \leq 0.08 \times Z_\odot$), old globular clusters (≥ 5 Gyr) according to comparisons with simple stellar population models (Bruzual & Charlot 2003) and colors of the old GCs in the Milky Way. This is in agreement with results from

previous investigations on GCS in dIrr, dSph and dE galaxies (e.g. Sharina et al. 2005; Seth et al. 2004; Lotz et al. 2004), which show that the GCSs in these systems share similar properties, hence similar early star formation histories.

Using the GCLF turnover magnitude as a standard candle, we estimated the distance to NGC 1427A for the first time. We derive a distance modulus of $(m - M) = 31.01 \pm 0.21$ mag (15.9 ± 1.6 Mpc) taking the measured GCLF turnover of $V_{TO} = 23.61 \pm 0.11$ and assuming $M_{V_{TO}} = -7.40 \pm 0.11$ as universal (Harris 2001). If we use the RR Lyrae calibrated GCLF $M_{V_{TO}} = -7.66 \pm 0.09$ (Di Criscienzo et al. 2006) we obtain $(m - M) = 31.25 \pm 0.20$ mag (17.8 ± 1.5 Mpc). The analysis shows that NGC 1427A is placed 3.2 ± 2.5 (statistic) ± 1.6 (systematic) Mpc in front of the giant cD galaxy NGC 1399. If NGC 1427A really is located more than 2-3 Mpc away from the cluster center, the suggested interaction of NGC 1427A with the dense intracluster medium triggering the intense star formation activity would then probably occur at large cluster-centric radii. This result, however, should be taken with precaution considering the uncertainties involved in the GCLF turnover point and the possible systematics in the method itself of about 0.2 mag (for a review see Richtler 2003). More importantly, a precise analysis of the relationship between NGC 1427A and the cluster environment must involve the giant elliptical NGC 1404 as well. We are currently prevented to do this due to the large uncertainties in the relevant distances. However, our relative distance result supports the Drinkwater et al. (2001) finding that the kinematically distinct population of infalling dwarf galaxies in Fornax shows an extended spatial distribution.

We obtained a present-day specific frequency of $S_N = 1.6 \pm 0.23$. However, this galaxy still is actively forming stars. Hence, an age fading of the galaxy's light should be applied prior to compare its S_N value to those of 'old' early-type galaxies. Applying such a correction (according to Miller et al. 1998) would lead to a S_N value of ~ 7 after passive evolution for a few Gyr. The large S_N value suggests that dIrrs could contribute to the blue GC population and its total numbers in giant early-type galaxies through dissipationless merging or accretion. Since they are still actively forming stars and star clusters, they may also contribute to the red GC population by some newly-formed GCs. Those clusters might form out of material that was enriched during the starburst event, probably triggered by the interaction with the cluster environment.

Given the current paucity of deep imaging studies of dIrr galaxies combined with the fact that they are likely building blocks of giant galaxies in the context of the hierarchical merging scenario, we suggest that detailed studies of dIrr galaxies in a range of environments be undertaken to establish their range of GCS properties as a function of environment density. This should provide important constraints on the formation of these galaxies as well as on their global impact on galaxy formation and evolution.

Chapter 2

Old Globular Clusters in Dwarf Irregular Galaxies in Field Environments

Contents

2.1 Introduction

Hierarchical structure formation models envision the assembly of present-day massive galaxies via numerous minor mergers/accretions of smaller galactic entities. Present day dwarf galaxies have masses that are similar to those predicted for the proto-galactic fragments (e.g. Purcell et al. 2007), which were later incorporated into more massive galaxies (e.g. Searle & Zinn 1978). The prediction of the hierarchical growth of major galaxies through merging of many dwarf-sized fragments at early times is manifested by the steepening of the faint-end slope of the galaxy luminosity function with redshift (e.g. Ryan et al. 2007; Khochfar et al. 2007). Furthermore, dwarf irregular galaxies are found to be one of the most abundant galaxy types in the high-z Universe (e.g. Ellis 1997; Stiavelli et al. 2004), and thus are regarded as building blocks of massive galaxies. As nearby dIrrs are less evolved systems than nearby massive galaxies, they might represent the most "pristine" dwarfs that are likely similar to the fragments incorporated into massive halos and therefore hold important clues as to how galaxies formed.

Old globular clusters (GC) are among the first objects to form in the early Universe. As luminous agglomerations of coeval stars with homogeneous metal abundances they represent unique tools for tracing the main galaxies' star formation episodes. Therefore, their properties, as distinct entities and as a system, reflect the physical conditions at the time of their early formation. This will provide us with constraints on the galaxies' early assembly, since dIrrs may well contribute to the

assembly of the rich GC systems (GCSs) of the most massive galaxies.

Numerous observations of the most massive elliptical and spiral galaxies in various environments have shown that they contain exceedingly rich populations of old GCs (e.g. Kundu et al. 1999; Larsen et al. 2001; Dirsch et al. 2003; Harris et al. 2006b; Tamura et al. 2006). Extensive studies were performed in the last decade to understand how such populous GCSs were assembled (e.g. Ashman & Zepf 1992; Zepf & Ashman 1993; Hilker et al. 1999; Goudfrooij et al. 2003; Chandar et al. 2004; Puzia et al. 2004; Rhode et al. 2005; Goudfrooij et al. 2007). These studies led to two important discoveries: i) the bimodal metallicity/color distribution of the GCs (e.g. Ashman & Zepf 1992; Neilsen & Tsvetanov 1999; Gebhardt & Kissler-Patig 1999; Puzia et al. 1999; Kundu & Whitmore 2001) and ii) the presence of young/intermediate age massive star clusters in merging, starburst and irregular galaxies (e.g. Whitmore & Schweizer 1995; Goudfrooij et al. 2001; Puzia et al. 2002; Goudfrooij et al. 2004). As a result, three major galaxy/GCS assembly scenarios have been proposed to explain these findings. The first scenario is the *hierarchical* build-up of massive galaxies through merging and accretion of pre-galactic dwarf-sized gas fragments (Searle & Zinn 1978) in which the metal-poor GCs form *in situ* while the metal-rich GCs originate from a second major star formation event (Forbes et al. 1997) from infalling gaseous fragments, e.g. the mini-mergers at high redshifts (Beasley et al. 2002). The spiral-spiral dissipative galaxy *merger* scenario (Schweizer 1987; Ashman & Zepf 1992) assumes that the metal-poor GCs were formed early in the progenitor galaxies, while metal-rich GCs formed during the major merger events. Finally, the *accretion* scenario incorporates the classical monolithic collapse picture in which the galaxies and their GCs form in the initial starburst (Pipino et al. 2007)and the later accretion of smaller dwarf-sized systems contributed to the assembly of massive galaxies GCSs (Côté et al. 1998; Hilker et al. 1999; Côté et al. 2002; Beasley et al. 2002; Kravtsov & Gnedin 2005). All three scenarios are not mutually exclusive and actually bear a number of similarities; they vary mostly in the amount of gas involved. For extensive discussion on the strengths and weaknesses of the various scenarios we refer the reader to the reviews by Ashman & Zepf (1998); Kissler-Patig (2000); van den Bergh (2000b); West et al. (2004); Brodie & Strader (2006).

Dwarf irregular galaxies play a key role in each GCS/galaxy formation scenario. As dIrrs host mainly old metal-poor, blue GCs (bGCs), the GCSs of massive galaxies, and mainly their bGCs, might be a mixture of clusters formed *in situ* and GCs accreted with the dwarfs through hierarchical merging. Thus, it is very important to study dIrr galaxies to obtain a proper understanding of their GCS properties and what might be their contribution to the blue GC population of massive galaxies, which has so far not yet been possible due to the lack of large enough samples.

Analyzing GCs' metallicities and horizontal branch (HB) morphologies, Zinn (1993) proposed a sub-classification of the Milky Way (MW) GCS into three populations – BD (bulge/disk), OH (old halo) and YH (young halo), where BD are all metal-rich ([Fe/H] > -0.8) clusters, and the metal-poor, OH and YH, are divided by their horizontal branch index, i.e. ΔHB > -0.3 and ΔHB< -0.3, respectively. With the idea that the YHs might be of external origin, first Zinn (1993) and later Mackey & Gilmore (2004) and Mackey & van den Bergh (2005) showed that in many respects the properties (colors, luminosities, spatial distributions, structural param-

eters, HB morphologies etc.) of the MW YH GCs are similar to the properties of GCs in dwarf galaxies (LMC, SMC, Fornax, Sagittarius). Recently, Lee et al. (2007) showed that GCs with extended horizontal branches (EHB-GCs) are decoupled in their orbital dynamics and mass from the rest of the GCs and confirmed the Zinn (1993) conclusion that the YH clusters are dominated by random motions and share the hot kinematic properties of EHB Galactic GC population supporting their probable external origin. This, and evidences of tidal streams around the MW and M31 (e.g. Ibata et al. 2001; Martin et al. 2004; Kalirai et al. 2006) further supported the view by Searle & Zinn (1978) that a fraction of the GCs were formed in isolated low-luminous satellite building blocks, which were later accreted.

The present study focuses on the GC properties (luminosity, color, structural parameters, spatial distribution and specific frequencies) of dIrr galaxies in groups and associations of only dwarf galaxies. The observational data, its reduction, GC selection and photometry are described in Sect. 2.2. The results are presented and summarized in Sect. 2.3, where the properties of GC candidates are discussed and compared with the Galactic YH GCs. Additionally, we address the question whether these dIrrs can be the progenitors of the present day dE/dSph by comparing their GC specific frequencies (S_N) with those of early-type dwarfs in clusters (e.g. Miller et al. 1998; Seth et al. 2004; Forbes 2005; Strader et al. 2006; Miller & Lotz 2007).

2.2 Observations

2.2.1 HST/ACS data

The current study uses HST archival data of 20 Magellanic-type dwarf irregular (dIrr) galaxies located in nearby ($d = 3-8$ Mpc) loose groups(associations) of dwarf galaxies (Tully et al. 2006). They were observed in the F606W and F814W filters with HST/ACS during Cycle 13, program GO-10210 (PI: B. Tully). The split into two non-dithered exposures was designed to reach ~ 2 mag beyond the Tip of the Red Giant Branch (TRGB) luminosity at $M_I = -4.05, (M_V = -2.5)$ (Da Costa & Armandroff 1990; Lee et al. 1993) in order to derive the TRGB distances to these groups/associations of (dIrr) galaxies. Accurate distances to these galaxies are published in Tully et al. (2006), which provides us with an excellent tool to study the properties of the GCSs of these dwarfs.

2.2.2 Initial photometry

The retrieved archival images were processed with the standard HST/ACS archival pipeline. In order to improve the object detection and initial photometry, the diffuse galaxy light was modeled and subtracted by convolving the images with ring aperture median kernel of 41 pixel radius. Then, on the residual images we used the IRAF[1] DAOPHOT/DAOFIND routine to detect objects with > 4-σ above the background. Photometry for all detected sources was performed with the DAOPHOT/PHOT routine in apertures of $2, 3, 5$ and 10 pixel radius. To convert the instrumental magnitudes to the ST magnitude system an aperture correction

[1]IRAF is distributed by the National Optical Astronomy Observatories, which are operated by the Association of Universities for Research in Astronomy, Inc., under cooperative agreement with the National Science Foundation.

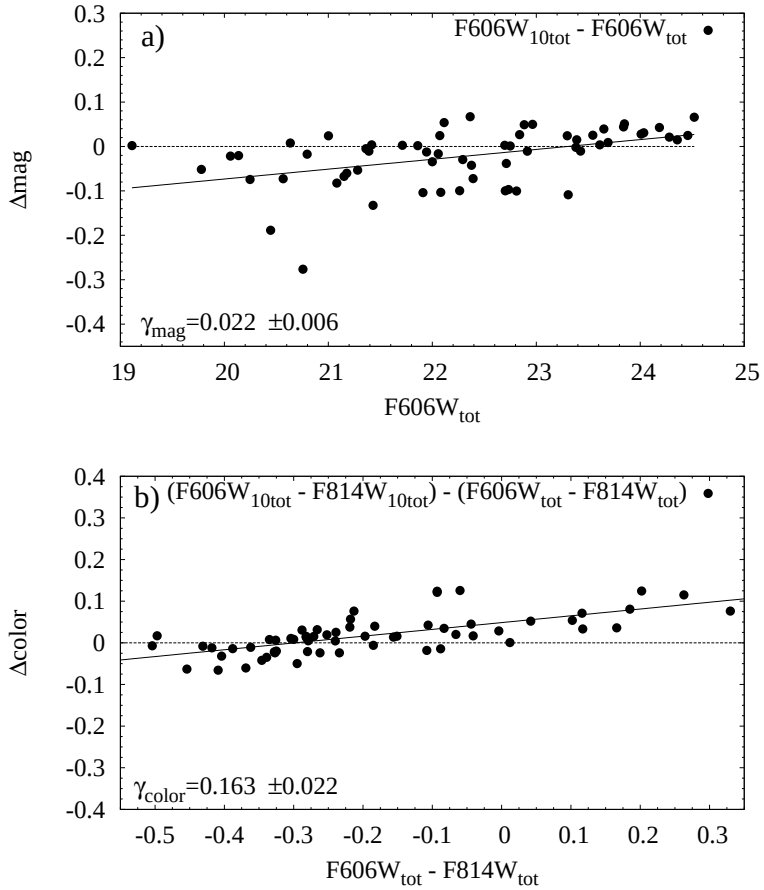

Figure 2.1: Constant aperture correction is color and magnitude dependent. In panel a) are shown the magnitude difference derived from the individual curves of growth for each GC candidate ($F606W_{tot}$ magnitudes) versus the magnitudes simply corrected with a constant value from 10 pixels to infinity ($F606W_{10tot}$). Analogously, in panel b) we show the same relation for the objects' colors. The thick line is the least-square linear fit to the data and γ is the slope of the fit. It is seen that, even when excluding the faintest objects, which are also the reddest ($F606W_{tot} - F814W_{tot}) > 0.1$), a simple aperture correction is magnitude and color dependent.

from 10 pixel aperture to infinity was applied, using the zero points and aperture correction values from the ACS photometric calibration by Sirianni et al. (2005). The magnitudes derived this way are labelled in the following with the subscript '10tot'. These magnitudes were only used for the GC selection, while the final GC magnitudes were determined as described in Section 2.2.5.

2.2.3 Aperture corrections

The typical size of a GC, containing half of its light, is about 3 pc. Therefore, the GCs in the galaxies in our sample are expected to be resolved on ACS images, and typically their light extends beyond 10 pixels, which can introduce systematic errors in the aperture correction. We explore how this error affects our GC selection criteria. In Figure 2.1 are shown the differences between the corrected ($F606W_{10tot}$; see above) aperture magnitudes (Fig. 2.1 a) and colors (Fig. 2.1 b) and the "true" magnitudes ($F606W_{tot}$) derived from curves of growth for each GC (see Sect. 2.2.5).

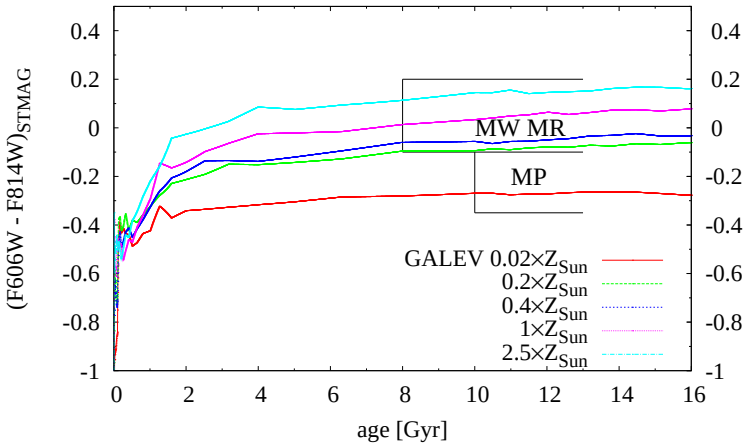

Figure 2.2: The initial GC selection was based on SSP evolutionary models in the ACS/WFC filter system for different metallicities (Anders & Fritze-v. Alvensleben 2003). Namely, objects with colors $-0.4 \lesssim$(F606W-F814W)$\lesssim 0.2$, i.e. objects older than $\gtrsim 4$ Gyr for the whole range of metallicities. With rectangles are shown the typical color ranges for Galactic metal-poor (MP) and metal-rich (MR) GCs.

The Sirianni et al. (2005) aperture corrections are computed for point sources, however, in the case of resolved GCs this correction will be insufficient and introduce an offset in the GCs' magnitudes. Figure 2.1 shows that this effect appears to be magnitude and color dependent. The dashed lines indicate the zero offset, the thick lines a linear fit to the data and γ is the slope of the fit. The observed magnitude dependence can be understood in the sense that the brighter the object the more extended it is. Thus, the correction is underestimated for brighter GCs while it is overestimated for the fainter ones, when a constant aperture correction was applied to all GC candidates. The color dependence of the aperture correction is even more significant (Fig. 2.1 b). Even when the reddest ((F606W$_{10\mathrm{tot}}$–F814W$_{10\mathrm{tot}}$) > 0.1) objects are excluded as likely background galaxies, the color dependence does not change significantly. Hence, a constant aperture correction could affect the clusters' colors by up to 0.1 mag. This result has significant implications for studies dealing with similar quality data.

2.2.4 GC Candidate Selection

Our goal is to study the old GC population in these dIrrs. Thus, our GC candidates selection criteria targets GCs with ages older than ~ 4 Gyr for a range of metallicities as provided by the GALEV Simple Stellar Population (SSP) models in the ACS filter system (Anders & Fritze-v. Alvensleben 2003). Therefore, we restrict the color selection limits to $-0.4 \lesssim (\mathrm{F606W} - \mathrm{F814W})_{\mathrm{STMAG}} \lesssim 0.15$. As seen in Fig. 2.2, the limit at (F606W-F814W)$_{\mathrm{STMAG}} \approx -0.4$ mag (corresponding to Johnson/Cousins $V - I \approx 0.7$) is 0.1 STMAG bluer than the most metal-poor GALEV model. With rectangles in Fig. 2.2 are shown the typical color ranges for metal-poor (MP) and metal-rich (MR) Milky Way GCs. Comparison with Bruzual & Charlot (2003) SSP models show that evolutionary tracks with $0.02 \times Z_{\odot}$ and $0.005 \times Z_{\odot}$ have $V - I$ colors literally indistinguishable for ages older than 4 Gyr. Therefore, our color limit

at (F606W-F814W)$_{\rm STMAG} > -0.4$ selects GC candidates with ages older than 4 Gyr and $(V-I) > 0.7$ mag. Considering the weak dependence of $(V-I)$ colors on metallicity, our GC candidates might be as metal-poor as $0.005 \times Z_{\odot}$.

Since our GC selection is based on effects mentioned in Sect. 2.2.3 as well. Given the small dispersion in the faint magnitude bins seen in Fig. 2.1 a, the effect of the aperture correction on the initial GC selection is negligible. Therefore, we adopt a faint magnitude selection limit at the TRGB, i.e. $M_V = -2.5$ ($M_I = -4.05$) (Da Costa & Armandroff 1990; Lee et al. 1993), which is ~ 5 mag fainter than the typical GC luminosity function turnover magnitude at $M_{V,TO} = -7.4$ mag (e.g. Harris 1996, 2001). This absolute magnitude was converted to apparent magnitudes using the distance modulus for each galaxy as derived by Tully et al. (2006).

To correct for foreground Galactic extinction we have used the $E(B-V)$ values towards each galaxy from the Schlegel et al. (1998) dust maps[2]. We used the Galactic extinction laws by Cardelli et al. (1989) (their eqs. 2 and 3) to compute the values for the ACS filters.

As mentioned above, due to the deep imaging and high ACS spatial resolution, the GCs in our images show profiles significantly more extended than point sources (stars). In order to include this knowledge in the GC selection we used IMEXAM to obtain initial information on the profiles of all detected objects as first approximation for the GC selection. We considered as GC candidates round objects (FWHM$_{F606W} \simeq$FWHM$_{F814W}$, ellipticity≤ 0.15) with $2 \lesssim$FWHM$\lesssim 9$ pix (the measured stellar FWHM was ~ 1.7 to 1.9 pix). The IMEXAM ϵ and FWHMs were measured with fixed $r = 5$ pix aperture radius and Moffat index $\beta = 2.5$, typical for stellar profiles. Hence, their absolute values cannot be taken as final result but rather as *upper* limits for the initial selection criteria. The final ellipticities and half-light radii (ϵ, $r_{\rm h}$) were measured with ISHAPE (Sect. 2.2.6). As seen in Fig. 2.15 and 2.17, the derived ϵ values for final GC candidates reach 0.3, a typical upper value observed for old GCs in the Magellanic Clouds and our Galaxy (Fig. 2.16, 2.17). Therefore, the adopted for initial selection IMEXAM $\epsilon < 0.15$ within $r = 5$ pix, should not have introduced an artificial bias in our selection, as can be expected for such resolved objects. An additional check, with an increased ϵ selection limit, proved to include large number of contamination due to blends and nuclei of background galaxies.

The selection process is illustrated in Figure 3.3, with UGC 685 as an example. In Fig. 3.3 a) we show the color–magnitude diagram (CMD) for all UGC 685 objects satisfying the aforementioned size selection criteria. The dashed box indicates the color and magnitude selection limits (see above). The observed dispersion in our CMD is simply due to crowding effects leading to the uncertainties in the 10 pix photometry. Hence, stars affected by their neighbors in crowded regions will show 'wrong' colors and increased color dispersion.

As the GCs are expected to show concentrations different to stars and background galaxies, we incorporate this information by calculating the difference between the 2, 3 and 5 pixel aperture photometry. In terms of contamination, the m_2-m_3 index is the more robust star–GC–background galaxy discriminator than the m_2-m_5 index. This is due to the increase of contaminating light from resolved Galactic stars with increasing aperture size. The GCs occupy a specific locus in the FWHM vs. m_2-m_3 or m_2-m_5 plane, typical for resolved objects.

[2]http://nedwww.ipac.caltech.edu/

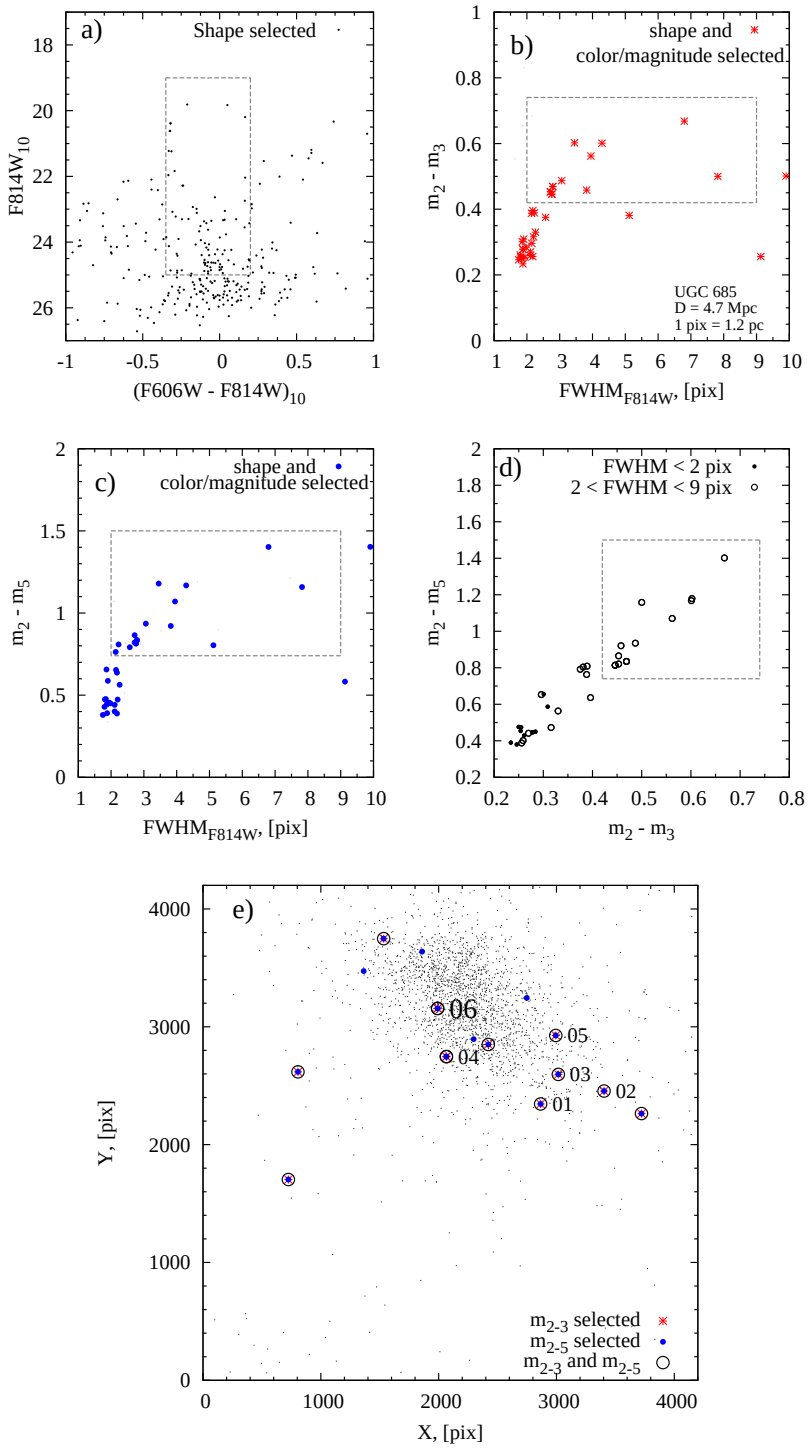

Figure 2.3: Summary of the initial GC selection process for UGC 685. In Panel a) are shown the color and magnitude selections. They are indicated by a rectangular region (dashed box) for all objects obeying the shape selection criteria (IMEXAM $\epsilon < 0.15$; $\mathrm{FWHM}_{F606W} \simeq \mathrm{FWHM}_{F814W}$). In panels b) and c) are shown the objects selected this way which were analyzed against their FWHM and light concentration (both $m_2 - m_3$ and $m_2 - m_5$). In panel d) are shown the two concentration parameters against each other. The objects within the dashed box were selected as GC candidates. Panel e): the selected GC candidates (circled) are shown with different symbol types. The candidates which after visual inspection were regarded as GCs are labeled. See Sect. 2.2.4 for detailed explanation.

In Fig. 3.3 b) and c) we show the concentration m_2-m_3, m_2-m_5 indices versus the measured $FWHM_{F814W}$ for all color, magnitude and shape selected objects (IMEXAM $e < 0.15$, $FWHM_{F606W} \simeq FWHM_{F814W}$). The dividing line around $m_2-m_3 \simeq 0.4$ and $m_2-m_5 \simeq 0.75$ mag separates stars from GC candidates. However, the bulges of resolved big galaxies and barely resolved compact (FWHM$<$ 9 pix) background galaxies fall in the same region as the GCs (see also Puzia et al. 2004). In Fig. 3.3 d) the two concentration indices are plotted against each other. The dotted box shows the region occupied by the GC candidates. It can be seen that if we were to select GC candidates from the m_2-m_5 index alone, we would have introduced more contamination (shown with blue dots) from blended sources within the galaxy. The completeness and contamination issue is discussed in more detail in Sect. 2.2.7.

In the case of UGC 685, the automated GC selection procedure returned 13 objects, which were visually inspected. 5 obvious background galaxies and 2 blends were removed leaving 6 GC candidates which are shown with numbered IDs in Fig. 3.3 e) (see also Fig. 2.6). Four of the five objects with $\bar{m}_{2-3} \simeq 0.4$ and $\bar{m}_{2-5} \simeq 0.7$ in Fig. 3.3 e) were visually inspected and turned out to be blended sources in the galaxy body, one was a clear background galaxy. The same was the case in the rest of the studied galaxies, therefore we adopted the lower limit for concentration selection at the quoted values above. The same technique was applied to all our sample galaxies. The final GC candidate sample comprises 60 objects in 13 out of the 19 examined dIrr galaxies.

After the presented selection process, the contamination in our GC sample by unresolved background galaxies cannot be ruled out entirely. Completeness, however, is not an issue due to the depth of the images, with 90% point source limiting magnitude at $M_V = -2.5$ mag. Therefore, we are confident that we do not introduce any unaccounted artificial bias in our GC selection. A similar selection of GC candidates in nearby LSB dwarf galaxies was recently confirmed with 96% success rate by radial velocities (Puzia & Sharina 2008).

2.2.5 Final Globular Cluster Candidate Photometry

Accurate photometry of the total light of resolved GCs, including virtually all cluster light, was based on individual curves of growth which account for the different GC sizes due to the varying distances to the host galaxy. However, in images where a significant part of the host galaxy stellar component is resolved a special treatment of the contaminating sources (galaxy stars, complex stellar regions, foreground Galactic stars, background galaxies), found in the photometric apertures, is needed. In order to eliminate the contaminating sources and build curves of growth up to 50 pixel aperture radius, we used the SExtractor (Bertin & Arnouts 1996) package. Measuring the GCs' magnitudes with SExtractor turned out to be an unstable task leading to very uncertain measurements especially for objects in crowded regions. Instead, we used the SExtractor option "CHECKIMAGE_TYPE -OBJECTS" to detect and subtract iteratively in two steps contaminating objects having different profiles. For their detection two different convolution filters were used, provided within SExtractor, i.e. gauss_5.0_9x9.conv and gauss_1.5_3x3.conv.

The iterative procedure is illustrated in Figure 2.4 where two cases with strong contamination are shown. In the lower row the brightest star on the right was masked out. The two iterative steps were designed to detect and subtract only

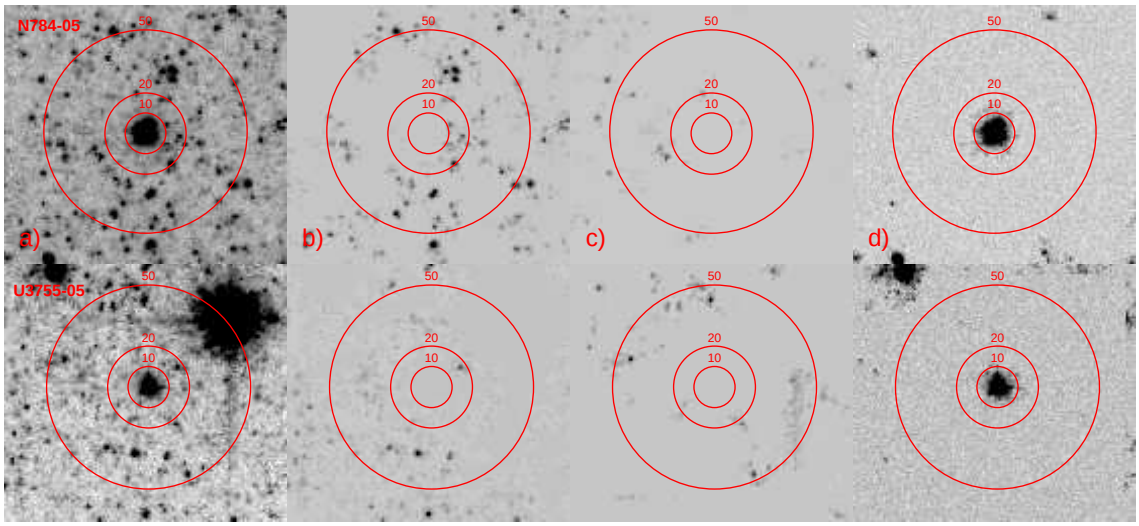

Figure 2.4: An illustration of the reduction process of iterative cleaning of the photometric apertures around the GC candidates in two extreme cases with strong contamination by resolved galactic stars and a nearby bright foreground star. As discussed in the text, two cleaning iterations (columns b) and c)) using SExtractor were involved to remove the underlying galaxy light and contaminating sources within the photometric apertures. The CCD image noise characteristics were restored with MKNOISE (column d). Aperture photometry and curves of growth were build from the images reduced this way.

sources with the given filter profiles from the images and replace them with the background value as evaluated by a 60-pixel background mesh. This allowed us to adjust the detection thresholds such that (as a first step) the GC with the associated pixels within $0.5\,\sigma$ of the background (thus practically loosing no light from the GC) was subtracted from the original image. The image of this step, containing only contaminating objects, (Fig. 2.4 b) was then subtracted from the original (Fig. 2.4 a), thus removing only the contaminants. The second iteration used the narrower convolution filter and the object detection was setup such that the GC was detected and subtracted from the result of the first iteration (Fig. 2.4 c). Then this image was subtracted from the result of the first iteration, thus removing the last contaminants (see Figure 2.4 d). Since SExtractor replaces the detected sources with a constant background value, we used the ACS CCD characteristics from the image header and restored the detector noise in the image with the IRAF MKNOISE routine. This step was mainly performed to restore the proper error budget in the photometry. The circles in Fig. 2.4 mark some of the aperture radii used in our curve of growth photometry.

In order to build individual curves of growth, an aperture photometry from 5 to 50 pixels with a step size of 5 pixels was performed with the DAOPHOT/PHOT task on the final images (free of contaminants). Fifth-order polynomial fits to the curves of growth were used to derive the magnitudes for each GC. In order to compare our GC magnitudes with those of other GC studies we iteratively converted the instrumental STMAG magnitudes from ACS/WFC filters to the Johnson/Cousins V and I magnitudes using the synthetic transformation coefficients computed by Sirianni et al. (2005).

2.2.6 Globular Cluster Sizes

With the spatial resolution (0.05 arcsec/pixel) of the ACS/WFC the GCs in these nearby (2 to 8 Mpc) dIrrs are clearly resolved. This enables one to measure their structural parameters with relatively high precision.

The GC half-light radii (r_h) were estimated using the ISHAPE algorithm (Larsen 1999), which models the source as an analytic function convolved with a (model) point-spread function (PSF). For the PSF model we used the TINYTIM software package[3]. It properly takes into account the field-dependent WFC aberration, filter passband effects, charge diffusion variations and varying pixel area due to the significant field distortion in the ACS field of view (Krist & Hook 2004). We have used the GCs coordinates to create ten times sub-sampled model PSFs at the position of each GC. When sub-sampling is enabled, TINYTIM doesn't convolve the PSF with the charge diffusion kernel (CDK), but provides its values in the PSF image header. As it is position and wavelength dependent we generated an individual CDK for each GC, which was later used with ISHAPE in the profile fitting process.

Assuming a King (1962) model for the intrinsic radial luminosity profile of the clusters, the clusters $F606W$ images were modeled with all concentration parameters $C = r_t/r_c = 5, 15, 30, 100$ provided by ISHAPE. An 8 pixel fitting radius was used. The FWHM of the best χ^2 model was adopted for the objects. To test the stability of the measured FWHMs we varied the fitting radius in the range 4 to 10 pix corresponding from $\sim$ 6 to 15 pc. No significant trend and practically identical FWHMs were returned by ISHAPE. In order to convert from FWHM to $r_{\rm h}$ we used the conversion factors tabulated for KING models with different C by Larsen (2006). However, this relation is valid for circularly symmetrical profiles while the output of ISHAPE is the FWHM along the major axis (w_y). In order not to overestimate the $r_{\rm h}$ by simply assuming its measured $r_{{\rm h},w_y}$ value, a correction considering the ratio of the FWHMs along the minor and major axes (w_x/w_y) should be applied. Therefore we adopted for the "true" effective radius the geometric mean of the FWHMs along the two axes, i.e.

$$r_{\rm h} = r_{{\rm h},w_y}\sqrt{w_x/w_y} \tag{2.1}$$

where w_x/w_y is the ISHAPE output of the minor/major axes FWHMs ratio. The comparison between $r_{\rm h}$ values derived this way and the numerically derived correction (eq. 11 in Larsen 2006) resulted in absolutely identical values. The analysis and interpretation of the GCs sizes derived as described above is presented in Sect. 3.2.4.

2.2.7 Completeness and Foreground/Background Contamination

Given the depth of the imaging data, incompleteness is not an issue since our lower magnitude for GC selection is $\sim$ 2 mag above the designed photometric limit of the images for each galaxy (see Sects. 2.2.1 and 2.2.2). Further, all dIrr galaxies in our sample have very small radial surface brightness gradients which do not bias the completeness towards the galaxy center and therefore no radial completeness tests are required.

[3] http://www.stsci.edu/software/tinytim/tinytim.html

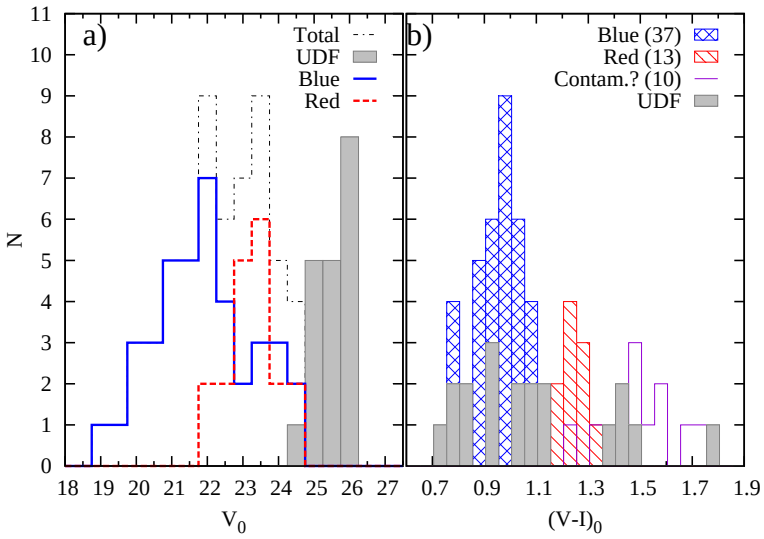

Figure 2.5: Apparent V-band luminosity (panel a) and color (panel b) distribution of the expected Hubble UDF background contamination (filled histograms). The dashed-dotted line, in panel a) shows the luminosity distribution of all GC candidates in our sample while with thick (blue) and dashed (red) histograms show the candidates divided by their color into blue and red GCs, respectively (Sect. 2.3.1).

Although the supreme ACS resolution and deep exposures allowed us to reject foreground stars and background galaxies at high confidence, compact background galaxies at intermediate redshifts may share the same color, magnitude and size properties as the GCs (e.g. Puzia et al. 2004). In order to assess this type of contamination we used the Hubble Ultra Deep Field (HUDF) images. An ideal way to estimate the contamination from the HUDF is to run the same image reduction, selection and photometry procedures. However, the lack of F814W imaging in HUDF prevents us from performing this task. Therefore, we selected objects having the same characteristics as the GCCs in our F606W images, from the HUDF catalog[4], i.e. $19 < V_{\rm F606W} < 26$ mag, ellipticity smaller than 0.15 and $2 <$ FWHM < 9 pix. Note that $V_{\rm F606W} \sim 26$ mag is equal to the magnitude limit we used for the most distant galaxies in our sample (i.e. UGC 3974, UGC 3755 at $\sim$ 8Mpc), therefore the above set of parameters for selecting objects from the HUDF will be exposure independent. Thus, the objects in the HUDF and our fields should be similarly resolved up to the magnitude limit used for selection.

After selecting HUDF objects this way, we converted their magnitudes to the Johnson/Cousins system using the Sirianni et al. (2005) transformation coefficients and show their magnitude and color distributions in Figure 2.5. The dashed-dotted line, in Fig. 2.5 a), shows the apparent magnitude distribution of all GC candidates in our sample while the solid (blue) and dashed (red) histograms show the candidates divided by their color into blue and red GCCs, respectively (see Sect. 2.3.1). We overplot the HUDF objects with a shaded histogram. While covering the same $(V - I)$ color distribution as the GC candidates (Fig. 2.5 b), the expected HUDF contamination from background galaxies starts to be a significant factor at faint

[4]http://heasarc.gsfc.nasa.gov/W3Browse/all/hubbleudf.html

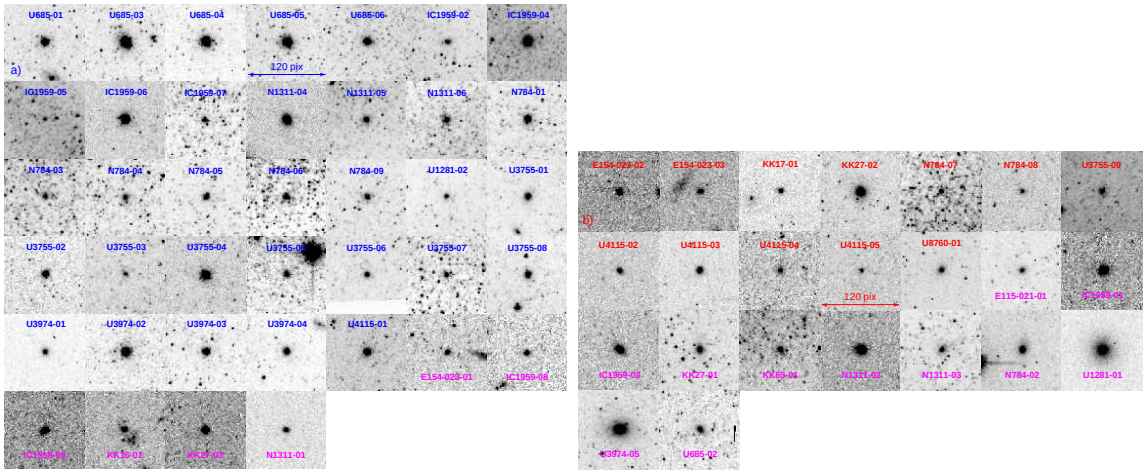

Figure 2.6: 120×120 pix F814W excerpts for all GC candidates. Labels on the top of the images indicate the name of the host galaxy and the sequence number of the GC candidate. Panel a) shows the GCs with $0.7 < (V-I)_0 < 1.15$ mag. The last eight GCs, having their labels in the bottom of the image, are the faintest and reddest candidates among the blue population (compare with Fig. 2.7 and Fig. 2.9), thus are likely background contaminants. Panel b) shows the red ($(V-I)_0 \gtrsim 1.15$ mag) group of objects. Although excluded from the analysis, just for comparison we show U 1281-01 and U 3974-05, the brightest objects in this group, having extended halos perhaps suggesting that they are background galaxies. This demonstrates that even with the supreme ACS resolution only spectral analysis can resolve all doubts regarding their nature, especially for objects like U 3974-05.

apparent magnitudes, $V_0 \gtrsim 24$ mag, as seen in Fig. 2.5 a). Hence, we might expect contamination only in the last one or two magnitude bins. Given that in Fig. 2.5 we combine the GC candidates from 15 individual ACS fields we need to multiply the number of HUDF contaminating objects by 15. Considering the apparent magnitude distribution of the blue and red GC candidates and the properly scaled HUDF contaminants, our upper estimates are 6 and 9 contaminants, respectively.

In Figure 2.6 we show 120×120 pix F814W image excerpts for all GC candidates. With blue and red labels in Fig. 2.6 a), b) are indicated the GCs bluer or redder than $(V-I)_0 = 1.1$ mag, respectively. The objects with labels at the bottom (in magenta) in Fig. 2.6 a) and b) are the reddest GCs with $(V-I)_0 > 1.4$ mag (cf. Fig. 2.7 and 2.9) which are very likely background contaminants. Fig. 2.6 shows that the probable contaminants are indistinguishable in appearance from the blue GC candidates in the ACS images.

Red GCs are unlikely to be observed in metal-poor dIrr galaxies because such red metal-rich GCs are believed to be forming mainly in massive galaxies. This question will be further addressed in Sect. 2.3. Therefore, in the following sections our analysis will be mainly focused on the blue GCCs.

2.3 Analysis

2.3.1 Magnitudes and Colors

Given the low luminosities ($M_V \gtrsim -17$ mag, see Table 2.2) of the dwarf galaxies in our sample and the expected low GC specific frequency for dIrr galaxies in group

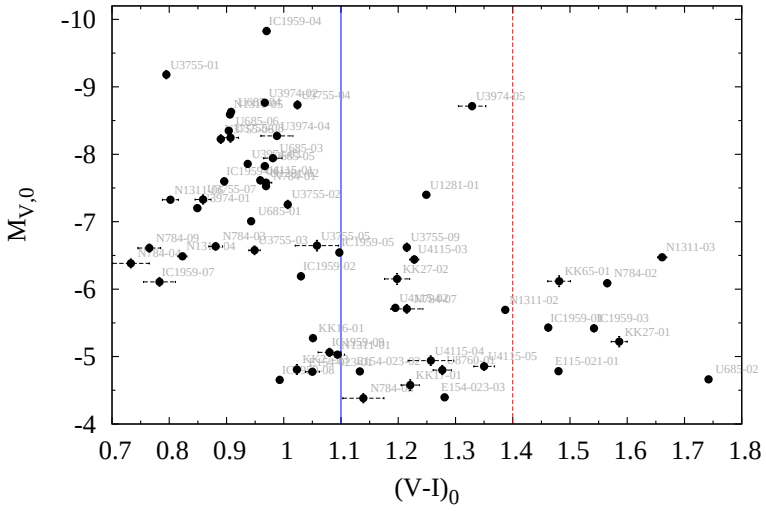

Figure 2.7: Color-magnitude diagram for all objects that passed the GC selection criteria (Sect. 2.2.2). The colors of the bulk of the GC candidates are consistent with old metal-poor GCs. The labels indicate the host galaxy and the number of the GC candidates in that galaxy. The GC candidates colors and magnitudes were dereddened for foreground Galactic extinction using the Schlegel et al. (1998) dust maps. With thick solid and dashed vertical lines are indicated the colors separating blue and red GCs.

environments (e.g. the Local Group, Harris 1991) one would expect to find one old GC in each of these galaxies. However, our analysis, shows that several of the faint dwarf galaxies actually harbor more than one GC candidate. As expected, most of the candidates show blue $(V-I)$ colors consistent with old metal-poor GCs. Figure 2.7 shows the combined color–magnitude diagram for all GC candidates selected among the 19 dIrrs in our sample (Sect. 2.2.2), that fulfill the color, magnitude, size criteria and passed the additional visual inspection which excluded background galaxies or blends from the final list. Other studies (e.g. Seth et al. 2004; Sharina et al. 2005; Georgiev et al. 2006) of old GCs in dwarf irregular galaxies outside the Local Group showed that the GCs are typically constrained within the color regime $0.8 < (V-I)_0 < 1.1$, which corresponds to > 5 Gyr old, metal-poor ($Z < 0.02 \times Z_{\odot}$) GCs according to the SSP models (e.g. Bruzual & Charlot 2003). Compared with the SSP models, the two very blue ($(V-I)_0 < 0.7$) GCCs (NGC 784-05,06) are likely intermediate-age star clusters with an upper age limit of $\lesssim 2$ Gyr. These two were therefore excluded from our analysis since we are interested only in the old GC population. The population of red objects ($(V-I)_0 > 1.1$) in our CMD, which passed our initial selection criteria, most likely is explained by unresolved, redshifted compact galaxies. Further, such red, possibly metal-rich GCs, are not expected in dIrrs although few of them were observed by Olsen et al. (2004) in Sculptor group late-type dwarfs. It is possible that some of the GCs might be reddened, in which case a dependence of their colors with the galactocentric distance would be expected. It is seen from Figure 2.8 that such a dependence is not present. In fact, we see some evidence for a redder color with increasing projected distance. Given the low number statistics, this trend could be due to unresolved background contaminants in the galaxies' outer regions.

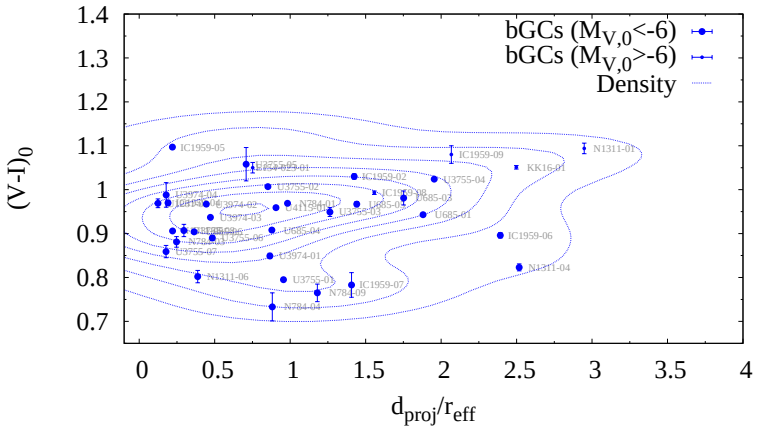

Figure 2.8: Color vs. projected distance for the blue GCs. The iso-lines of the two dimensional density estimate shows that there is no hint for GCs colors becoming redder with decreasing projected distance, as it might be expected due to internal reddening within the host galaxy.

However, follow-up spectroscopy is needed in order to constrain their nature. The two bright and red objects ($M_V > -7$ mag, $1.2 < (V-I)_0 < 1.4$) in Fig. 2.7 (UGC 1281-01, UGC 3974-05) show slightly different (more complex) profiles compared to the rest of the GC candidates and therefore are most probably background contaminants. We therefore also exclude these from subsequent analysis. Objects redder than $(V-I)_0 > 1.5$, although compact and morphologically similar to the bluer GC candidates, are deemed background contaminants. The structural parameters of these objects are discussed in Sect. 3.2.4.

A detailed examination of Fig. 2.7 reveals that there seems to be a lack of faint blue GCs in our CMD ($(V-I)_0 < 1; M_V \lesssim -6$ mag). We have extensively tested the reliability of this observation, by loosening our size/shape selection criteria (the limiting IMEXAM ellipticity and $\mathrm{FWHM}_{F606W} \simeq \mathrm{FWHM}_{F814W}$ cutoffs). This resulted in an increased number of contaminating blended stars in crowded regions. Therefore this lack of faint bGCs is not due to incompleteness or biased GC selection introduced by our size discrimination criteria (see Sect. 2.2.2). However, we do find GC candidates redder $(V-I)_0 \sim 1$ and fainter than $M_V \sim -6$ mag, which are likely background contaminants. This issue is further discussed in Sect. 2.4.1.

In Figure 2.9 we present the combined luminosity and color distributions of all GC candidates, without the excluded objects as discussed above. In order to probe the underlying distributions we run a non-parametric probability density estimator using Gaussian and Epanechnikov (inverted parabola) kernel, shown with solid and dashed lines in Fig. 2.9 a). Although the Gaussian kernel shows better the dip at $(V-I)_0 \sim 1.1$ between the red and blue objects, both kernels give similar color number density probability distributions, with maxima and minima at the same colors. The third peak represents the population of very red objects, i.e. contaminating background galaxies. The highest probability density peak values are at $(V-I)_0 \sim 0.96$ and $(V-I)_0 \simeq 1.19$ for the blue (bGC) and red GCs, respectively. The peak $(V-I)$ color of the bGCs is similar to the one found in other dIrr galaxies (e.g. Seth et al. 2004; Sharina et al. 2005; Georgiev et al. 2006). Although our GC sample might have reddening uncertainties, it is anticipated that it is not a significant factor for these

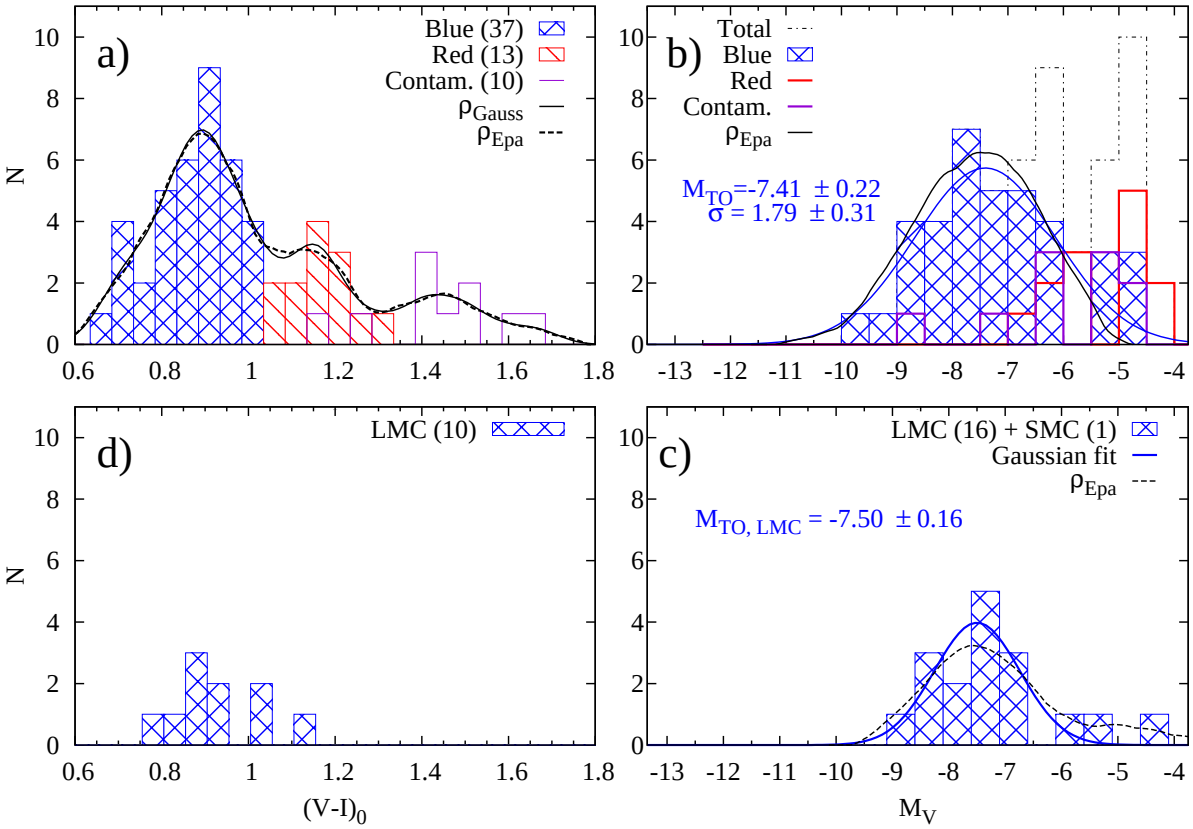

Figure 2.9: Color and luminosity functions (panels a and b) of all GCCs detected in 15 dIrr galaxies. The blue histogram marks the likely GCs, while the likely background contaminants are plotted as red histogram. With thick and dashed lines are shown the non-parametric density estimates using Gaussian and Epanecknikov kernels. Panel b) shows the increasing number of objects in the red group with decreasing magnitude, which is mainly due to background contamination (see Sect. 2.2.7 and Fig. 2.5). To compare the LF of the GCs in our sample with that of the Magellanic-type dIrrs, panels c) and d) show the LF of old GCs in the LMC, SMC and Fornax dwarf galaxy (data from McLaughlin & van der Marel 2005).

extremely low-mass galaxies. Based on H_α fluxes James et al. (2005) showed that dIrrs posses low $A_{H_\alpha} \simeq 0.5$, which translates to $E_{B-V} = 0.06$ or $E_{V-I} = 0.07$ mag. Note, however, that this only refers to the star forming regions.

The luminosity distribution of the bGCs in our sample peaks at $M_{TO,V} = -7.43$ (rather typical for massive galaxies) and has a broader dispersion than the observed LF for the LMC, SMC and Fornax dwarf galaxies (data from McLaughlin & van der Marel 2005), shown in Fig. 2.9 c). The broader luminosity distributions might be partly attributed due to the distance uncertainties to these dwarfs of $\sigma(m - M) \simeq 0.05$ (Tully et al. 2006). A Kolmogorov–Smirnov test gives a 49% probability that the M_V distribution of our bGCs are drawn from those of the LMC. In comparison with other low-mass dIrr galaxies ($M_{TO,V} \sim -6$; Sharina et al. 2005; van den Bergh 2006) the bGCs in our sample show a brighter M_{TO}.

It is interesting to note that the LMC data from McLaughlin & van der Marel (2005), which is the re-calibrated and extended version of the LMC data from Mackey & Gilmore (2003a,b), gives a brighter peak magnitude at $M_{TO,V} = -7.50 \pm 0.16$ mag (highest probability density peak at $M_V = -7.52$ mag) versus $M_{TO,V} =$

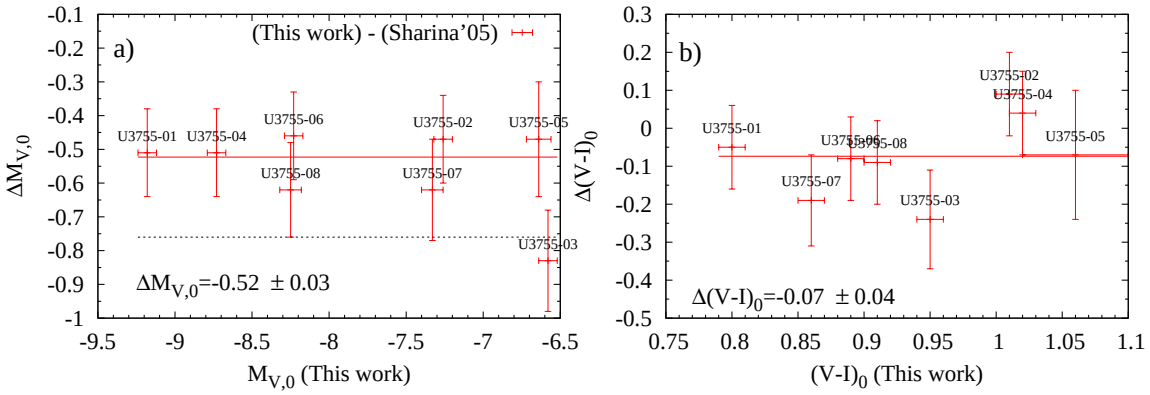

Figure 2.10: Differences in absolute magnitudes and colors for our GCs in common with Sharina et al. (2005). The least-square fit to the data (solid line) shows that our magnitudes are 0.5 mag brighter than the earlier study, while the expected difference due to distance modulus is –0.76 mag (dotted line). The colors (within the errors) are basically identical between the two studies.

−7.31 mag, derived from fitting the formerly determined M_V values of old LMC GCs (Table 2 in van den Bergh & Mackey 2004). Given the uncertainties, this suggests that the GCLF of old GCs for the dIrrs in our sample, and LMC (considering the uncertainties), both peak at similar magnitudes.

Much fainter M_{TO} values were found for other dIrrs by Sharina et al. (2005) using WFPC2 data. However, some of the galaxies included in their study (eg. KK 16, UGC 8651, UGC 4115, UGC 3974, UGC 3755) were re-observed with much deeper ACS observations by Tully et al. (2006). For these dIrr the distance moduli were improved and some of them turned out to be more distant than thought before. Therefore, underestimating the distance to some galaxies of the Sharina et al. (2005) sample led to an underestimate of the GCs' absolute magnitudes, and hence the M_{TO} magnitude. The larger distances also have an effect on the GC half-light radius estimates (see Sect. 3.2.4). For the GCs in common with the Sharina et al. (2005) study in UGC 3755, the differences in absolute magnitude between both studies are mainly due to the improved photometric technique we used for deriving the clusters apparent magnitudes and the new distance moduli. Figure 2.10 shows the differences between both studies. However, the faintness and broadness of the Sharina et al. (2005) GC LFs is not expected to be influenced by contamination from background galaxies since their estimated contamination level is less than $\sim 5\%$ for objects with $(V-I)_0 < 1.2,\ -5.3 < M_{V_0} < -6.3$ mag (Puzia & Sharina 2008).

2.3.2 Comparison with the Milky Way GCs

In Figure 2.11 we show the color and magnitude distributions of the different GC subpopulations in our Galaxy. The Milky Way "Young Halo" (YH) GCs, which were suggested to have been accreted from dwarf galaxies (e.g. Zinn 1993; Mackey & Gilmore 2004; Mackey & van den Bergh 2005; Lee et al. 2007) show a turnover magnitude ($M_{TO} = -7.27 \pm 0.11$ mag) which, although fainter, is consistent within the uncertainties with that of our bGCs ($M_{TO} = -7.41 \pm 0.22$ mag). In comparison with the Magellanic Clouds (see also Sect. 2.3.1), the magnitude distribution of the LMC old GCs peaks at surprisingly bright magnitude $M_{TO} = -7.78 \pm 0.12$. When

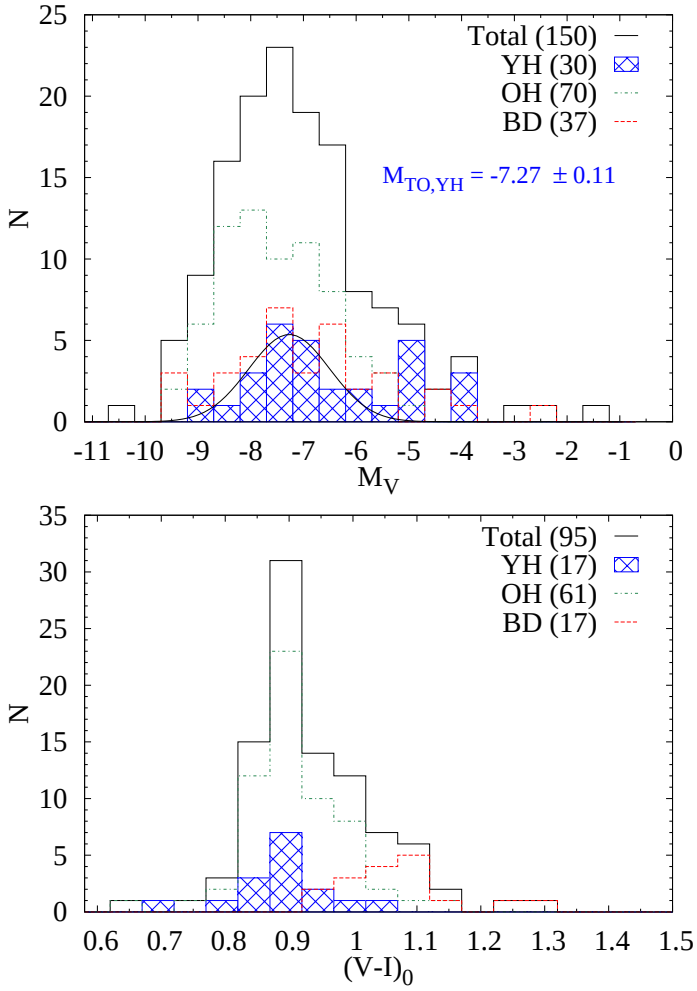

Figure 2.11: Color and magnitude distributions of Galactic GCs (data from Harris 1996, revised 2003). Based on their metallicity and horizontal branch morphology, Bulge/Disk (BD), Old Halo (OH) and "Young" Halo (YH) GCs are shown in red, green and blue, respectively. Excluding the last two bins, a Gaussian fit to the YH GC histogram gives a $M_{TO,YH}$ value that is fainter than those of our dIrrs' GCs and the LMC GCs (see Fig. 2.9).

including the old GCs of the SMC and the Fornax dSph the combined peak magnitude becomes slightly fainter ($M_{TO} = -7.67 \pm 0.1$ mag). K-S tests (cf. Table 2.1) assign 54% and 50% similarity for the $V-I$ and M_V distributions, respectively, between our bGCs and the Galactic YH clusters. It should be noted, that only 17 YH GCs have $V-I$ colors in the Harris (1996) catalog. Comparing with the same distributions for the OH GCs gives probabilities of 2% and 19%. The luminosity function of the old LMC clusters is similar to the YH and OH clusters with K-S probability of 43% and 78%, respectively. In Table 4 are also shown the results from K-S tests between the $V-I$ and M_V distributions for ten of the old GCs in the LMC with V-I colors (McLaughlin & van der Marel 2005) and bGC in our dIrrs sample.

Table 2.1: Results of K-S tests for $V-I$, M_V, r_h and ϵ between our bGCs and the old GCs in the LMC and our Galaxy.

	bGCs				LMC			
	$V-I$	M_V	r_h	ϵ	$V-I$	M_V	r_h	ϵ
YH	54%	50%	1%	1%	25%	34%	32%	3%
OH	1%	19%	86%	3%	1%	78%	7%	20%
LMC	73%	66%	8%	99%	–	–	–	–

2.3.3 Structural parameters

Half-light radii

The half-light radius r_h, a measure of the GC size and stable over many (> 10) relaxations times (e.g. Spitzer & Thuan 1972; Aarseth & Heggie 1998), is the most robust and easy to measure structural parameter and therefore is a good indicator for the initial conditions of the GC formation. Hence, a comparison between r_h of the blue GCs in our dIrr sample and r_h of the YH GCs in our Galaxy and in the LMC can reveal an important evolutionary link among them as well as information of the initial conditions of GC formation.

The r_h versus M_V relation in Fig. 2.12 a) shows that most of our GC candidates fall below the upper envelope of the GC distribution in our Galaxy (solid line in Fig. 2.12; see Mackey & van den Bergh 2005). Interestingly, the brightest cluster, IC1959-04, is at the very center of its host galaxy and occupies the same r_h versus M_V region and has similar color as ω Cen, which supports a scenario for ω Cen's origin as the nucleus of a former dwarf galaxy (e.g. Hilker & Richtler 2000; Hughes & Wallerstein 2000). However, this is the only nuclear cluster we find in the studied galaxies. It is known that r_h increases with galactocentric distance for MW, M 31 and Cen A GCs (e.g. Barmby et al. 2007), which indicates the influence of the galactic potential. In Fig. 2.12 b) we combined the GCs r_hs from all galaxies in our sample. Note that in Fig. 2.12 b we define $r_\mathrm{eff} = \sqrt{a \times b}$, where a and b are the galaxy semi-major and semi-minor axes of the galaxy light profile. A dependence of r_h on the projected distance from the galaxy center can not be confirmed with significance given the large scatter and the low number statistics.

In Figure 2.13 we show the size distribution of the GCs in our sample compared with that of the old GCs in the Magellanic Clouds and GCs in our Galaxy. Our bGCs are more compact on average ($\bar{r}_\mathrm{h} \sim$3.3 pc, cf. Fig. 2.13) than the LMC GCs ($\bar{r}_\mathrm{h} \sim 6$ pc) and the YH GCs ($\bar{r}_\mathrm{h} \sim 7.7$ pc). They are rather more similar to the MW OH GCs ($\bar{r}_\mathrm{h} \sim$3.5 pc), as evidenced by the K-S test probabilities listed in Table 2.1. In Sect. 2.4.2 we discuss the implication of this comparison.

It is worth noting, that in the SMC, a dIrr galaxy which closely resembles in total luminosity ($M_{V,SMC} = -16.82$ mag) the galaxies in the current study, there exists only one old GC (10.6 Gyr, Dolphin et al. 2001) with $r_\mathrm{h} \simeq 5.6$ pc.

Probability K-S tests give 1% and 8% likelihood that the bGC have a similar r_h distribution as the YHs or the old LMC GCs, respectively. The r_h distribution of LMC GCs is 32% and 7% similar to the ones of YHs and OHs, respectively (see Table 2.1).

GCs more extended than those of the Milky Way and elliptical galaxies have been

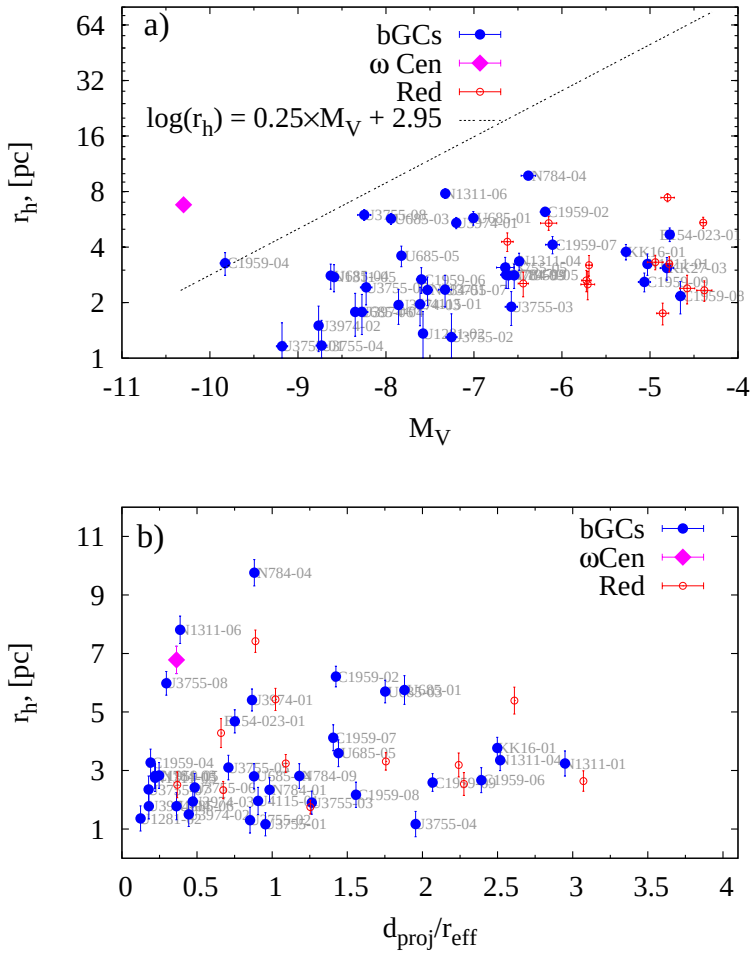

Figure 2.12: a) Distribution of the GC candidate sizes ($r_{\rm h}$) with their absolute magnitude. b) $r_{\rm h}$ as function of the normalized projected distance ($d_{\rm proj}/r_{\rm eff}$) from the host galaxy center (b). The GC candidates occupy the M_V vs. $r_{\rm h}$ plane below the relation defined by Mackey & van den Bergh (2005) (thick line in panel a), which is typical for GCs in our Galaxy and other galaxies. IC 1959-04, the nuclear cluster of IC 1959, shares the same parameter space as ω Cen.

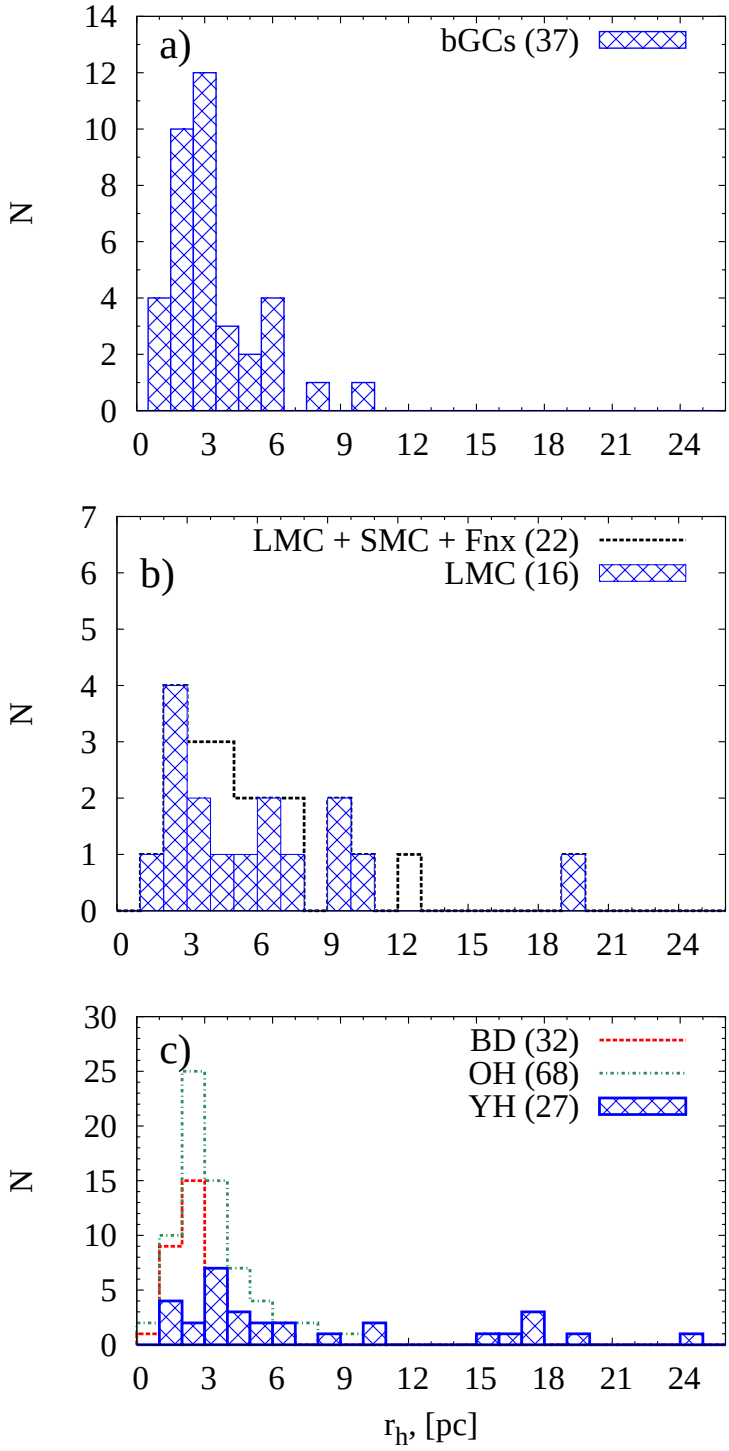

Figure 2.13: Comparison of $r_{\rm h}$ distributions for (a) GCs in our dIrrs with that of (b) LMC (+SMC+Fornax) GCs and (c) MW GCs (data from Mackey & van den Bergh 2005; McLaughlin & van der Marel 2005).

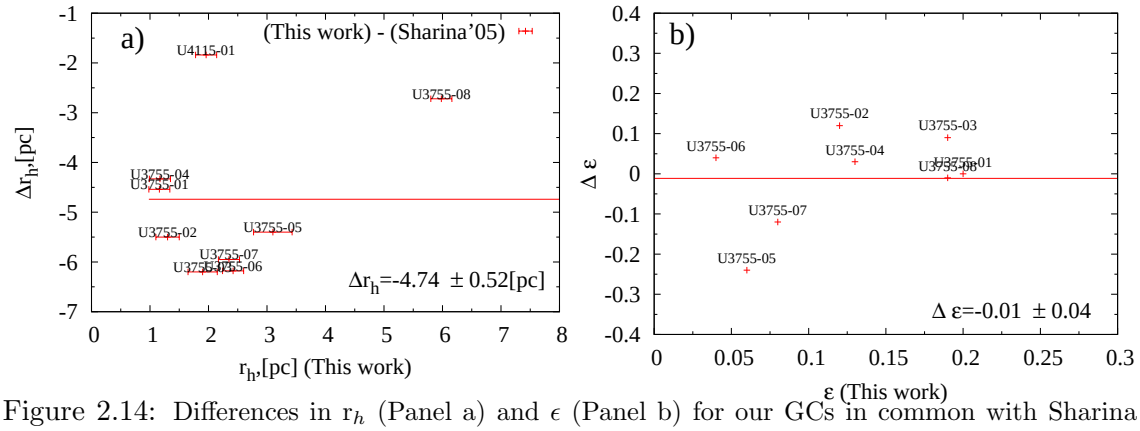

Figure 2.14: Differences in r_h (Panel a) and ϵ (Panel b) for our GCs in common with Sharina et al. (2005). The least-square fit to the data (solid line) shows that our sizes are ~ 5 pc smaller than found in the earlier study, while the expected difference due to a different distance modulus is only -0.55 pc.

previously observed in other dIrrs (Seth et al. 2004; Sharina et al. 2005). We have nine GCs in common (one in UGC 4115 and eight in UGC 3755) with the Sharina et al. (2005) study. Our $r_{\rm h}$ measurements, which take into account the cluster ellipticity, are significantly smaller by ~ 5 pc (see Fig. 2.14). The expected difference due to updated distances to UGC 3755 (m–M= 29.35, Tully et al. 2006) between both studies is just -0.53 pc (m–M= 28.59, Karachentsev et al. 2004, adopted by Sharina et al. (2005)).

However, the absolute $r_{\rm h}$ comparisons between GCs should be taken with caution as they were assessed using different measurement methods by different studies. The structural parameters of the Galactic and LMC GCs are based on King model fits from McLaughlin & van der Marel (2005). The same King model was used in our study, but using discrete concentration parameters as provided by ISHAPE, while McLaughlin & van der Marel (2005) derived a concentration parameter coming from their best χ^2 fit to the model.

Ellipticities

Two major dynamical effects are considered as drivers of the evolution of the GC ellipticities (ϵ): *i)* the external galactic tidal field and/or *ii)* internal (age-dependent) rotation and/or velocity anisotropy (e.g. Fall & Frenk 1985; Han & Ryden 1994; Meylan & Heggie 1997). A third possibility, although perhaps less attractive than general mechanisms, is that highly flattened GCs might arise from cluster mergers (e.g. de Oliveira et al. 2000). Fall & Frenk (1985) showed that the cluster ϵ decreases by a factor $\sim 2-5 \times t_{rh}$. The relaxation time depends on the clusters mass at $r = r_{\rm h}$. For Galactic GCs it ranges from $\sim 10^8$ to $\sim 10^{10}$ yr (Djorgovski 1993) and $\sim 10^8 - \sim 10^9$ yr for LMC GCs (Fall & Frenk 1985). It is well known, that on average the Magellanic Clouds GCs are flatter than those in the Milky Way and M31 (e.g. Geisler & Hodge 1980) and these differences might be primarily due to differences in cluster ages (Han & Ryden 1994).

The ellipticities of the clusters in our sample are measured at the $r_{\rm h}$ along the semi-major axis returned by ISHAPE. In Figure 2.15 we present the ellipticities of the bGCs in our dIrr galaxies versus $M_V, d_{\rm proj}/r_{\rm eff}, (V-I)_0$ and $r_{\rm h}$ in panels a,b,c and

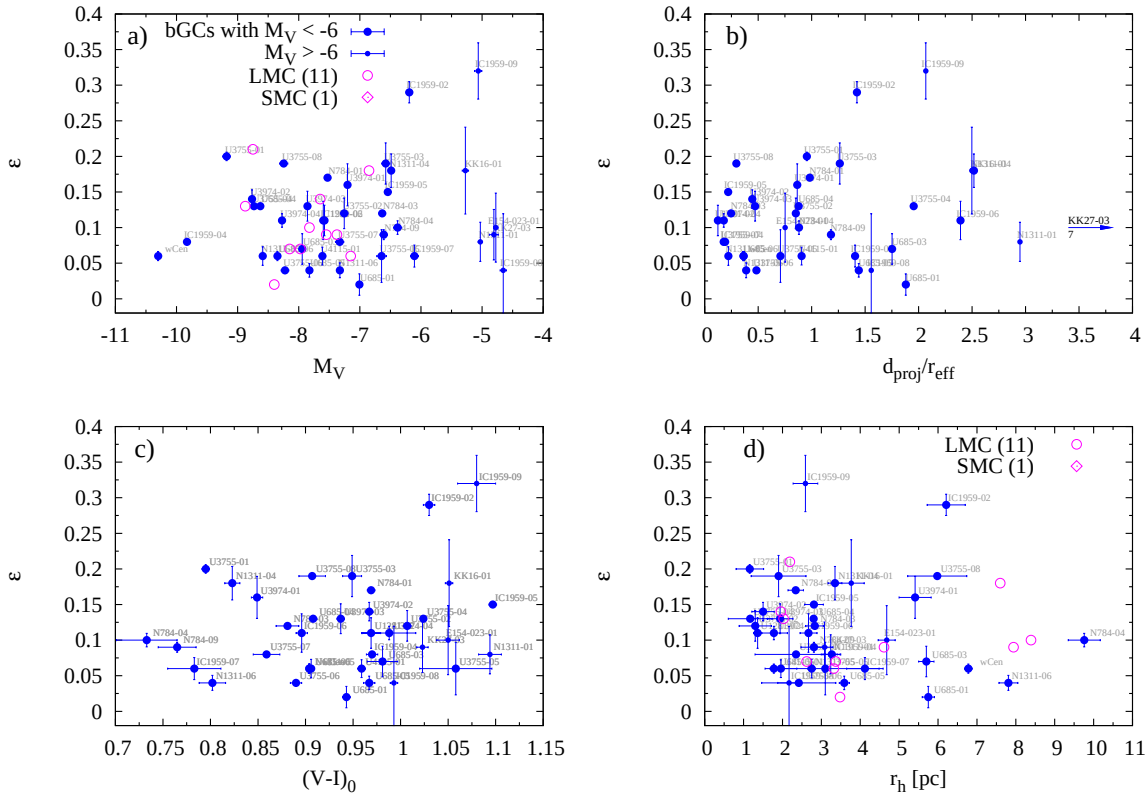

Figure 2.15: Correlation of clusters ellipticities with M_V, $d_{\rm proj}/r_{\rm eff}$, $(V-I)_0$ and $r_{\rm h}$ in panels a, b, c and d, respectively. Old GCs in the LMC and SMC are shown with open circles and diamonds, respectively (data from Frenk & Fall 1982; Kontizas et al. 1989, 1990).

d, respectively. For comparison we show the old GCs in the Magellanic Clouds with data available from the literature (Frenk & Fall 1982; Kontizas et al. 1989, 1990). In general, the old LMC/SMC GCs overlap well with the clusters in our sample. As previous studies for various galaxy types also showed, no correlation between ϵ and the projected distance from the galactic center can be seen (Fig. 2.15 b).

The comparison between the ellipticity vs. M_V, $(V-I)_0$ and $r_{\rm h}$ distributions the bGCs in this study with those of YH GCs in our Galaxy (suspected of being accreted from dwarf galaxies), is shown in Figure 2.16. For the Galactic clusters, we used the ϵ entries in the 2003 update of the Harris (1996) catalog. Although only 16 YH GCs are included, it is seen that they overlap with the old Magellanic GCs in the ϵ vs. M_V and $r_{\rm h}$ planes (Fig. 2.16 a, c). However, the ϵ distributions (Fig. 2.17) of our bGCs and the LMC GCs are very similar to one another ($\bar{\epsilon} \simeq 0.12 \pm 0.07$ and $\bar{\epsilon} \simeq 0.11 \pm 0.06$) and flatter than that of the YH GCs ($\bar{\epsilon} \simeq 0.06 \pm 0.06$), and show a peaked, Gaussian-type distribution. The result of a Kolmogorov–Smirnov test (see Table 2.1) run on the ϵ distributions of the YH GCs, LMC old GCs and the bGCs in our sample showed that there is only 1 and 3% chance that the LMC old GCs or bGCs, respectively, are drawn from the same distribution as the YH GCs, while the bGCs and the LMC GCs share the same distribution at a 99% confidence level. The presence of such a turnover might mean that either the clusters are not fully relaxed, i.e. they are dynamically young and still evolving, or it is an indication of the impact of the weaker potential of these dwarfs on the initial conditions during

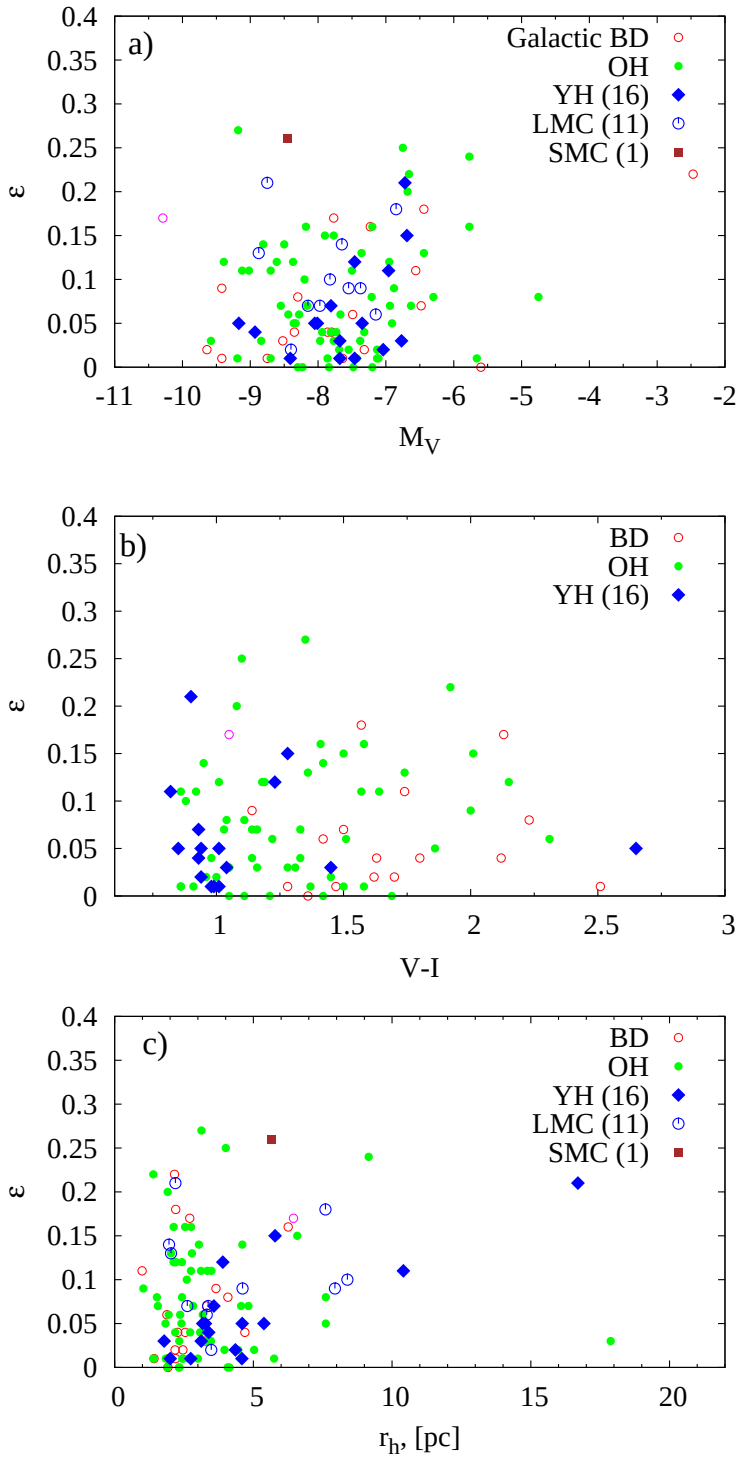

Figure 2.16: Galactic and Magellanic Clouds GC ellipticities versus their a) M_V, b) $(V-I)_0$ and c) r_h. Different symbols show the different MW and LMC/SMC GC populations. Data from the 2003 update of the Harris (1996) MW GC catalog and from Frenk & Fall (1982); Kontizas et al. (1989, 1990) for LMC and SMC.

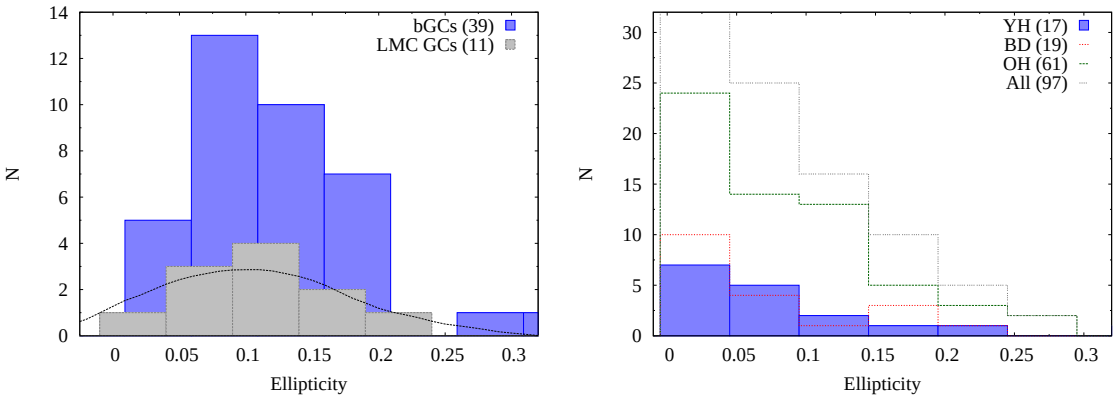

Figure 2.17: Distributions of ellipticities for bGCs in our sample and old GCs in the LMC (upper panel) (Frenk & Fall 1982; Kontizas et al. 1989) and in our Galaxy (lower panel, data from the 2003 update of the Harris 1996, catalog).

the GC formation, or both.

Therefore, if the YH GCs are of external origin, their ϵ distribution should be similar to that of the bGCs. In contrast, it is more like a power law as seen in the Fig. 2.17, right panel. This might be an indication that their accretion must have happened very early and the strong tidal field of our Galaxy might be responsible for the evolution of the ϵ distribution away from the initial conditions, removing the turnover. Note, however, that reliable ellipticities are available only for approximately half of all MW YH GCs (16 out of 30) and for old GCs in the LMC (11 out of 17). Thus the ellipticity distribution we show might be biased.

2.3.4 Specific frequencies

The 'specific frequency' (S_N) is a quantity introduced by Harris & van den Bergh (1981) to compare the richness of GCSs between (elliptical) galaxies. The S_N was originally defined as twice the number of GCs down to the turnover peak of the GC luminosity function, or (as most commonly used) as the total number of GCs ($N_{\rm GC}$), normalized to a galaxy luminosity of $M_V = -15$ mag:

$$S_N = N_{\rm GC} 10^{0.4(M_V+15)} \tag{2.2}$$

For poor GCSs containing few GCs, such as those in our dIrrs, calculating the S_N as originally defined is practically impossible. Hence, the S_N values presented here were derived from the total $N_{\rm GC}$. Given the small physical sizes of the studied dIrrs and the large enough ACS field of view, there is no need to apply a geometrical completeness correction to the total GC number for most of the galaxies except for the brightest and largest two, NGC 784 and ESO 154-023. Because of the extremely deep ACS observations, corrections due to photometric incompleteness are not necessary either (see Sect. 2.2.7). In order to derive the total galaxy light we used the IRAF/STSDAS task ELLIPSE. The galaxy magnitudes we derived (see Table 2.2) were identical (within the errors) to the RC3 (de Vaucouleurs et al. 1991) values for the same galaxies at the radius of the $\mu_B = 25$ mag arcsec^{-2} isophote. However, we could not directly measure the total magnitudes for NGC 784 and ESO 154-023 which extend beyond the ACS field and thus we adopted their RC3 magnitudes.

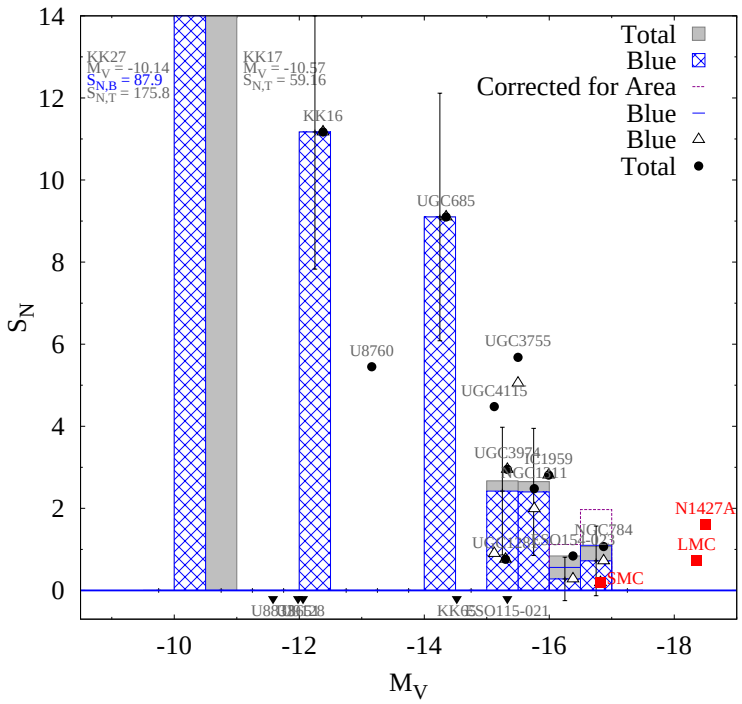

Figure 2.18: S_N versus host galaxy M_V. Open triangles and filled circles are the S_N values for our sample dIrrs including only the blue GCs and blue and red GCs for each individual galaxy, respectively. Galaxies in which no GC candidates were found are shown with filled triangles and negative S_N. With the hatched histogram we show the average S_N distribution per galaxy magnitude bin with width equal to the width of the histogram bin. For comparison with filled squares are shown the S_N values for the Magellanic Clouds and NGC 1427A in the Fornax galaxy cluster.

The majority of the bGCs in our ACS images are resolved and the estimated background contamination for this GC sub-population is low (see Sect. 2.2.7). Thus, the uncertainty of the S_N values for the bGCs presented in Table 2.3 is mainly due to stochasticity in the number of genuine GCs rather than background contamination. The subpopulation of red GCs is more likely affected by faint and unresolved background sources, because red GCs are on average fainter and more compact than bGCs. This is the reason why our analysis is mainly focused on bGCs.

Present-day S_N Values

Using the distance modulus for each galaxy as determined by Tully et al. (2006) the apparent galaxy magnitudes were converted to absolute ones. Taking the numbers of GCs as given in Table 2.3, the resulting S_N values then range from 0.74 to 88. Excluding the extreme outlier (KK 27) with $S_N = 88$, the mean value for all galaxies with blue GCs is ~ 3.8. The total mean S_N would increase to ~ 4.2 if one would include the red GCs. Figure 2.18 shows the S_N values for each individual galaxy (symbols) and an average S_N for galaxies in magnitude bins (histogram). The galaxies in which no GC was detected are plotted with negative S_N values. The S_N values of the Magellanic Clouds and NGC 1427A are shown for comparison. To calculate the Magellanic Clouds' absolute magnitudes we used the distance moduli of Laney & Stobie (1994) and information for NGC 1427A was taken from Georgiev

et al. (2006). Note that the dIrrs in our sample with luminosities similar to the SMC also have similar S_N values. In general we find that the GC specific frequency in dIrrs increases (on average) with decreasing host galaxy luminosity. This result was also found for early-type dwarfs in galaxy clusters (Miller et al. 1998; Forbes 2005; Strader et al. 2006; Miller & Lotz 2007).

S_N Values After Evolutionary Fading

Since the dIrr galaxies in our sample are of Magellanic type with ongoing star formation, their present-day integrated luminosity is dominated by the young stellar populations that formed in the most recent star formation episode. In order to make a more relevant comparison with the S_N values in evolved dwarf galaxies like dEs or dSphs, we have to account for fading of the dIrrs' luminosity due to stellar evolution. All galaxies in our sample have luminosities comparable to or even fainter than the SMC. We therefore adopted the SMC metallicity of [Fe/H]$= -0.68$ (Luck et al. 1998) for the passive evolution of the stellar population. Bruzual & Charlot (2003) SSP models were used to derive the stellar age for each galaxy based on their color and adopted metallicity. The mean stellar age for all galaxies as inferred by their $V-I$ colors is 1.3 Gyr, with individual ages ranging from 0.4 to 3.7 Gyr. Given the low surface brightness and low star formation of these dwarfs, a passive (dissipationless) evolution was assumed to evolve the galaxies' luminosity to an age of 14 Gyr. This resulted in an average luminosity fading of 2.34 ± 0.43 mag, with a full range from 2.98 to 1.09 mag. This leads to an increase in the S_N values by a factor of 2 to almost 16 due to passive evolutionary fading. The specific frequencies after age fading (S_{Nf}) are listed in Table 2.3.

It is worth assessing the impact of the adopted SMC metallicity on the evolved S_N values. Due to the continuous star formation rate, typical for late-type galaxies, a dIrr galaxy in our sample cannot be more metal-poor than its most metal-poor GC(s); unless, in the unlikely scenario where the galaxy underwent instantaneous star formation which ceased abruptly prior to GC formation. However, assuming a mean galaxy metallicity as metal-poor as $0.02 \times Z_{\odot}$, the mean stellar age, as inferred from the measured $V-I$ color, increases by ~ 1 Gyr. Hence, after evolutionary age fading the galaxy will appear, on average, ~ 1 mag fainter. This translates into an increase of S_N up to 6 times of the present-day value, unlike up to 16 times if the dIrrs were of SMC metallicity. In general, the change of S_N values due to evolutionary age fading will be milder for more metal-poor galaxies, and the evolved S_N values in Table 2.3 will apply only to galaxies with SMC metallicity ([Fe/H] $= -0.68$, i.e. similar to $0.2 \times Z_{\odot}$ in the Bruzual & Charlot (2003) SSPs). This illustrates the dependence of S_N values on host galaxy metallicity.

If one would add all galaxies with GCs together, a master galaxy of $M_V = -18.24$ mag would result with a $S_{Nb} = 1.9$. Including also dIrrs without GCs results in a master galaxy of $M_V = -18.36$ mag and $S_{Nb} = 1.7$. Fading the master galaxy light to an age of 14 Gyr gives for the two cases $M_V = -16.0$ and $M_V = -16.11$ mag and specific frequencies of $S_N = 14.8$ and $S_N = 13$, respectively. Again, this is consistent with S_N values for dEs/dSphs of similar absolute magnitude.

2.4 Discussion and conclusions

We have searched for old globular clusters in 19 Magellanic-type dwarf Irregular (dIrr) galaxies utilizing archival $F606W$ and $F814W$ HST/ACS images. The main goal of this study is to assess the properties of the old GCs in such systems and compare them with those of the Galactic "Young Halo" GCs (YH GCs), which are considered to be of external origin (e.g. Zinn 1993; Mackey & van den Bergh 2005; Lee et al. 2007). The studied dIrrs reside in nearby (2 - 8 Mpc) groups and associations containing dwarf galaxies only, with no massive nearby galaxy around (Tully et al. 2006). All galaxies in our sample have absolute magnitudes smaller than or equal to the SMC.

2.4.1 An Apparent Lack of Low-Luminosity GCs

We detect in total 50 GCs in 13 dIrrs, of which 37 have $(V-I)$ colors consistent with "blue" (old and metal-poor) GCs (bGC) typical for low-mass dwarfs and the bGC population in other galaxies. The few red GCs (rGC) we detect are indistinguishable in sizes from the bGCs and are not expected in this galaxy type, perhaps they are background contaminants. Only follow-up spectroscopy can reveal their nature. The luminosity function (LF) of the bGC candidates in our sample shows a turnover magnitude at $M_V = -7.41 \pm 0.22$ mag, similar to what is typically found in other galaxy types, and a GCLF width of $\sigma = 1.79 \pm 0.31$, typical for dIrrs but slightly broader than the typical width of GCLFs in massive galaxies. The broadening of the GCLF might be (at least partly) due to the distance modulus uncertainties to those dwarfs of $\sigma(m-M) \simeq 0.05$ (Tully et al. 2006).

Interestingly, we do not find many low-luminosity GCs, contrary to expectations. As we showed, this is not due to incompleteness or selection criteria (Sect. 2.3.1). The lack of faint GCs might be related to environmental effects and the physical conditions of the GC formation and disruption in such dwarfs. However, all dIrrs in our sample are found in associations of dwarf galaxies, e.g. there is no dominant massive galaxy in their immediate vicinity. Thus tidal stripping or disruption in the current environment is unlikely to be responsible.

Another possibility could be that the bluer ($0.8 \sim V-I$) and slightly brighter ($M_V \sim -6.5$ mag) GCs seen in Fig. 2.7 might actually be relatively young GCs. Aging due to stellar evolution would make their magnitudes fainter and colors redder. If so, a shift in their colors and magnitudes of $(V-I) \sim 0.15$ and $M_V \sim 1.5$ mag would be required to populate that region in the CMD. According to the Bruzual & Charlot (2003) SSP models, this is exactly the amount of color and magnitude evolution needed for a $\gtrsim 4$ Gyr old metal-poor cluster with $(V-I) \gtrsim 0.8$, to evolve to ~ 14 Gyr.

Further detailed spectral analysis of GC candidates in dIrrs are necessary to address this question and draw firmer conclusions. Although an interesting observational result, for now we can not extend the discussion further given the inadequate number statistics in our data set.

2.4.2 Sizes: GCs in dIrr Galaxies are smaller than "Young Halo" GCs

The half-light radii, $r_{\rm h}$, of the bGCs in our sample are smaller on average, $r_{\rm h} \sim 3.3\,{\rm pc}$, than those of the YH GCs in our Galaxy ($r_{\rm h} \sim 7.7\,{\rm pc}$) and those in the Magellanic Clouds and Fornax dwarfs ($r_{\rm h} \sim 6.3\,{\rm pc}$) and other dIrrs (Sharina et al. 2005; van den Bergh 2006). They compare well with the $r_{\rm h}$ values of Galactic OH GCs, as shown by the K-S tests in Table 2.1. This suggests that either the conditions of YH GC formation were different from those in low-mass galaxies, or their sizes were influenced by tidal shocks in their subsequent evolution in the Galactic tidal field which will require that they have been accreted very early. $N-$body simulations (e.g. Dinescu et al. 1999; Gieles et al. 2007) show that the effect of bulge/disk shocks scales with $r_{\rm h}^3/M_{\rm cl}$. Hence, depending on their orbital periods and pericentric radii, the tidal field will strongly affect diffuse clusters, such as the YH GCs, and transform their $r_{\rm h}$ distributions. Further, Lamers et al. (2005) show that the cluster disruption time scales with the ambient density. As $r_{\rm h}$ is stable over many relaxation times (Sect. 3.7) in the absence of a tidal field, a modeling of the $r_{\rm h}$ evolution with the strength of the host galaxy tidal field and environmental density will be required to understand the $r_{\rm h}$ evolution.

2.4.3 The Ellipticity Distribution of GCs in dIrr Galaxies

We find that, on average, the ellipticities (ϵ) for the GCs in the studied dIrrs are practically the same as those of the old GCs in the Magellanic Clouds ($\bar{\epsilon} \simeq 0.12 \pm 0.07$ and $\bar{\epsilon} \simeq 0.11 \pm 0.06$, respectively). They also show similar distributions of ϵ with M_V, $r_{\rm h}$ and cluster color (Fig. 2.15). Although ellipticities are only available for half the Galactic YH GCs, their distribution differs significantly from those of GCs in our sample and those in the LMC (see Fig. 2.17). This is further shown by the result of the K-S tests presented in Table 2.1. This shows that *if* the YH GCs formed in similar environments as the GCs in low-mass dIrr galaxies, their ellipticity must have been significantly altered by the tidal field of the Galaxy after their accretion. I.e., if YH GCs were accreted from satellite galaxies, the accretion event(s) must have happened quite early.

The observed turnover in the ellipticity distributions for the bGCs and LMC old GCs in contrast with the power-law ϵ distribution for the Galactic YHs, might suggest that the former are slightly younger and not yet fully relaxed (see also Sect. 2.3.3), as expected from theory (Fall & Frenk 1985).

Furthermore, the strength of the galactic tidal field is expected to be important in setting the initial conditions during the GC formation. It probably also causes the mean ϵ value to vary with galaxy mass, as slightly higher ϵ values are observed for the young clusters in the SMC than in the LMC (Kontizas et al. 1990). Thus, it does not seem surprising that the GCs in our low-mass dIrrs and in the Magellanic Clouds on average are flatter than those in massive galaxies and that, if the YH GCs were accreted early enough, their evolution in the stronger Galactic tidal field must have influenced their ellipticities. The fact that the ϵ vs. $r_{\rm h}$ relation for the YH GCs holds just as well for GCs in our dIrrs and the LMC/SMC suggests that they might all have formed in similar initial conditions. However, this interpretation needs to be tested with larger numbers of GCs in dIrrs, simulations and further precise determinations of the GC ellipticities in various environments, as well as

future integrated spectra to infer their ages and metallicities.

2.4.4 Specific Frequencies: Trend with galaxy luminosity and Comparison to Dwarf Ellipticals

The present-day specific frequencies (S_N) of the dIrr galaxies in our sample span a broad range from $S_N = 0.3$ to 87. Using the galaxy $V - I$ colors and the SSP models of Bruzual & Charlot (2003) with the metallicity of the SMC, we derive age fading of the galaxies' luminosity to 14 Gyr. We find that this causes an increase in the S_N by a factor of ~ 2 to 16, if all GCs survive and no new ones are formed (see also Table 2.3).

Assuming that these groups of dIrr galaxies might not be fully relaxed yet (Tully et al. 2006) and that their members will merge eventually, we constructed a "master" dIrr galaxy from all members. The resulting present-day and faded S_N values of the "master" dIrr are similar to the values for early-type dwarfs. This supports the idea that some dE/dSphs might have evolved from dIrrs (Miller et al. 1998), due to gas loss after the main burst of star formation (Dekel & Silk 1986) and/or via external ram pressure stripping (Moore et al. 1998; Grebel et al. 2003). The S_N values of the non-faded and faded dIrrs, in general, are consistent with those found for dEs in the same luminosity range (Miller et al. 1998; Miller & Lotz 2007).

The recent discovery of hidden non-axisymmetric disk-like structures and other morphological anomalies in Virgo early-type dwarfs from detailed isophotal analysis (Ferrarese et al. 2006) also suggests that their progenitors might be late-type dwarfs. This view is theoretically supported by Mastropietro et al. (2005). If rapid cessation of star formation processes occurs in present-day dIrrs, the comparison with Bruzual & Charlot (2003) stellar evolution models shows that ~ 10 Gyr of passive fading are required for dIrrs to fade and fall on the dSphs metallicity–luminosity relation (see also Jerjen et al. 2004).

If all dIrrs in our sample are merged together (without dissipation) to a master dIrr galaxy and the galaxy light is evolved to 14 Gyr, the GCS characteristics (Table 2.3) of the "merger remnant" resemble those of a field dwarf elliptical or spheroidal galaxy as suggested by Miller et al. (1998).

2.5 Summary and Outlook

Our study shows that properties of old GCs in low-mass dIrr galaxies hold interesting and important insights in our understanding of what were the conditions at the time of their formation. Indeed, considering their color and magnitude distributions, they are as old and as metal poor as the GCs in other galaxy types. Their structural parameters (r_h and ϵ), whose evolution is shown to depend mainly on processes internal to the GCs (e.g. rotation, two-body relaxation), are very similar to those of the old GCs in the Magellanic Clouds, but differ from YH GCs in our Galaxy. Under the assumption that initial conditions of GC formation (occurring in giant molecular clouds) were similar among old GCs, this difference suggests that the initial structural parameters were altered by an amount depending on the environment, i.e., the strength of the galactic potential plus external pressure. Therefore, our comparison of the bGCs in dIrrs with the Galactic YH GCs, the latter of which are suspected

Table 2.2: General properties of the studied dwarf irregular galaxies. In column (1) are listed the Group ID to which the galaxy belongs and the galaxy's name; columns (2) and (3) list the galaxies' coordinates, columns (4) and (5) their morphological classification; columns (6) and (7) give the distance and distance modulus from Tully et al. (2006), followed by the galaxies' apparent (8) and absolute (9) magnitudes and colors (10) measured in this work (all dereddened from Galactic extinction).

Group/ID	R.A. (J2000.0)	Decl. (J2000.0)	Morph.	Type	D[a] Mpc	$m-M$ mag	V_0 mag	M_V^0 mag	$(V-I)_0$ mag
(1)	(2)	(3)	(4)	(5)	(6)	(7)	(8)	(9)	(10)
14+12									
ANTLIA	10 04 03.9	−27 20 01	10.0	IAB	1.25	25.49	18.39	-7.1	0.80
14+08									
UGC 8760	13 50 50.6	+38 01 09	9.8	IB	3.24	27.55	14.39	-13.16	0.68
UGC 8651	13 39 53.8	+40 44 21	9.9	I	3.02	27.40	15.42	-11.98	0.66
UGC 8833	13 54 48.7	+35 50 15	9.9	IAB	3.20	27.53	15.95	-11.58	0.58
17+06[b]									
NGC 784	02 01 17.0	+28 50 15	7.7	SBdm	5.19	28.58	11.71	-16.87[c]	–
UGC 1281	01 49 31.5	+32 35 17	7.5	Sdm	5.13	28.55	13.25	-15.30	0.83
KK 16	01 55 20.3	+27 57 14	10.0	I	5.47	28.69	16.31	-12.38	0.88
KK 17	02 00 10.2	+28 49 53	10.0	I	4.91	28.45	17.88	-10.57	0.96
UGC 685	01 07 22.4	+16 41 02	9.1	Sm	4.70	28.36	14.01	-14.35	0.82
14-14									
ESO 115-021	02 37 48.1	−61 20 18	7.6	SBd	4.99	28.49	13.16	-15.33	0.72
KK 27	03 21 02.4	−66 19 09	10.0	I	4.15	28.09	17.95	-10.14	0.78
14+14									
ESO 154-023	02 56 51.2	−54 34 23	8.8	SBm	5.76	28.80	12.42	-16.38[c]	0.680[c]
IC 1959	03 33 09.0	−50 24 42	8.6	SBm	6.06	28.91	12.92	-15.99	0.74
NGC 1311	03 20 06.7	−52 11 13	8.8	SBm	5.45	28.68	12.92	-15.76	0.78
14+19									
UGC 3974	07 41 52.0	+16 47 54	9.8	IBm	8.04	29.53	14.20	-15.33	0.98
UGC 4115	07 57 02.4	+14 23 01	9.9	I	7.72	29.44	14.32	-15.12	0.74
KK 65	07 42 32.0	+16 33 39	10.0	I	7.72	29.52	15.00	-14.52	0.76
UGC 3755	07 13 51.6	+10 31 19	9.9	IAB	7.41	29.35	13.85	-15.50	0.88
Dregs									
UGC 9128	14 15 56.5	+23 03 19	9.9	IAB	2.24	26.75	14.69	-12.06	0.60

[a]Tully et al. (2006) [b]Information for UGC 9240, which belongs to this group, was taken from Sharina et al. (2005) [c]From RC3

to have their origin in accreted low-mass galaxies, may indicate that the Galactic YH GCs were accreted very early. This accretion must have been early enough for the Galactic tidal field to have an impact on the time scale of the evolution of the structural parameters.

However, to properly assess all the addressed suggestions to a higher statistical confidence, we suggest that further detailed studies of GC properties in other samples of low-mass dIrr galaxies be undertaken in the near future.

Table 2.3: Specific frequencies. In column (1) are listed the Group ID to which the galaxy belongs and the galaxy's name; The following columns are: the distance (2), absolute magnitude (3), number of blue GCs (4), number of red GCCs (5), blue GCs and total specific frequency $S_{Nb}(S_{Ntot})$ (6), age of the dominant stellar population deduced from the Bruzual & Charlot (2003) SSP ($0.2 \times Z_{\odot}$) using the galaxy color (7), amount of $V-$band fading to 14 Gyr (8), $M_{V,f}$ after fading (9), S_N^f after fading (10), M_V of the product galaxy after merging all group members together (11), S_N of the merger product, amount of the merger product fading to 14 Gyr (12), $M_{V\,\mathrm{grp},f}$ after merger fading (13), S_N^f after merger fading (14). Numbers in brackets always refer to the total values.

Group/ID	D[a] Mpc	M_V^0 mag	N_b	N_r	$S_{N\mathrm{b(tot)}}$	Age Gyr	Fade Δ mag	$M_{V,f}^0$ mag	$S_{N\mathrm{b(tot)}}^f$	$M_{V\,grp}^0$ mag	$S_{N\mathrm{b(tot)}}$	Fade Δ mag	$M_{V\,\mathrm{grp},f}^0$ mag	$S_{N\mathrm{b(tot)}}^f$
(1)	(2)	(3)	(4)	(5)	(6)	(7)	(8)	(9)	(10)	(11)	(12)	(13)	(14)	(15)
14+12										–	–	–	–	–
ANTLIA	1.25	-7.1	0	0	0 (0)	1.2	2.36	-4.74	0 (0)					
14+08										-14.82	0 (0)	2.72	-12.1	0 (0)
UGC 8760	3.24	-13.16	0	1	0 (5.45)	0.8	2.57	-10.59	0 (58)					
UGC 8651	3.02	-11.98	0	0	0 (0)	0.7	2.62	-9.36	0 (0)					
UGC 8833	3.20	-11.58	0	0	0 (0)	0.4	2.98	-8.60	0 (0)					
17+06[b]										-17.20	1.45 (1.85)	2.18	-15.02	10.78 (13.72)
NGC 784	5.19	-16.87[c]	4	2	0.72 (1.07)	1.0	2.36	-14.51	6.3 (9.4)					
UGC 1281	5.13	-15.30	1	0	0.76 (0.76)	1.9	2.37	-12.93	6.7 (6.7)					
KK 16	5.47	-12.38	1	0	11.2 (11.2)	1.2	2.42	-9.96	104 (104)					
KK 17	4.91	-10.57	0	1	0 (59.2)	2.9	1.39	-9.18	0 (213)					
UGC 685	4.70	-14.35	5	0	9.10 (9.10)	1.9	2.37	-11.98	81 (81)					
14-14										–	–	–	–	–
ESO 115-021	4.99	-15.33	0	0	0 (0)	1.1	2.33	-13.0	0 (0)					
KK 27	4.15	-10.14	1	1	88 (176)	1.2	2.35	-7.79	766 (1531)					
14+14										-17.27	1.49 (1.86)	2.41	-14.86	13.69 (17.11)
ESO 154-023	5.76	-16.38[c]	1	2	0.28 (0.84)	0.8	2.55	-13.83	2.9 (8.8)					
IC 1959	6.06	-15.99	7	0	2.81 (2.81)	1.1	2.33	-13.66	24.1 (24.1)					
NGC 1311	5.45	-15.76	4	1	1.99 (2.48)	1.2	2.35	-13.41	17.3 (21.6)					
14+19										-16.68	2.8 (3.8)	2.05	-14.63	18.29 (25.31)
UGC 3974	8.04	-15.33	4	0	2.95 (2.95)	3.7	1.09	-14.24	8.1 (8.1)					
UGC 4115	7.72	-15.12	1	4	0.9 (4.48)	1.1	2.33	-12.79	7.7 (38.3)					
KK 65	7.72	-14.52	0	0	0 (0)	1.2	2.34	-12.18	0 (0)					
UGC 3755	7.41	-15.50	8	1	5.05 (5.68)	1.3	2.43	-13.07	47.3 (53.3)					
Dregs										–	–	–	–	
UGC 9128	2.24	-12.06	0	0	0 (0)	0.5	2.85	-9.21	0 (0)					

[a] Tully et al. (2006) [b] Information for UGC 9240, which belongs to this group, was taken from Sharina et al. (2005) [c] From RC3

Table 2.4: General properties of the GC candidates in the studied dIrrs. According to the colors of the GC candidates, they are separated with lines on blue, red and likely background contamination sub-populations.

ID	X , Y (pix)	RA DEC (2000) (hh:mm:ss)	M_V^0 (mag)	$(V-I)_0$ (mag)	r_h (pix)	r_h (pc)	ϵ	d_{proj} (kpc)
E154-023-01	3472.05 , 2329.00	02:56:49.17 -54:33:16.51	-4.78 ± 0.04	1.05 ± 0.01	2.02 ± 0.09	4.68 ± 0.15	0.10	1.99
IC1959-02	3083.73 , 1739.38	03:33:14.24 -50:25:40.16	-6.19 ± 0.05	1.03 ± 0.01	4.23 ± 0.01	6.21 ± 0.11	0.29	1.71
IC1959-04	2224.47 , 2273.96	03:33:12.43 -50:24:52.60	-9.83 ± 0.05	0.97 ± 0.01	2.11 ± 0.00	3.27 ± 0.10	0.08	0.23
IC1959-05	1982.16 , 2506.51	03:33:11.51 -50:24:38.34	-6.54 ± 0.05	1.10 ± 0.01	1.81 ± 0.00	2.81 ± 0.10	0.15	0.26
IC1959-06	544.56 , 3554.56	03:33:07.70 -50:23:17.16	-7.60 ± 0.05	0.90 ± 0.01	1.72 ± 0.02	2.67 ± 0.12	0.11	2.87
IC1959-07	2852.76 , 1501.31	03:33:15.71 -50:25:31.32	-6.11 ± 0.06	0.78 ± 0.03	2.66 ± 0.05	4.12 ± 0.15	0.06	1.69
IC1959-08	3366.00 , 2605.55	03:33:09.50 -50:25:45.00	-4.65 ± 0.05	0.99 ± 0.01	1.40 ± 0.07	2.17 ± 0.17	0.04	1.87
IC1959-09	2884.04 , 3886.73	03:33:03.47 -50:25:08.15	-5.06 ± 0.06	1.08 ± 0.02	1.67 ± 0.05	2.59 ± 0.15	0.32	2.48
KK16-01	2158.83 , 2265.25	01:55:23.51 27:57:29.12	-5.27 ± 0.05	1.05 ± 0.01	2.40 ± 0.12	3.77 ± 0.21	0.18	1.20
KK27-03	3744.75 , 3274.22	03:20:50.39 -66:19:38.16	-4.81 ± 0.07	1.02 ± 0.01	1.96 ± 0.05	3.08 ± 0.11	0.09	1.57
N1311-01	493.31 , 415.26	03:20:20.05 -52:10:14.95	-5.03 ± 0.04	1.09 ± 0.01	2.06 ± 0.06	3.24 ± 0.11	0.08	3.57
N1311-04	325.69 , 3554.20	03:20:04.00 -52:09:21.26	-6.49 ± 0.03	0.82 ± 0.01	3.63 ± 0.07	3.35 ± 0.11	0.18	3.05
N1311-05	2219.00 , 2235.00	03:20:07.86 -52:11:11.03	-8.59 ± 0.03	0.91 ± 0.01	2.98 ± 0.01	2.75 ± 0.06	0.06	0.27
N1311-06	1997.27 , 2526.72	03:20:06.69 -52:10:56.18	-7.33 ± 0.04	0.80 ± 0.01	8.47 ± 0.06	7.81 ± 0.11	0.04	0.47
N784-01	358.61 , 1688.27	02:01:18.09 28:48:42.92	-7.53 ± 0.05	0.97 ± 0.01	2.54 ± 0.00	2.34 ± 0.07	0.17	2.35
N784-03	1788.73 , 2006.70	02:01:16.42 28:49:52.81	-6.63 ± 0.06	0.88 ± 0.01	3.07 ± 0.00	2.83 ± 0.07	0.12	0.59
N784-04	3598.94 , 3096.28	02:01:16.57 28:51:38.43	-6.38 ± 0.07	0.73 ± 0.03	10.59 ± 0.05	9.76 ± 0.12	0.10	2.11
N784-09	3802.58 , 3811.71	02:01:18.54 28:52:05.14	-6.61 ± 0.06	0.77 ± 0.02	3.75 ± 0.03	2.81 ± 0.10	0.09	2.82
U1281-02	2147.49 , 2346.95	01:49:32.54 32:35:25.26	-7.58 ± 0.04	0.97 ± 0.01	1.82 ± 0.02	1.36 ± 0.06	0.11	0.17
U3755-01	1638.62 , 2239.86	07:13:51.95 10:31:42.11	-9.18 ± 0.06	0.80 ± 0.01	1.55 ± 0.01	1.16 ± 0.18	0.20	1.30
U3755-02	2864.94 , 2681.61	07:13:50.61 10:30:40.01	-7.26 ± 0.06	1.01 ± 0.01	1.73 ± 0.02	1.30 ± 0.20	0.12	1.16
U3755-03	1497.29 , 2691.75	07:13:50.40 10:31:48.33	-6.58 ± 0.06	0.95 ± 0.01	2.53 ± 0.07	1.90 ± 0.25	0.19	1.72
U3755-04	960.61 , 2756.50	07:13:50.11 10:32:15.02	-8.73 ± 0.06	1.02 ± 0.01	1.56 ± 0.00	1.17 ± 0.18	0.13	2.65
U3755-05	2836.61 , 2038.49	07:13:52.78 10:30:42.62	-6.64 ± 0.08	1.06 ± 0.04	4.14 ± 0.15	3.10 ± 0.33	0.06	0.96
U3755-06	2003.00 , 2200.00	07:13:52.13 10:31:23.97	-8.23 ± 0.06	0.89 ± 0.01	3.11 ± 0.00	2.42 ± 0.18	0.04	0.66
U3755-07	2236.00 , 2229.53	07:13:52.06 10:31:12.28	-7.33 ± 0.07	0.86 ± 0.01	3.02 ± 0.00	2.35 ± 0.18	0.08	0.24
U3755-08	2529.77 , 2427.00	07:13:51.43 10:30:57.23	-8.25 ± 0.07	0.91 ± 0.01	4.53 ± 0.00	5.98 ± 0.18	0.19	0.40
U3974-01	964.54 , 1568.30	07:41:59.49 16:49:00.92	-7.20 ± 0.04	0.85 ± 0.01	4.93 ± 0.05	5.41 ± 0.19	0.16	3.06
U3974-02	1910.55 , 1800.60	07:41:58.16 16:48:16.12	-8.76 ± 0.04	0.97 ± 0.01	1.65 ± 0.01	1.50 ± 0.15	0.14	1.57
U3974-03	2419.29 , 1739.74	07:41:58.08 16:47:50.52	-7.86 ± 0.04	0.94 ± 0.01	2.13 ± 0.02	1.94 ± 0.16	0.13	1.67
U3974-04	2485.60 , 2663.96	07:41:54.87 16:47:54.72	-8.27 ± 0.05	0.99 ± 0.03	1.96 ± 0.01	1.78 ± 0.15	0.11	0.63
U4115-01	1217.34 , 3760.26	07:57:03.79 14:22:41.01	-7.61 ± 0.05	0.96 ± 0.01	2.16 ± 0.02	1.96 ± 0.18	0.06	1.39
U685-01	2866.04 , 2345.56	01:07:26.18 16:40:56.84	-7.01 ± 0.03	0.94 ± 0.01	3.03 ± 0.02	5.75 ± 0.06	0.02	1.31
U685-03	3015.40 , 2596.32	01:07:25.68 16:40:44.19	-7.94 ± 0.04	0.98 ± 0.02	4.34 ± 0.08	5.70 ± 0.11	0.07	1.22
U685-04	2066.37 , 2746.89	01:07:23.60 16:41:21.88	-8.63 ± 0.03	0.91 ± 0.01	2.13 ± 0.00	2.80 ± 0.04	0.13	0.61
U685-05	2993.85 , 2926.33	01:07:24.64 16:40:37.05	-7.82 ± 0.03	0.97 ± 0.01	3.75 ± 0.02	3.59 ± 0.06	0.04	1.01
U685-06	1991.53 , 3155.90	01:07:22.24 16:41:15.14	-8.35 ± 0.03	0.90 ± 0.01	2.01 ± 0.00	1.78 ± 0.04	0.06	0.25
E154-023-02	500.587 , 3732.66	02:57:01.03 -54:35:24.44	-4.78 ± 0.03	1.13 ± 0.01	1.87 ± 0.02	3.85 ± 0.03	0.15	2.89
E154-023-03	750.00 , 3799.00	02:57:01.06 -54:35:11.54	-4.39 ± 0.03	1.28 ± 0.01	2.59 ± 0.05	5.32 ± 0.07	0.09	2.71
KK17-01	1821.97 , 1410.22	02:00:15.85 28:50:42.59	-4.58 ± 0.08	1.22 ± 0.02	2.02 ± 0.03	3.56 ± 0.03	0.03	2.12
KK27-02	2665.38 , 3563.55	03:20:57.69 -66:19:03.74	-6.15 ± 0.08	1.20 ± 0.02	4.55 ± 0.01	6.8 ± 0.01	0.11	0.58
N1311-02	1570.35 , 490.91	03:20:17.96 -52:11:05.37	-5.69 ± 0.03	1.39 ± 0.01	2.13 ± 0.02	4.17 ± 0.02	0.11	2.72
N784-07	1398.57 , 2354.43	02:01:18.31 28:49:44.61	-5.71 ± 0.06	1.22 ± 0.03	3.01 ± 0.08	5.62 ± 0.10	0.09	0.88
N784-08	1020.28 , 3049.7	02:01:21.32 28:49:45.61	-4.38 ± 0.07	1.14 ± 0.04	2.79 ± 0.08	5.2 ± 0.10	0.16	1.61
U3755-09	2247.0 , 2767.67	07:13:50.24 10:31:10.73	-6.62 ± 0.06	1.22 ± 0.01	5.05 ± 0.22	13.44 ± 0.40	0.12	0.90
U4115-02	2306.86 , 890.00	07:56:54.05 14:23:40.30	-5.72 ± 0.05	1.20 ± 0.01	3.09 ± 0.03	8.55 ± 0.06	0.16	4.71
U4115-03	214.30 , 2458.00	07:56:59.20 14:21:53.09	-6.44 ± 0.05	1.23 ± 0.01	3.57 ± 0.01	9.88 ± 0.01	0.14	3.49
U4115-04	3215.00 , 2926.0	07:57:01.16 14:24:22.25	-4.94 ± 0.07	1.26 ± 0.04	2.17 ± 0.01	6.01 ± 0.02	0.28	2.70
U4115-05	925.00 , 3822.00	07:57:03.97 14:22:26.30	-4.86 ± 0.06	1.35 ± 0.02	1.54 ± 0.05	4.26 ± 0.10	0.18	1.92
U8760-01	2932.65 , 3042.88	13:50:50.73 38:01:48.27	-4.80 ± 0.07	1.28 ± 0.02	3.60 ± 0.07	4.16 ± 0.05	0.22	0.51
E115-021-01	505.00 , 1425.43	02:37:54.24 -61:18:45.39	-4.78 ± 0.03	1.48 ± 0.01	2.74 ± 0.03	4.91 ± 0.04	0.12	2.10
IC1959-01	395.93 , 1110.70	03:33:20.36 -50:23:35.17	-5.43 ± 0.05	1.46 ± 0.01	3.16 ± 0.03	6.88 ± 0.04	0.06	3.13
IC1959-03	670.10 , 1963.78	03:33:15.70 -50:23:39.77	-5.42 ± 0.05	1.54 ± 0.01	2.23 ± 0.02	4.85 ± 0.04	0.18	2.20
KK27-01	2377.27 , 3224.14	03:21:01.00 -66:19:13.72	-5.22 ± 0.08	1.59 ± 0.01	2.84 ± 0.08	4.25 ± 0.08	0.04	0.20
KK65-01	2016.4 , 2749.84	07:42:39.75 16:34:37.65	-6.12 ± 0.08	1.48 ± 0.02	2.75 ± 0.01	4.32 ± 0.01	0.21	0.88
N1311-03	2869.85 , 2768.65	03:20:04.05 -52:11:34.39	-6.47 ± 0.03	1.66 ± 0.01	2.63 ± 0.01	5.14 ± 0.01	0.16	0.86
N784-02	3337.92 , 1645.64	02:01:12.29 28:50:50.86	-6.09 ± 0.05	1.57 ± 0.01	1.83 ± 0.01	3.41 ± 0.01	0.13	1.80
U685-02	3403.67 , 2455.21	01:07:26.77 16:40:30.71	-4.66 ± 0.03	1.74 ± 0.01	1.91 ± 0.03	3.22 ± 0.04	0.06	1.68
U1281-01	1439.38 , 3836.35	01:49:38.95 32:35:09.73	-7.40 ± 0.03	1.25 ± 0.01	2.75 ± 0.02	5.05 ± 0.03	0.10	2.13
U3974-05	1729.83 , 2874.48	07:41:54.57 16:48:33.71	-8.71 ± 0.05	1.33 ± 0.02	3.08 ± 0.01	8.88 ± 0.01	0.11	1.07

Chapter 3

Specific frequencies and structural parameters of globular clusters from 63 nearby low-mass dwarf galaxies

Contents

3.1 Introduction

3.1.1 Globular Cluster Systems

The traditional view of old globular clusters (GCs) is that they are simple stellar systems composed of a few to several hundreds thousand stars with homogeneous metal abundances. This makes the study of their integrated-light properties an extremely valuable tool to trace the star formation history of their host galaxies and probe differences or/and similarities between GC populations among galaxies of different luminosities and morphological types. Recent findings that some of the most massive, old Galactic GCs are actually composed of multiple stellar populations with slightly different chemical abundances (e.g. Bedin et al. 2004; Piotto et al. 2007) make the old GC populations even more attractive. It is challenging to find out in what environment such complex clusters could have formed and what this tells us about their origin and if they have analogs in other galaxies. A comparison of many different globular cluster systems (GCSs) is required in order to test various scenarios proposed for the assembly of rich GCSs.

GCs are observed in vast numbers in massive early-type galaxies (e.g. Harris et al. 2006b) and their integrated-light properties were extensively studied in the last decade (e.g. Hilker et al. 1999; Kundu & Whitmore 2001; Larsen et al. 2001; Goudfrooij et al. 2003; Puzia et al. 2002, 2004; Harris et al. 2006a; Rejkuba et al.

2007; Jordán et al. 2007; Wehner et al. 2008; Peng et al. 2008) with the aim to understand how such populous GCSs were assembled. These studies revealed the discovery of *i*) the bimodal metallicity/color distribution of GCs (e.g. Ashman & Zepf 1992; Gebhardt & Kissler-Patig 1999; Puzia et al. 1999; Kundu & Whitmore 2001) and *ii*) the presence of young/intermediate age massive star clusters in merging, starburst and irregular galaxies (e.g. Whitmore & Schweizer 1995; Goudfrooij et al. 2001; Puzia et al. 2002; Schweizer 2002; Goudfrooij et al. 2007).

From the point of view of GCS assembly, three scenarios for galaxy formation have been presented to explain these findings. The first scenario is the *hierarchical* build-up of massive galaxies from pregalactic dwarf-sized gas fragments (Searle & Zinn 1978) in which the metal-poor GCs form *in situ* while the metal-rich GCs originate from a second major star formation event (Forbes et al. 1997) or infalling gaseous fragments, the so-called mini-mergers at high redshifts (Beasley et al. 2002). The *dissipative merger* scenario (e.g. Schweizer 1987; Ashman & Zepf 1992; Bekki et al. 2002) assumes that the metal-poor GCs were formed early in "Searle-Zinn" fragments while metal-rich (and younger) GCs formed during major merger events of galaxies with comparable masses (Spiral–Spiral, Elliptical–Spiral, etc.). The *dissipationless merging and accretion* scenario incorporates the classical monolithic galaxy collapse in which the galaxies and their GCs were formed after which the dwarf galaxies and their GCs were accreted by giant galaxies (Zinn 1993; Côté et al. 1998, 2002; Hilker et al. 1999; Lee et al. 2007). For detailed discussion on the GCS formation scenarios and properties of GCs in various galaxy types we refer the reader to Kissler-Patig (2000); van den Bergh (2000b); Harris (2001, 2003); Brodie & Strader (2006).

3.1.2 The Role of Dwarf Galaxies

Although major mergers are found to be very common (e.g. Conselice et al. 2008), observations and theoretical predictions reveal that they cannot fully account for the morphological evolution from late to early-type galaxies (e.g. Lotz et al. 2008) and additional less violent processes such as gas consumption, gas stripping or minor mergers are required. Successive minor mergers were shown to lead to the gradual transformation of spiral galaxies into elliptical-like systems (Bundy et al. 2007; Bournaud et al. 2007). The prediction of the hierarchical growth of massive galaxies through merging of many dwarf-sized fragments at early times is backed by the steepening of the faint-end slope of the galaxy luminosity function with redshift (e.g. Ryan et al. 2007; Khochfar et al. 2007). In addition, the fraction of low-mass peculiar/irregular galaxies is the dominant population and increases with redshift (z) (e.g. Conselice et al. 2008). Hubble Ultra Deep field studies show that *mainly* dwarf-sized galaxies exist at $z > 6$ (e.g. Stiavelli et al. 2004). Hence, nearby dIrr galaxies may thus represent the probable *surviving* building blocks of massive galaxies.

Evidence for accretion events of dwarf galaxies and their dissolution in the Galactic potential is manifested by numerous stellar over-density streams observed in the Milky Way, M31, and other galaxies (e.g. Ibata et al. 2001; Grillmair 2006; Liu et al. 2006; Martinez-Delgado et al. 2008, and refs therein). Among those, the best example of a recent accretion event is the Sagittarius dwarf galaxy, which is currently being added to the Milky Way halo together with its globular clusters (e.g., Ibata et al. 1994). In the view of the hierarchical galaxy assembly scenario, many more

minor accretion/merger events of dwarf sized galaxies are expected during the evolution of a giant galaxy. The Pipino et al. (2007) galaxy evolution and GC formation model, in which a low number of blue (metal-poor) GCs in massive galaxies are predicted to form in the initial monolithic collapse, contrasts with observations and suggests that subsequent accretion of such GCs from low-mass dwarfs is required. However, the observed large ratio between metal-poor GCs and metal-poor field halo stars in massive galaxies (Harris 2001; Harris & Harris 2002) implies that, if such dwarfs were later accreted, they must have large GC specific frequencies (S_N is the number of GCs per unit galaxy luminosity Harris & van den Bergh 1981) in order to keep the ratio high. This is in line with the high specific frequencies observed in low-mass early and late-type dwarfs in clusters (Durrell et al. 1996; Miller et al. 1998; Seth et al. 2004; Miller & Lotz 2007; Georgiev et al. 2006; Peng et al. 2008) and in group/field environments (Olsen et al. 2004; Sharina et al. 2005; Georgiev et al. 2008a; Puzia & Sharina 2008).

In this study we present the results from the combined analysis of old GCs in 70 dwarf galaxies with focus on dIrrs (the sample contains 55 dIrrs, 3 dEs, 5 dSphs and 5 late-type dwarf spirals). Old GC candidates were found in 30 dIrrs, 2 dEs, 2 dSphs and in 4 Sms. Their colors, luminosities and structural parameters are compared with the old GCs in the best studied Local Group dIrr galaxies, i.e. the Large and Small Magellanic Clouds. Those GC properties are directly compared with those of the Galactic "Young Halo" (YH) GCs, which have been suspected to be of external origin and are discussed in the context of the dissipationless accretion scenario of dwarf galaxies. We also discuss the interesting behavior of the GC specific frequency found in dwarf and giant galaxies, the mass fraction in globular clusters and what are the implications for the GC formation efficiencies.

3.2 Data

3.2.1 Observations

The current study is based on the HST/ACS archival data from programs SNAP-9771 and GO-10235, Cycle 12 and 13 respectively (PI: I. Karachentsev) and archival HST/ACS data (GO-10210, PI: B. Tully) described in Georgiev et al. (2008a). The non-dithered 2×600 s F606W and 2×450 s F814W exposures for each galaxy were designed to reach the Tip of the Red Giand Branch (TRGB) at $M_I = -4.05, M_V = -2.5$ mag (Da Costa & Armandroff 1990) and provide TRGB distances to the sample dwarf galaxies as published in Karachentsev et al. (2006, 2007). All galaxies are found to reside in the isolated outskirts of nearby (≤ 6 Mpc) galaxy groups (Sculptor, Maffei 1& 2, IC 342, M 81, CVn I cloud) with exception of 3 dwarfs at 9 Mpc.

The program SNAP-9771 observed 34 low-mass galaxies, of which 26 are dIrrs, 2 dEs, 4 dSphs and 2 late-type spiral dwarf galaxies: NGC 247 and NGC 4605. The program GO-10235 contains 15 targets of which 10 are dIrrs, 1 dE, 1 dSph and 3 late-type spirals: ESO 137-18, ESO 274-01 and IC 4247. We have excluded the very distant spiral PGC 47885 at ~ 200 Mpc and the Magellanic-type spiral ESO 383-087, whose F606W image has 0 exposure time, from further analysis. All galaxies in our final sample have published TRGB distance measurements (Karachentsev et al. 2006, 2007). A summary of their general properties is given in Table 3.1. In column (1) the galaxy IDs are listed, and in columns (2) and (3) their coordinates; columns

(4) and (5) contain the morphological classifications from LEDA[1] and NED[2], (6) and (7) the distances and distance moduli, (8) and (9) the absolute magnitudes and colors (measured in this work, see Sect 3.3.1), and in column (10) their HI mass (obtained from LEDA).

The additional archival HST/ACS data consists of 19 Magellanic-type dIrr galaxies residing in nearby ($2-8$ Mpc) associations composed mainly of dwarfs with similar luminosities as the target galaxies, with the only exception that the previous sample was composed of dwarfs located in isolated associations of only few dwarfs (Tully et al. 2006), while the dwarfs in our new dataset are in the halo regions of groups which contain massive dominant galaxies such as M 83 and Cen A (see Table 3.1, Karachentsev et al. 2006, 2007,). The HST/ACS F606W and F814W imaging of the previous data was also designed to reach the tip of the red giant branch (TRGB) and measure TRGB distances (Tully et al. 2006).

In total, our sample consists of 55 dIrrs, 3 dEs and 5 dSphs in the field environment, either in lose associations of dwarfs or in the remote halo regions of nearby groups. All dwarfs have apparent diameters smaller than the HST/ACS field of view which provided us with a good sampling of their GCSs.

3.2.2 Data Reduction and Photometry

The image processing and photometry was performed in identical manner as in our previous study (Georgiev et al. 2008a), and is summarized in the following. We retrieved archival HST/ACS images in F606W and F814W filters which were processed with the ACS reduction pipeline and the MULTIDRIZZLE routine (Koekemoer et al. 2002). To improve the object detection and photometry we have modeled and subtracted the underlying galaxy light using a circular aperture median kernel of 41 pixel radius. The kernel aperture radius is large enough to preserve the structure of the GC candidate profiles, which were semi-resolved under the high ACS resolution.

Object detection (4σ above the backrgound) and initial aperture photometry (in 2,3,5 and 10 pixel radius) was performed with the IRAF[3] DAOPHOT/DAOFIND and PHOT routines. Conversion from instrumental magnitudes to the STMAG system and aperture corrections from 10 pixel to infinity were performed using the ACS photometric calibration prescription by Sirianni et al. (2005).

3.2.3 GC Candidate Selection

The GC candidate (GCC) selection was based, first, on the expected colors for old (> 4 Gyr) Simple Stellar Population (SSP) models (Anders & Fritze-v. Alvensleben 2003; Bruzual & Charlot 2003) and typical colors of old Galactic GCs. Namely, objects in the color range $-0.4 \leq$(F606W-F814W)≤ 0.2 (corresponding to $0.7 < V-I < 1.5$). Second, we have imposed a faint magnitude cut-off at the TRGB ($M_V = -2.5$, $M_I = -4.05$; Da Costa & Armandroff 1990; Lee et al. 1993) converted

[1] http://leda.univ-lyon1.fr/

[2] http://nedwww.ipac.caltech.edu/

[3] IRAF is distributed by the National Optical Astronomy Observatories, which are operated by the Association of Universities for Research in Astronomy, Inc., under cooperative agreement with the National Science Foundation.

to apparent magnitudes according to the distance to each galaxy as derived by Tully et al. (2006) and Karachentsev et al. (2006, 2007). This is $\sim$5 mag fainter than the typical GC luminosity function turnover magnitude for metal-poor globular clusters at $M_{V,TO} = -7.66 \pm 0.1$ mag (e.g. Di Criscienzo et al. 2006).

Due to the deep ACS imaging and its high spatial resolution (1 ACS pixel = 1.2 pc at a mean distance to our sample dIrrs of 5 Mpc), a typical LG GC with half-light radius of $r_{\rm h} = 3$ pc is resolved and has a considerably different light profile from a stellar PSF. We used IMEXAM to confine the initial GCC selection to round objects (FWHM$_{F606W}$ $\simeq$FWHM$_{F814W}$) with an IMEXAM ellipticity $\epsilon \leq 0.15$ within a fixed $r = 5$ pix aperture radius and a Moffat index $\beta = 2.5$, typical for stellar profiles. As we showed in Georgiev et al. (2008a), the upper IMEXAM ϵ limit allows selection of GC candidates with true ellipticity up to $\epsilon < 0.4$. The final ellipticities and half-light radii ($\epsilon,\ r_{\rm h}$) were measured with ISHAPE (see Sect. 3.2.4).

The last GC candidate selection step is to measure the difference between the 2, 3, and 5 pixel aperture photometry. These m_2-m_3 vs m_2-m_5 concentration indices separate well the stellar PSFs from extended GCCs and the majority of the contaminating background galaxies during the automated GC candidate selection.

We have detected 57 GC candidates in 17 dIrrs, 6 GCCs in 2 dSph, 25 GCC in 2 dEs and 25 GCCs in 4 Sm dwarfs. Therefore, in combination with the 60 GCCs from Georgiev et al. (2008a) we have in total 117 GCCs in 30 dIrrs. Their color and magnitude distributions are presented in Sect. 3.3.2.

The final GC candidate photometry was derived from curve of growth analysis for each individual object from images iteratively cleaned from contaminating sources within the photometric apertures. A detailed description of the iterative procedure is provided in Georgiev et al. (2008a). In brief, it involved an object detection based on convolution of the image with two different Gaussian profiles using the SExtractor package (Bertin & Arnouts 1996). The detected objects were subtracted and replaced with the background value as evaluated from 60 pixel background mesh, thus leaving only the extended GC candidates with all associated pixels within 0.5σ above the background. The image noise characteristics were restored using the ACS header keywords and the IRAF MKNOISE routine. On these final images, a curve of growth analysis was performed out to 50 pix aperture radius for each GC candidate. The total luminosity is represented by the asymptotic magnitude of each of these GCCs.

Conversion from STMAG to Johnson/Cousins was performed using the transformation and dereddening coefficients (for a G2 star) provided in Sirianni et al. (2005). The foreground reddening $E(B-V)$ to each galaxy was obtained from Schlegel et al. (1998).

3.2.4 Structural parameters

To derive the GCC structural parameters (half-light radius, $r_{\rm h}$, and ellipticities, ϵ) we have used the ISHAPE algorithm (Larsen 1999), which models the object's surface brightness profile with analytical models convolved with a subsampled PSF. Since most clusters are marginally resolved, a very good knowledge of the ACS PSF is required to obtain reliable measurements of their sizes. Testing the influence of the

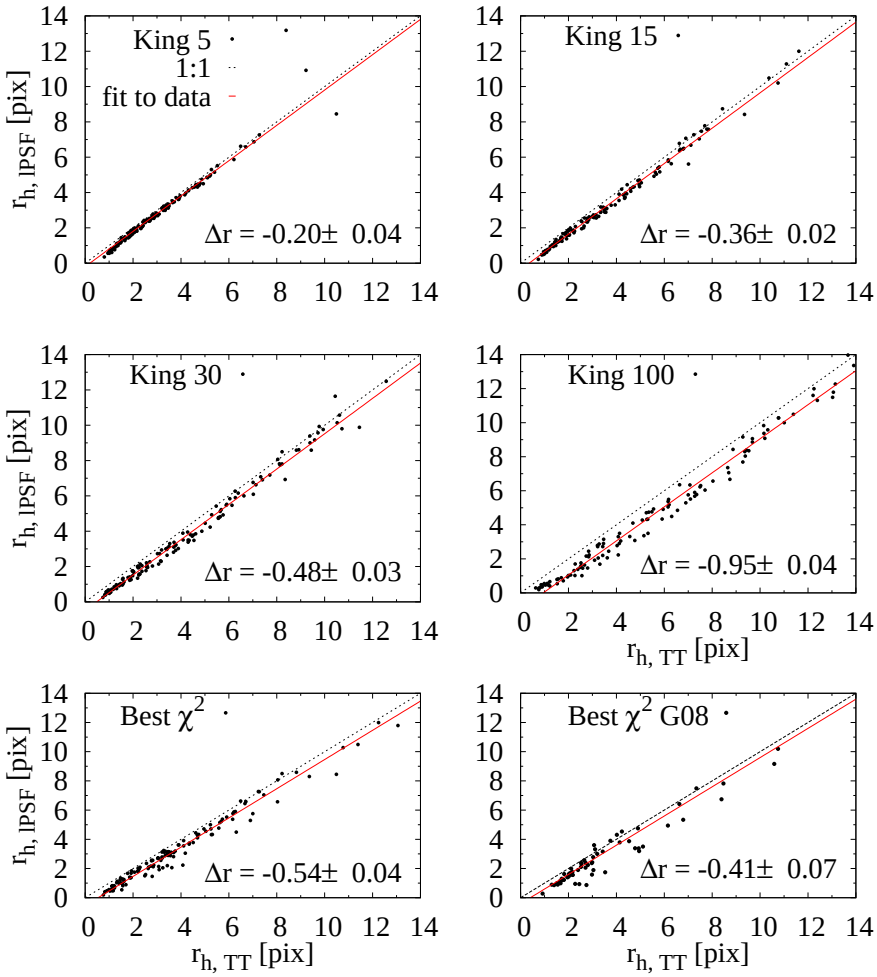

Figure 3.1: Comparison between $r_{\rm h}$ derived with TinyTim (TT) and empirical PSFs build from the images (lPSF). From top to bottom are shown relations for different King model concentration parameters and the best χ^2 fit models, respectively. The lower right panel shows the best χ^2 from our previous study (Georgiev et al. 2008a).

PSF library, we performed a comparison between the $r_{\rm h}$ measured using TinyTim[4] model PSFs (TT-PSF) and the empirical, local PSF (lPSF), which we build from stars in the image for each galaxy with GCCs.

The ten times sub-sampled TT-PSF was convolved with the charge diffusion kernel. The position-dependent lPSFs was built from images typically having more than 20 isolated stars across the ACS field. Both PSF types were used with ishape to model the clusters profiles for all King model concentration parameters ($C = r_{\rm tidal}/r_{\rm core} = 5, 15, 30, 100$). The final cluster parameters were adopted from the best χ^2 fit model for both PSFs. For the final cluster half-light radius we have adopted the geometric mean from the ishape FWHMs measured along the semi-major and semi-minor axis (w_y and w_y), i.e. $r_{\rm h} = r_{{\rm h},w_y}\sqrt{w_x/w_y}$.

Figure 3.1 shows a comparison between the $r_{\rm h}$ derived from the best χ^2 TT

[4]http://www.stsci.edu/software/tinytim/tinytim.html
The TinyTim software package properly takes into account the field-dependent WFC aberration, filter passband effects, charge diffusion variations and varying pixel area due to the significant field distortion in the ACS field of view (Krist & Hook 2004)

and lPSF models. It is obvious that for every C the $r_{\rm h,lPSF}$ values are smaller than the $r_{\rm h,TT}$ values (see Δr values in Fig. 3.1). This shows that the TinyTim PSFs are sharper, although convolved with the diffusion kernel, than the empirical lPSFs which represent the real imaging conditions (charge diffusion, telescope focus breathing, drizzle effects, etc.).

In this study we are compiling data from our previous study (Georgiev et al. 2008a) in which the $r_{\rm h}$ were derived from the best χ^2 TinyTim PSF due to the lack of enough good PSF stars for modeling empirical PSF in the field of those extremely isolated dIrrs. Therefore, we convolved the GCs from that study with the local PSF derived from the image of ESO 223-09, which has the highest number of PSF stars (69). In the bottom right panel of Fig. 3.1 we show the $r_{\rm h}$ derived with the TinyTim PSF versus the empirical PSF for the best χ^2 model. As can be seen, the values computed with TT-PSFs are ~ 0.4 pix larger than the corresponding sizes computed with the empirical lPSFs.

A similar difference between the empirical and TinyTim PSF of ~ 0.5 pix (the $r_{\rm h,TT}$ being larger) was also previously reported in the ACS study of the Sombrero galaxy by Spitler et al. (2006) (their Fig.2), where a fixed concentration index $C = 30$ was assumed. In the following, we will use the structural parameters of GCCs obtained with the empirical lPSFs.

3.2.5 Completeness Tests

Artificial clusters were modeled with the MKCMPPSF and MKSYNTH routines in the BAOLAB package (Larsen 1999). The procedure includes convolution of empirical PSFs with analytic KING profiles for all concentrations (C = 5, 15, 30 and 100). For the completeness tests we chose the galaxy ESO 223-09 which has the highest surface brightness, foreground extinction ($E(B-V) = 0.260$) and foreground star contamination in our sample. In Figure 3.2 are shown a color composite image of ESO 223-09 (bottom right) and five other dwarf irregular galaxies created from the I, the average of V and I, and $V-$band HST/ACS images in the red, green and blue channels, respectively. The galaxies in the top row panels are among the most distant (~ 10 Mpc) and isolated (unknown or no group affiliation) objects in our dwarf galaxies sample (cf. Tables 3.1 and 2.2). The mean distance of the other galaxies in the figure is ~ 5 Mpc. Their luminosities are in the range $M_V \simeq -12$ and -16.5 mag ($L \simeq 0.54-34\times10^7 L_\odot$), typical for the entire sample dIrrs. We point out that this is the most conservative estimate of our sample photometric completeness and all other galaxies have more complete photometries. Also ESO 223-09 contains the highest number (69) of PSF stars. To sample the parameter space typical for colors and luminosities of old GCs ($t \geq 4$ Gyr) we generated synthetic clusters in the range $21 <$ F606W < 26 mag (STMAG) with the fainter limit matching the TRGB at the distance of ESO 223-09 (Karachentsev et al. 2007). The colors of the artificial clusters were spread over the range $-0.4 < F606W - F814W < 0.25$ ($0.5 < V - I < 1.5$) in fourteen color bins with 0.05 mag step. For each color bin 200 artificial clusters were randomly placed across the synthetic image. This step was repeated 100 times thus providing 20 000 objects per color bin or in total 280 000 artificial clusters for the completeness test for one King profile concentration. The same procedure was applied to all four concentrations provided within BAOLAB (Larsen 1999).

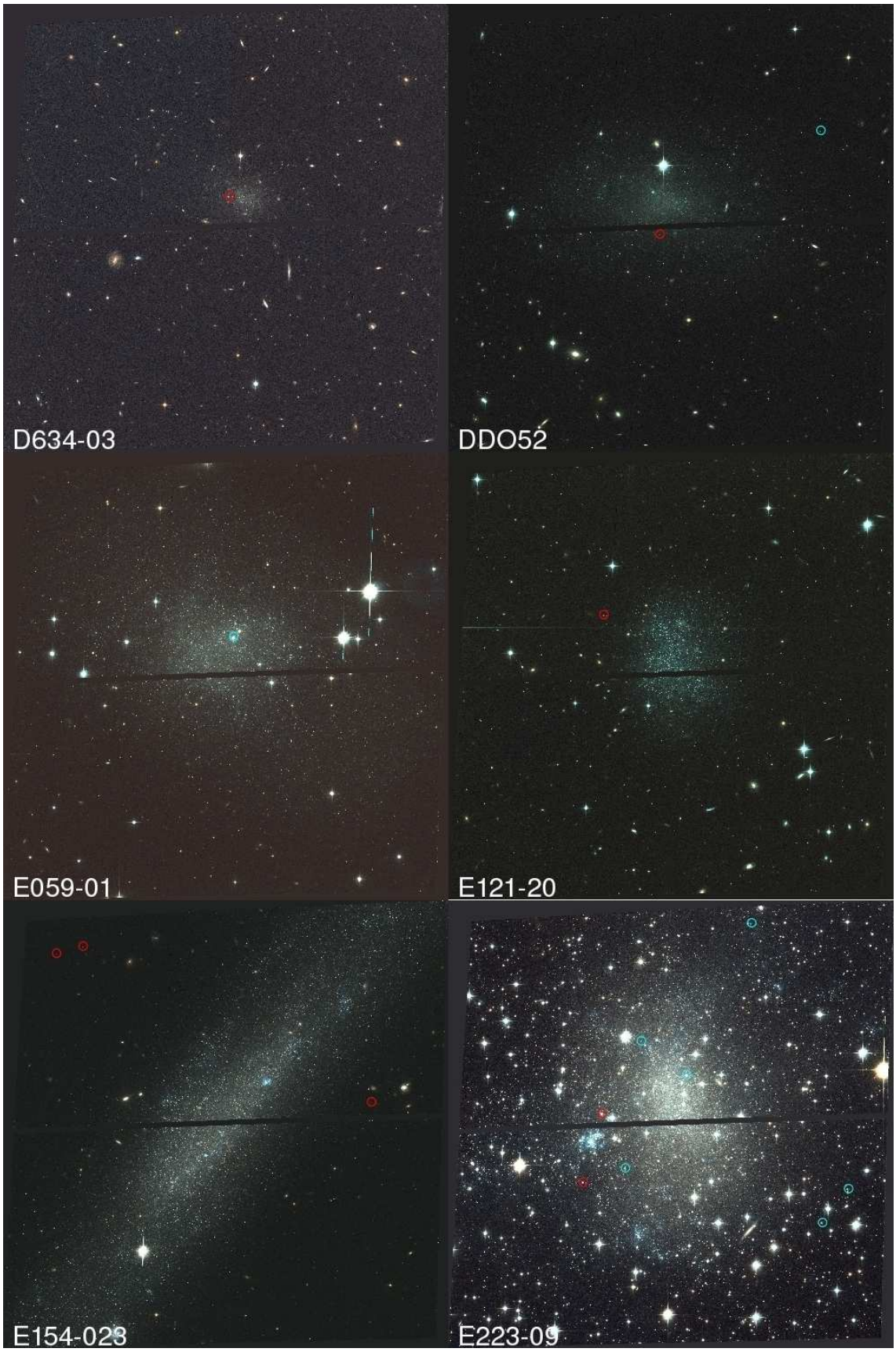

Figure 3.2: Color composite images of six dwarf irregular galaxies created from the I, the average of V and I, and $V-$band HST/ACS images in the red, green and blue channels, respectively. With light blue and red circles are shown the blue and red GCCs, respectively.

The synthetic images consist of the modeled clusters on a constant (0 ADUs) background, matching the mean background value of the original ACS images. Every synthetic image, containing 200 objects, was then added to the original ESO 223-09 image, thus preserving the image background level and noise characteristics. Then the final images were pipelined through the same routines for object detection, photometry, and GCC selection as the ones used in this and the Georgiev et al. (2008a) study.

In Figure 3.3 we show the color-magnitude diagrams (CMDs) and concentration plots of the retrieved artificial clusters for the four King models. The rectangle in the left-column panels indicates the region in which the artificial clusters were modeled and later selected. After applying the color-magnitude and the IMEXAM FWHM and ϵ cuts, the final cluster selection was based on their concentration as derived from the difference between their magnitudes in 2, 3 and 5 pixel aperture radius. The right-column panels of Figure 3.3 show the $m_2 - m_3$ vs. $m_2 - m_5$ diagrams. The objects that survived all the selection criteria were used to compute the completeness as a function of the cluster magnitude. In Figure 3.4 we present the completeness functions in V and I for all King models.

Figure 3.4 shows that for the case of a galaxy with high surface brightness, strong foreground reddening and foreground star contamination (cf. Fig. 3.2), the 90% completeness limit for extended sources is reached at $M_V \simeq -4.5$ mag. As expected, the completeness is a function of the cluster concentration, in the sense that more extended clusters suffer stronger incompleteness as their detection and correct magnitude measurement are easily affected by the variable galaxy background and bright foreground stars. We point out that this is the least complete case in our sample and that all other target galaxies have fainter completeness limits.

3.2.6 Background Contamination

Background contamination from bulges of compact and starbursting galaxies at intermediate redshifts, which resemble the colors and structural appearance of GCs, need to be taken into account. We have already assessed (Georgiev et al. 2008a) the expected contamination for the ACS field of view and objects with identical magnitude and size distributions as GCs in galaxies within 8 Mpc using the Hubble Ultra Deep Field (HUDF)[5]. The expected number of contaminating background galaxies increases significantly for $V_0 \geq 25$ mag ($M_V \geq -4$), well beyond the luminosity distribution of GCs. Nevertheless, down to this limit a contamination of up to 2 objects per field is expected.

3.3 Results

3.3.1 Integrated Galaxy Magnitudes

Only six of the dwarf galaxies in our sample have total $V-$band magnitudes available in the literature while the majority of them only have B magnitudes. However, good knowledge of the V-band magnitudes is required to estimate their GC specific frequencies for a robust comparison with previous studies. We, therefore, perform integrated-light photometry on the ACS images and derive their total magnitudes.

[5] http://heasarc.nasa.gov/W3Browse/all/hubbleudf.html

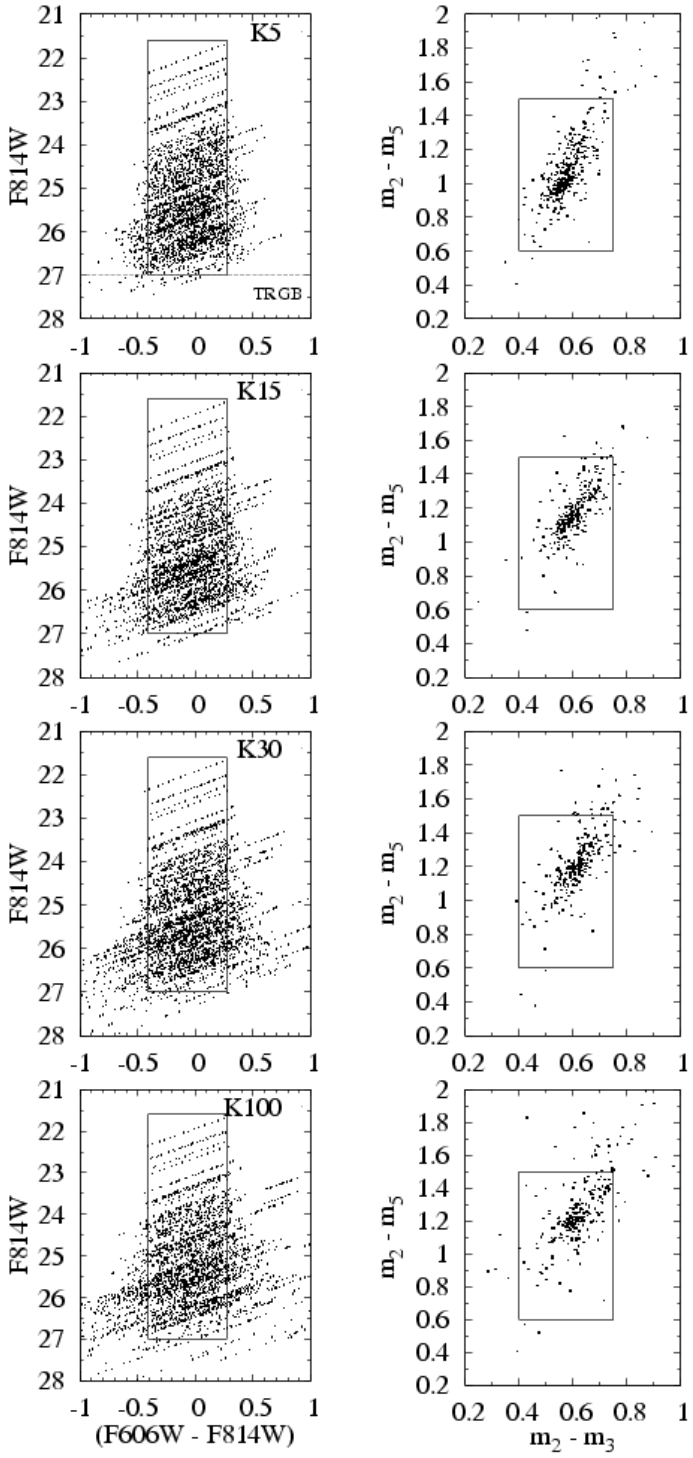

Figure 3.3: *Left panels:* Color-magnitude diagram of the artificial clusters with King profile concentrations $C = 5, 15, 30$ and 100 from top to bottom, respectively. The solid line rectangle indicates the color-magnitude region used to generate artificial clusters and their subsequent selection. *Right panels:* Magnitude concentration index of the artificial clusters as defined by their 2,3 and 5 pixel aperture radius magnitudes. The rectangle defines the final cluster selection.

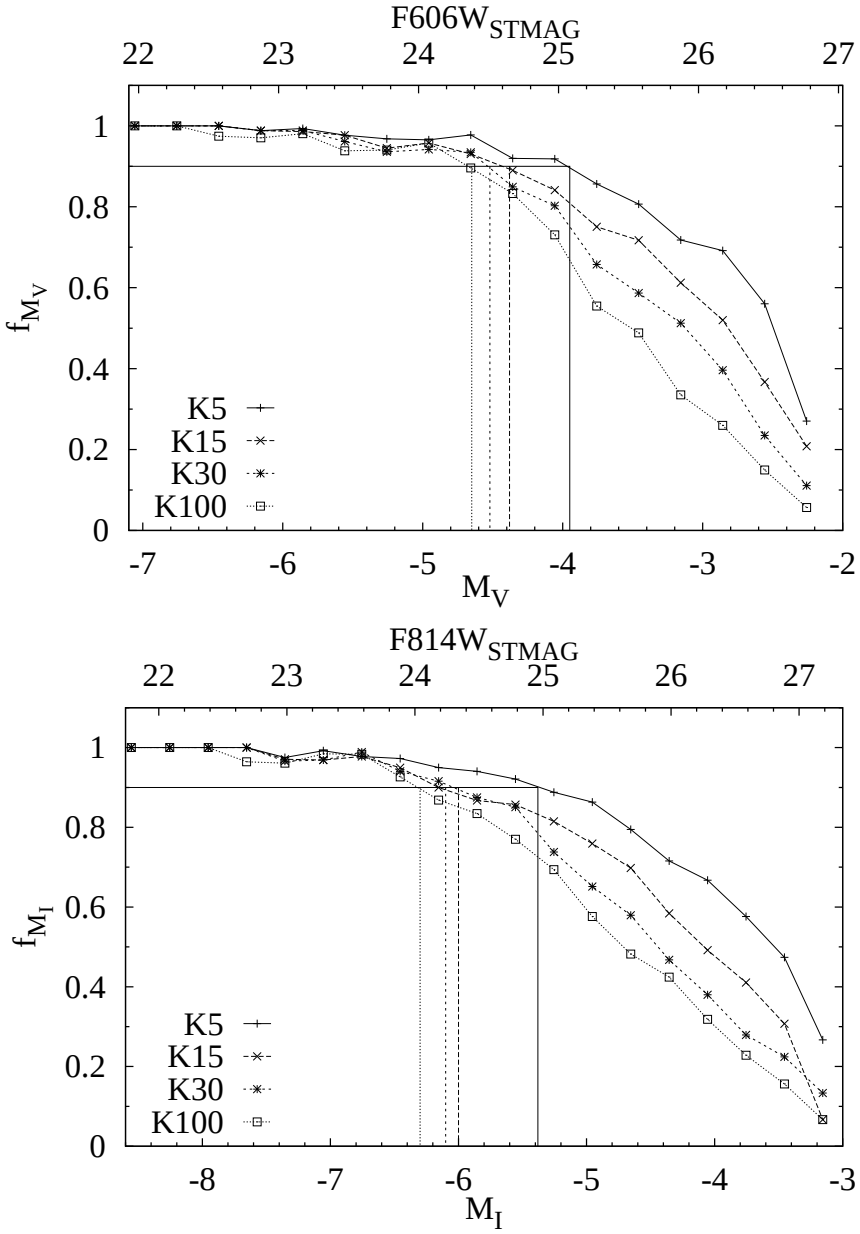

Figure 3.4: Completeness as a function of synthetic cluster magnitude for V and I in the top and bottom panels, respectively. To convert from instrumental STMAG to the Johnson/Cousins photometric system, we have used the transformation relations tabulated in Sirianni et al. (2005). To convert from apparent to absolute magnitudes, we have used the distance modulus of $m - M = 29.06$ mag to ESO 223-09 as derived from the TRGB measurement by Karachentsev et al. (2007).

Bright foreground stars and background galaxies were masked out and replaced with the local background level and noise. The median smoothed image of each galaxy was used to estimate the center of the galaxy. However, for most dwarfs the derived centers were not representative of the visual center of the extended galaxy light, but rather the region with the strongest starburst. Thus, we adopted the geometric center of the isointensity contour at the 10σ level above the background as the galaxy center. Since the galaxies rarely extend beyond 1500 pixel radius, the estimate of the sky value determined from the median value measured at the image corners, is representative for the true photometric background. To measure the galaxy magnitudes we used the ELLIPSE task within IRAF. The initial values for galaxy ellipticity and position angle were taken from NED. For dwarfs without published values for those parameters, we estimated the center in interactive mode with ELLIPSE, i.e. to approximate the ellipticity and position angle of the extended light (at the 10σ isointensity contour). We have measured the total galaxy magnitudes within the ellipse with radius at the Holmberg radius ($\mu_B = 26.5$) quoted in NED.

Magnitudes were adopted from NED for two spiral galaxies (ESO 274-01 and NGC 247, see Table 3.1) which were extending beyond the ACS field of view as well as for NGC 4605 which was off-center and for KKH 77 which was contaminated by a very bright overexposed foreground star. For IKN and VKN, two extremely low surface brightness dwarfs ($M_V \approx -11.5$ and -10.5 mag, respectively), we could not reliably determine their magnitudes due to an extremely bright foreground star in the former and the very low surface brightness of the latter (close to the level of background fluctuations and measurement errors). Their $V-$band magnitudes were derived from their $B-$band magnitudes assuming an average $B - V = 0.45$ mag estimated from the rest of the dwarfs. Due to the fact that UGCA 86 was centered in the middle of ACS chip 2, its Holmberg radius extended beyond the ACS field by $\sim 1'$ and, therefore, we had to extrapolate its magnitude with the gradient of the last 3 magnitude bins of its curve of growth.

Finally, the derived magnitudes were compared with the published ones for six dwarfs in our sample (DDO 52, ESO 269-58, IC 4662, NGC 5237, 4068, 4163) and found consistent within the measurement errors. The magnitudes of all galaxies are listed in Table 3.1.

3.3.2 Colors and Luminosities

In Figure 3.5 we show the color-magnitude diagrams for GCCs in dIrr, dE/dSph, and Sm galaxies, and the composite sample, combining the results from this work with our identically analyzed sample from Georgiev et al. (2008a). The color and luminosity distributions are illustrated as histograms in the top and right sub-panels, where the curves indicate non-parametric Epanechnikov kernel probability density estimates. We subdivide the samples in color into blue GCCs (bGCCs) with $V-I \leq 1.0$ mag and red GCCs (rGCCs) with $V-I > 1.0$ mag, which include the sub-sample of extremely red objects with colors $V-I > 1.4$ mag[6]. This division is motivated by the average location of the gap between the blue and red color peaks of rich GCSs in massive early-type galaxies

[6]The faintest clusters with $M_V \leq -6$ and $(V-I)_0 > 1.0$ mag are likely background contaminants which passed our selection criteria. This should be tested with follow-up spectroscopy.

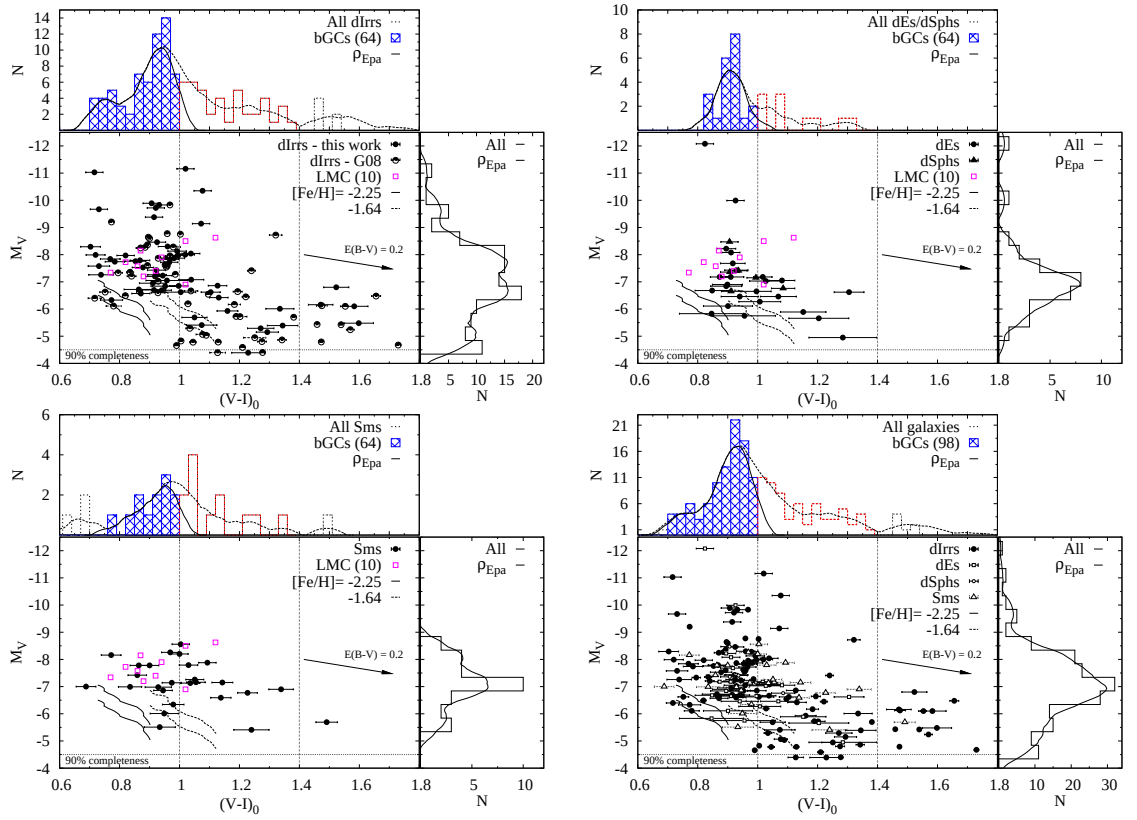

Figure 3.5: Combined color-magnitude diagram for GC candidates in dIrr galaxies (upper left panel). With filled and semi-filled circles are shown the GC candidates from the current and Georgiev et al. (2008a) study and with open squares old LMC GCs (data from McLaughlin & van der Marel 2005). The vertical dotted lines indicate the colors separating blue and red GC candidates. With thick and dashed are shown Bruzual & Charlot (2003) SSP evolutionary tracks from 3 Gyr to 14 Gyr.The top and right histograms show the GC candidates color and luminosity distributions. In the other panels are shown the respective distributions for dEs/dSphs, Sm and the combined dwarf galaxies sample.

An intriguing feature of Figure 3.5 is the lack of faint blue GCCs in our sample dIrr galaxies. Our artificial cluster test show that this is not a completeness effect as our 90% completeness limit is $M_V = -4.5$ mag (see Sect. 3.2.5). However, finding one more GC in these faint dwarfs would increase even more their already high specific frequencies (see Sect. 3.4.1). On the other hand, we do observe few clusters at $M_V \simeq -5.5$ to -6.5 mag and $(V-I) < 1.0$ mag in galaxies with dE/dSph and Sm morphology[7]. (e.g. Gebhardt & Kissler-Patig 1999).

One possibility for the apparent lack of faint blue clusters is that metal-poor ($V - I < 1.0$ mag) and low-mass GCCs ($M_V > -6.5$ mag) are younger (< 4 Gyr) than our selection. To explore this effect we investigate stellar evolution fading according to SSP models (e.g. Bruzual & Charlot 2003). Passive aging of a simple stellar population from 3 to 14 Gyr reddens its $(V - I)$ color by ~ 0.15 mag and fades its M_V luminosity fainter by ~ 1.5 mag. This is illustrated in Figure 3.5 with

[7] We note that all absolute magnitudes were calculated using the newly determined distance moduli by Tully et al. (2006) and Karachentsev et al. (2006, 2007) which are fainter by ~ 0.5 mag on average from the values listed in Karachentsev et al. (2004), hence the GCCs are brighter in absolute magnitudes.

evolutionary tracks for two metallicities ([Fe/H] = −2.25 and −1.64 dex) and two clusters masses $M_{\rm cl} = 3 \cdot 10^4$ and $5 \cdot 10^4\,M_\odot$, based on Bruzual & Charlot (2003) SSP models. If some of the bluest GCCs are indeed younger clusters they will end up on the faint-end of the luminosity function after a Hubble time of passive evolution. However, those clusters would have to have unusually low metallicities ([Fe/H] ≤ -2.0), and interesting result that calls for spectroscopic confirmation. Previous spectroscopic analyses of GCs in other dwarf galaxies show that their blue colors are in general consistent with old ages and low-metallicities. However, some of these clusters show spectroscopic intermediate ages ($\sim 4\,$Gyr), in particular in dIrrs (Puzia & Sharina 2008). Intermediate-age clusters will fade due to stellar (and dynamical) evolution, as described above. An alternative explanation for the lack of old, metal-poor, low-mass clusters in dIrr galaxies may be selective reddening of such objects. The reddening vector in the CMDs of Figure 3.5 shows that a relatively mild reddening of $E_{(B-V)} = 0.2$ mag is enough to dislocate intrinsically blue GCCs to the red GCC sub-sample. All previous findings should be tested with spectroscopic observations. Although the current dIrr GC sample is one of the most complete to date, stochastic effects due to low number statistics could still be an issue.

Another interesting feature in the CMDs is the presence of a few relatively bright GCCs in dIrr and dE/dSph, which are similar in color and magnitude to $\omega\,$Cen and M 54 and are located in the nuclear regions of their host galaxies. Such bright object do not appear in the Sm sub-sample. Given the stochastic star formation histories of dwarf irregular galaxies it is an unexpected discovery that low-mass dIrr galaxies would be nucleated. A dedicated study of the properties of these GCCs will be presented in a forthcoming study.

The probability density estimates for all sub-samples give the highest probability values for in the range $(V-I)_{0,\rho} \approx 0.9 - 1.0\,$mag and $M_{V,\rho} \approx -7.5$ to -6.5 mag. Gaussian fits to the bGCC luminosity function give peak values in the range $M_{V,G} = -7.42$ to $-6.99 \pm 0.11\,$mag with $\sigma = 1.12 - 1.68 \pm 0.15$ mag. The color distributions of GCCs in our sample galaxies peak at values typically found in other low-mass dwarfs (Seth et al. 2004; Sharina et al. 2005; Georgiev et al. 2006, 2008a), and are very similar to the canonical blue peak color of rich GCSs in massive early-type galaxies (e.g. Peng et al. 2008). For comparison we also show ten of the brightest old LMC GCs (McLaughlin & van der Marel 2005). There are three more LMC clusters that are fainter than $M_V = -6.5\,$mag, however, without available $V-I$ colors.

Figure 3.6 shows the luminosity functions of the blue and red GCCs in the top and bottom sub-panels, respectively. Thick curves are Epanechnikov kernel density estimates. We find that the rGCCs are biased to fainter luminosities compared to the bGCC sub-sample. This indicates that these objects are strongly affected by background contamination. Gaussian fits to the histogram distributions return $M_V = -7.53 \pm 0.17\,$mag and $\sigma = 1.15 \pm 0.11$ for dIrr, $M_V = -7.12 \pm 0.10\,$mag and $\sigma = 1.09 \pm 0.11$ for dE/dSph, and $M_V = -7.41 \pm 0.08\,$mag and $\sigma = 0.92 \pm 0.12$ for Sm galaxies (note the different axes scales when comparing with Fig. 3.6). Assuming a typical $M/L_V = 1.8$ obtained for old metal-poor Magellanic GCs (McLaughlin & van der Marel 2005) the turnover magnitude translates to M$\simeq 1.6 \times 10^5\,$M$_\odot$.

The GCC luminosity function turn-over magnitude for dIrrs is slightly brighter

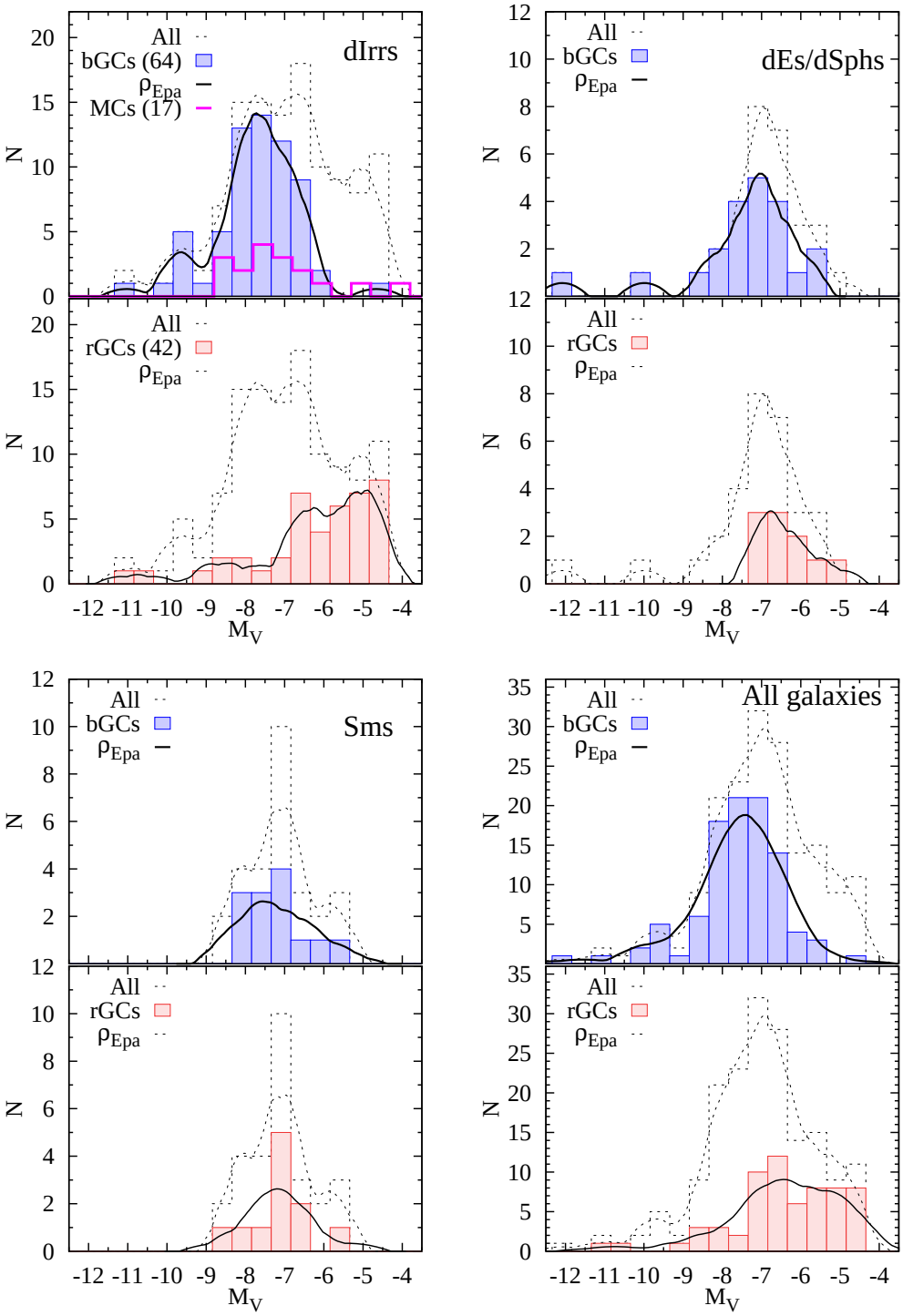

Figure 3.6: Luminosity distributions of the selected as blue and red GCs on the top and bottom panels, respectivey. With hatched histograms are shown the respective GC candidates luminosity distribution while with open histogram is the total. In both panels, thick and dotted lines show the non-parametric Epanechnikov kernel density estimates. With thick line open histogram is also shown for comparison the luminosity distribution of the LMC old GCs (data from McLaughlin & van der Marel 2005).

that those for dE/dSph and Sm galaxies, which shows significantly broader luminosity function peaks extending to fainter magnitudes. The brighter peak magnitude in dIrrs might also imply that the GCS as whole is younger than that in early-type dwarfs and can become fainter due to stellar evolutionary fading as discussed above. This may be also due to the interplay of different formation mechanisms and ages/metallicities or simply due to contamination by background galaxies. In general, all are consistent with the luminosity function turn-over magnitude for metal-poor Galactic GCs (Di Criscienzo et al. 2006), as well as GCs in early-type dwarfs (Sharina et al. 2005; Jordán et al. 2007; Miller & Lotz 2007), and virtually identical to the turn-over magnitude of old LMC GCs at $M_V = -7.50 \pm 0.16$ mag (data from McLaughlin & van der Marel 2005).

3.3.3 Structural Parameters

The clusters half-light radii (r_h) and ellipticities (ϵ) are stable over many relaxation times (e.g. Spitzer & Thuan 1972) and, thus, contain information about the initial conditions and the dynamical evolution of clusters over a Hubble time. In particular, the cluster half-light radius is stable for > 10 relaxation times (i.e. 10 Gyr) (e.g. Aarseth & Heggie 1998), while the ellipticity decreases by a factor of two for 5 relaxation times and reaches asymptotic values around 0.1 (Fall & Frenk 1985; Han & Ryden 1994; Meylan & Heggie 1997). This theoretical estimate gives us a good proxy for comparison and analysis of the conditions at which present-day GCs evolved.

Half-Light Radii

In Figure 3.7 we present the measurements of r_h for GCCs in our sample galaxies. The majority of GCCs lies below the empirically established relation $\log\{r_\mathrm{h}\} = 0.25 \times M_V + 2.95$ (Mackey & van den Bergh 2005), which forms the upper envelope of Galactic GCs in the M_V vs. r_h plane. The brightest clusters in Fig. 3.7 have masses $> 10^6 M_\odot$, similar to ω Cen and M 54. Some of these brightest GCCs, that reside in the nuclear regions of their hosts, tend to lie on or above that envelope (towards larger r_h at a given M_V), which seems typical for nuclear star clusters (e.g. Böker et al. 2004; Haşegan et al. 2005). This region is also occupied by the peculiar Galactic GCs ω Cen, NGC 2419, NGC 2808, NGC 6441 and M 54, the nucleus of Sagittarius dSph.

The half-light radius distribution of the bGCCs and rGCCs is shown in the bottom sub-panels of Figure 3.7. On average, the blue GCC sub-population appears more extended than their rGCC counterpart in all sub-samples, by about 9%, however with low statistical confidence. On average, the most compact bGCC population is found in dE/dSph host galaxies ($r_\mathrm{h,med} = 2.5$ pc), followed by bGCCs in dIrrs ($r_\mathrm{h,med} = 3.3$ pc) and Sm galaxies ($r_\mathrm{h,med} = 7.6$ pc) whose GC population is significantly incomplete due to spatial coverage (cf. Sect. 3.3.1). We find the highest value of the probability density estimate of the entire sample at $r_\mathrm{h} \sim 2.9$ pc and a median $r_\mathrm{h,med} = 3.2 \pm 0.51$ pc. These values are typical for Galactic GCs (Harris 2001). The median value of the old LMC GCs is $r_\mathrm{h,med} = 5$ pc (based on measurements from McLaughlin & van der Marel 2005).

The comparison between the r_h distribution of the total bGCC sample with the sizes of different metal-poor, Galactic GC sub-populations shows that the old halo

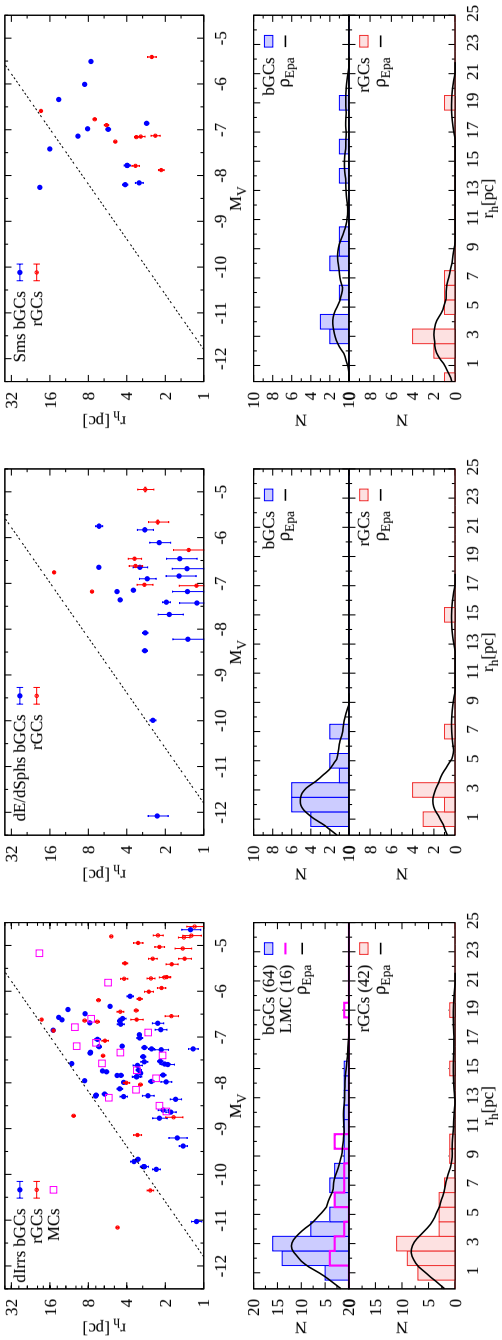

Figure 3.7: Luminosity versus half-light radius (r_h) for GCCs in dIrrs (*left panel*), dE/dSph (*middle panel*), and Sm galaxies (*right panel*). In the left panel we show old GCs in the Magellanic Clouds (McLaughlin & van der Marel 2005). The dashed line indicates the upper envelope for the distribution of Galactic GCs (Mackey & van den Bergh 2005). The lower sub-panels show the corresponding r_h distributions for the blue and red GC candidates. The thick lines show Epanechnikov kernel density estimates. Note that in all three sub-sample the blue GCCs appear more extended than the red GCC sub-population.

(OH) GCs have comparable ($r_{\rm h,med} = 3\,$pc) and the young halo (YH) GCs have larger median sizes ($r_{\rm h,med} = 5.4\,$pc) than blue GCCs in our sample dwarf galaxies.

Comparisson with theoretical predictions for dynamical evolution

Another way to look at the cluster size distribution is in the $r_{\rm h}$ versus cluster mass plane (Fig. 3.8) which is often used to compare these observable quantities with their theoretically predicted values for clusters whose "survivability" depends on the interplay between various external and internal dissolution mechanisms.

Few theoretical studies suggest a very specific description of the cluster dynamical evolution in the $r_{\rm h}$ vs cluster mass plane. Those incorporate internal processes like mass-loss due to stellar evolution, two-body relaxation, core collapse and re-expansion due to two-body relaxation gas expulsion and external shocks from the host tidal field and encounters with giant molecular clouds (GMCs). On one side the approach of predicting the cluster dissolution (survival) assumes that the dissolution time $t_{\rm diss}$ mainly depends on cluster half-light radius and therefore scales with its relaxation time t_{rh} (e.g. Fall & Rees 1977; Gnedin & Ostriker 1997; Fall & Zhang 2001; McLaughlin & Fall 2008). However, it has been shown that one of the most significant factors of the cluster dynamical evolution over Hubble time which should be taken into account is the influence of the external tidal field (e.g. Vesperini 2000; Baumgardt & Makino 2003), and also encounters with GMCs (Gieles et al. 2006; Lamers & Gieles 2006). In particular, it was recently shown that cluster dissolution is virtually independent of cluster $r_{\rm h}$ (Gieles & Baumgardt 2008). Vesperini (2000) has shown interestingly that GCs are actually more efficiently destroyed in lower mass galaxies (10% of the initial clusters survived) than in giants (90%), opposite of what one would expect considering the strength of the host potential and the presence of disk/bulge shocking in massive galaxies. In their models, this is explained due to the transition from tidal shocking dominant in massive galaxies to dynamical friction which is very effective in lower-mass systems. Another interesting aspect of the cluster dynamical evolution, which has not been explicitly shown yet for the observable quantities ($r_{\rm h}$, cluster mass) although suggested (by e.g. Hénon 1965; Goodman 1984; Gieles & Baumgardt 2008), is the re-expansion due to two-body relaxation of a self-gravitating cluster (in weak potential and/or remote halo regions of the host galaxy) (Baumgardt & Gieles 2008 priv. com., see below). However, testing any of the above theoretical predictions and arguing in favor of one ore another is far beyond the scope of this study. Instead, in the following we will simply contrast our observations with the above mentioned predictions on clusters survivability.

In Figure 3.8 we show the distribution of GCCs in all studied dwarfs in our sample and Galactic and MCs GCs. To convert from cluster luminosities to cluster masses we adopt the mean $M/L_V = 1.8$ derived for the old LMC clusters in McLaughlin & van der Marel (2005), which are shown for comparison in the same panel in Figure 3.8 as that of the dIrrs bGCs. The half-light radius estimates and cluster masses for MCs and Galactic clusters were taken from McLaughlin & van der Marel (2005), where available, and from Harris (1996) for the remainder. The distribution of the GCs in all studied dwarfs shows that their dynamical evolution has been mainly governed by internal cluster processes (two-body relaxation, stellar evolution) rather external tidal or disk shocks. It is worth mentioning that the larger

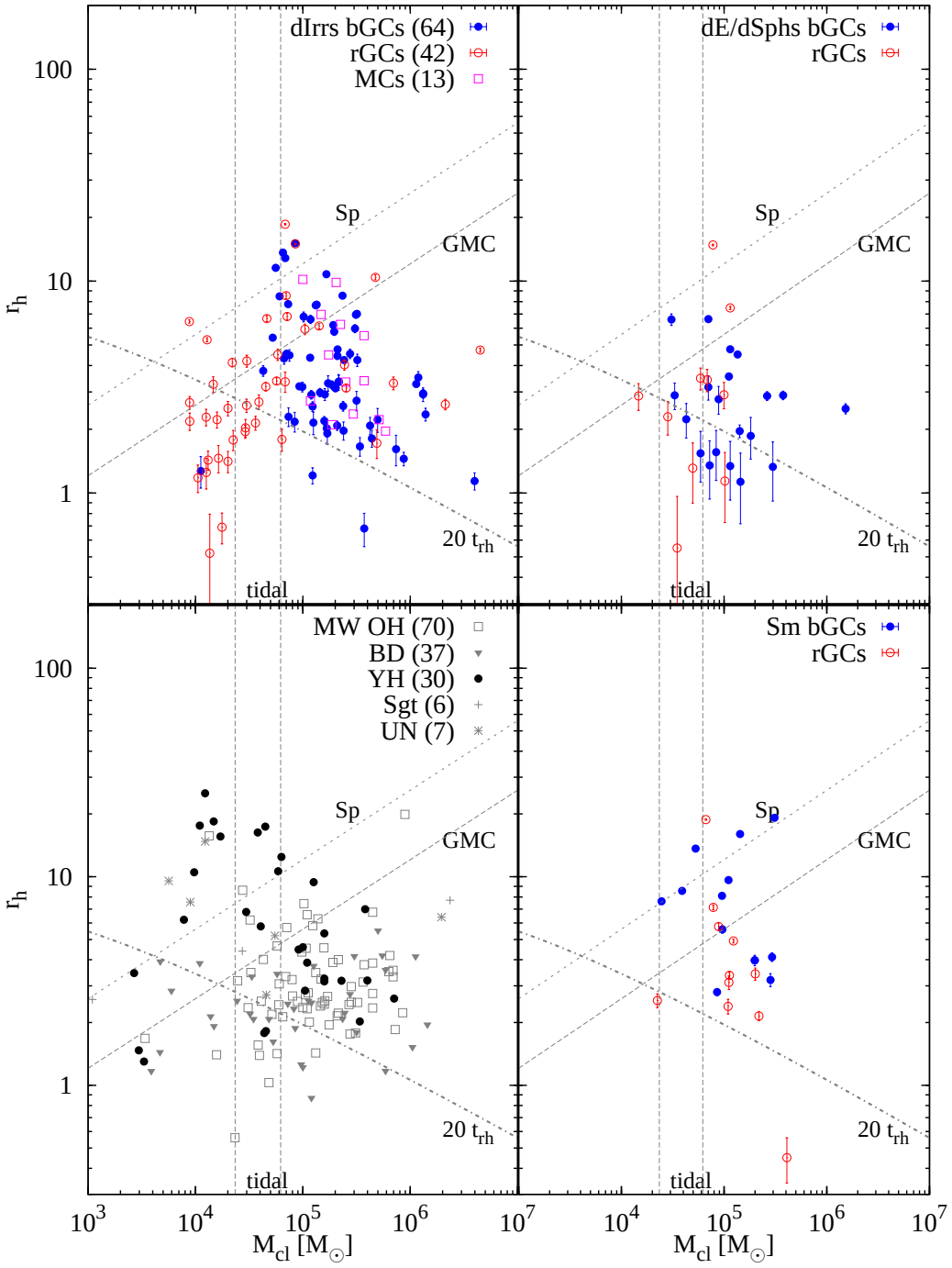

Figure 3.8: Half-light radius versus cluster mass for GCs in low-mass galaxies. In the panels are show bGCCs and rGCCs (filled and open circles), old Magellanic Clouds GCs (open squares). In the lower left panel are shown the Galactic YH GCs (filled circles), OH and BD GCs (open squares and filled triangles), Sagittarius dwarf GCs (plus sign) and clusters with unknown classification (asterisk). With lines are shown theoretical predictions for cluster dissolution over a Hubble time due to tidal field effects for clusters at 0.8 and 0.5 kpc from the center of the host (left and right vertical lines), two-body relaxation processes (dash-dotted), GMC encounters (dashed) and spiral arm shocking (dotted) (for details see Sect. 3.3.3).

erorrbars in the dE/dSphs plot are for objects in one of the most distant galaxies in our sample - the dE UGC 7369 at 11.6 Mpc. Comparisson between left-column panels in Figure 3.8, shows that bGCCs, MC GCs, and Galactic YH GCs share very similar distributions, which suggests that those objects have experienced similar formation and/or dynamical evolution histories in the weak tidal fields of the dwarf and the halo regions of the Milky Way, respectively. In contrast, the Galactic OH and BD clusters show distributions significantly different than those for bGCs and YH GCs. This indicates that their dynamical evolution has been affected by the tidal field and disk/bulge shocking. This can be seen form Fig. 3.8 that most of the OHs and BD clusters are below the limits predicting significant dynamical mass-loss due to the mentioned effects. With lines are shown the different limits for clusters experiencing mass loss due to the effects mentioned above. With a dotted line is shown the the cluster evaporation limit due to mainly two-body relaxation (Fall & Rees 1977; Gnedin & Ostriker 1997)

$$r_{\rm h} = \left(\frac{12\,000[{\rm Myr}]}{20}\right)^{2/3} \left(\frac{0.138}{G^{1/2} m_\star \ln\left(\gamma \frac{M}{m_\star}\right)}\right)^{-2/3} M^{-1/3} \qquad (3.1)$$

for clusters surviving 12 Gyr after 20 initial relaxation times; $m_\star = 0.35 M_\odot$ is the average stellar mass in GC and $\gamma = 0.02$ from models treating clusters with mass spectrum (Giersz & Heggie 1996). Below this "survival" limit, clusters should have dissolved within a Hubble time (e.g. Fall & Zhang 2001).

The evolution of a cluster in a galactic tidal field is investigated by Baumgardt & Makino (2003). We have used their equation (7) to calculate the minimum mass of a cluster which can survive for 14 Gyr within a typical mean distance from the galaxy center ($d_{\rm proj}$) for the GCs in our sample of 0.8 kpc. The result is shown with the left vertical dashed line in Figure 3.8 and corresponds to a minimum mass of $2.34 \times 10^4 M_\odot$ ($M_V = -5.5$ mag). Clusters below this mass limit should have dissolved due to the influence of the tidal field. The right vertical line indicates the minimum cluster cluster mass $d_{\rm proj} = 0.5$ kpc. It should be noted, however, that effects due to variable tidal field and dynamical friction, the latter usually very effective within $d_{\rm proj}$, are not taken into account. Interestingly, as mentioned above Vesperini (2000) showed that low-mass galaxies destroy the majority of their initial clusters mainly due to dynamical friction which is the dominant factor in dwarf galaxies.

Limits for mass-loss due to spiral arms shocking (dashed line) and GMC encounters (dash-dotted line) in Fig. 3.8 were taken from Lamers & Gieles (2006). We note however, that the derivation of those relations assumed solar neighborhood values. Nevertheless, it is seen from Figure 3.8 that GCCs in low-mass galaxies are not significantly affected by GMC encounters and spiral arm shocking.

As mentioned above, an interesting idea stems from the cluster re-expansion which can occur after core collapse. The basic relations shown in eqs.(3.2) for the $r_{\rm h}$ and cluster mass evolution are obtained by Hénon (1965); Goodman (1984); Spitzer (1987). From

$$M(t) = M_0 \left(\frac{t}{t_0}\right)^{-\nu} \quad \text{and} \quad r_{\rm h}(t) = r_{\rm h_0} \left(\frac{t}{t_0}\right)^{\frac{2+\nu}{3}} \qquad (3.2)$$

where M_0 and $r_{\rm h_0}$ the half-light radius and cluster mass at the time of core collapse t_0 and $\nu = 0.05 - 0.1$ (Baumgardt et al. 2002) is the dynamical mass-loss factor, one easily obtains

$$r_{\rm h} = r_{\rm h0} \left(\frac{M}{M_0} \right)^{-\frac{2+\nu}{3\nu}} \tag{3.3}$$

Since core collapse happens for several initial cluster relaxation times ($t_0 = n_{\rm rh} t_{{\rm rh},i}$, Gieles & Baumgardt 2008) then

$$r_{\rm h0} = (t_0)^{2/3} \left(\frac{0.138}{G^{1/2} m_\star \ln\left(\gamma \frac{M_0}{m_\star}\right)} \right)^{-2/3} M_0^{-1/3} \tag{3.4}$$

and combining eqs. (3.3) and (3.4)

$$r_{\rm h} = (t_0)^{2/3} \left(\frac{0.138}{G^{1/2} m_\star \ln\left(\gamma \frac{M_0}{m_\star}\right)} \right)^{-2/3} M_0^{-1/3} \left(\frac{M}{M_0} \right)^{-\frac{2+\nu}{3\nu}} \tag{3.5}$$

then if $M_0 = M$ (i.e. no dynamical mass-loss) at $t_0 = t = 12\,000$ Myr (Hubble time), and $n_{\rm rh} = 20$ the equation brings down to the same expression as eq. (3.1).

$$r_{\rm h} = \left(\frac{12\,000\,[{\rm Myr}]}{20} \right)^{2/3} \left(\frac{0.138}{G^{1/2} m_\star \ln\left(\gamma \frac{M}{m_\star}\right)} \right)^{-2/3} M^{-1/3} \tag{3.6}$$

In other words, clusters which starts below the currently observed relation will expand after 20 relaxation times with an increase more pronounced in low-mass clusters. However, all this requires to be shown by numerical modeling.

Ellipticities

The difference between bGCCs in dIrrs and those of the various Galactic subpopulations is also found when clusters ellipticities are compared. In Figure 3.9 we show the ellipticity distribution of GCCs in our sample dIrrs and in the Magellanic Clouds for which we used data from Frenk & Fall (1982); Kontizas et al. (1989, 1990). The non-parametric kernel density estimate identifies peaked distributions with values $\epsilon \simeq 0.1$ for both samples. This is a markedly different ellipticity distribution than that of Galactic GCs that is biased towards lower ellipticity values.

Fall & Frenk (1985) showed for a self-gravitating clusters that for $\sim 5 \times t_{\rm rh}$ the ϵ decreases by a factor of two and reaches an asymptotic value of $\epsilon = 0.1$, corresponding to the observed mean ellipticity of our bGCCs in dIrr galaxies. This implies that our sample of bGCCs as well as the MC old GCs evolved dynamically in conditions similar to isolation (i.e. mainly affected by internal than external for the cluster processes). This additionally supports the same conclusion obtained in the previous section based on cluster masses and $r_{\rm h}$.

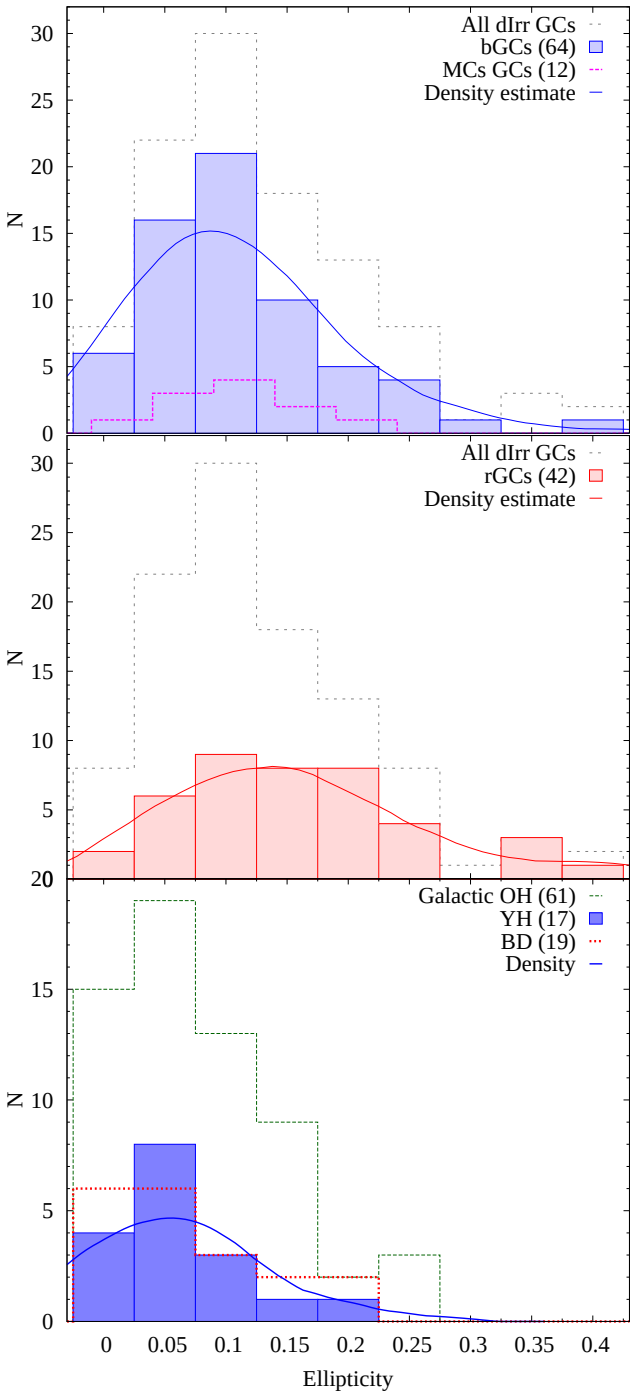

Figure 3.9: Ellipticity (ϵ) distributions of GCs in dwarf irregular galaxies. The top panel shows that bGCs in our sample dIrrs and old LMC GCs are similarly flattened. The even broader ϵ distribution for the rGCs shows that the majority are likely background contaminants. The bottom panel shows the ϵ distribution for the Galactic GC subpopulations.

3.4 Discussion

3.4.1 Specific frequencies

The globular cluster specific frequency, or the number of GCs in a galaxy per unit $M_V = -15$ mag, was introduced by Harris & van den Bergh (1981) as:

$$S_N = N_{\rm GC} \times 10^{0.4(M_V+15)} \tag{3.7}$$

to compare the formation efficiency of globular clusters per unit galaxy luminosity of different galaxies. Here we compute the S_N values for dIrrs using the number of bGCCs, the total number bGCCs+rGCCs and their total V-band magnitudes derived in Sect. 3.3.1. The total number of GCCs for the two dIrr galaxies NGC 784 and ESO 154-23 extending beyond the ACS field of view was corrected for the spatial incompleteness in Georgiev et al. (2008a). The results are shown in the upper panel of Figure 3.10. We find a strong trend of increasing S_N values with decreasing host luminosity for dIrrs. Because of their small sample size the trends, previously observed (see below), for dEs/dSph and Sm galaxies are inconclusive from our data alone.

In the bottom panel of Figure 3.10 we compare S_N values of our sample dwarfs with those of early-type giant and dwarf elliptical galaxies (data from Miller & Lotz 2007; Peng et al. 2008). All S_N values represent their present day values. Passive evolutionary fading of the integrated galaxy light will increase the S_N values by a factor of 2 to 16 for dIrrs (Georgiev et al. 2008a). The arrow indicates the change in S_N if a galaxy passively fades due to stellar evolution by $\Delta M_V = 1.5$ mag, which corresponds to the evolutionary fading from 3 to 14 Gyr.

The main observation is that the increase of S_N values seems to hold irrespective of galaxy morphological type, which was also observed in previous studies of early-type (Miller et al. 1998; Forbes 2005; Strader et al. 2006; Sharina et al. 2005; Miller & Lotz 2007; Puzia & Sharina 2008; Peng et al. 2008) and late-type dwarfs (Seth et al. 2004; Olsen et al. 2004; Georgiev et al. 2006, 2008a). It was suggested that the observed trends could be a result of mass loss due to galactic winds causing strong mass-loss (e.g. Harris et al. 1998; Forbes 2005; Bekki et al. 2006) and/or in addition to that an enhanced and very efficient GC formation due to "cold" gas accretion flows (Forbes 2005). Recently, Peng et al. (2008) investigated also the idea that the S_N behavior could be explained if the variation of the $M/L-$ratio of the galaxy is taken into account. Others suggested that the S_N behavior can be solved if the mass in GCs is directly proportional to the total gas mass supply, i.e. constant GC formation efficiency (Blakeslee 1997; Kavelaars 1999; McLaughlin 1999; Kravtsov & Gnedin 2005, see also Sect. 3.4.2). In the following we will discuss the observed trends in the GC S_N value in the light of the accretion scenario.

Given equation (3.7) and assuming $N_{\rm GC} = 1$ enables us to define a lower boundary to the S_N vs. M_V trend which is of the form:

$$\log(S_N) = 6 + 0.4 \times M_V \text{ or } \log(S_N) = 7.932 - \log(L). \tag{3.8}$$

In other words, this relation can be understood as the minimum GC formation efficiency (GCFE), i.e. to have formed at least one GC and survived a Hubble time, per unit galaxy luminosity. Interestingly, this lower limit (the lower dashed line in

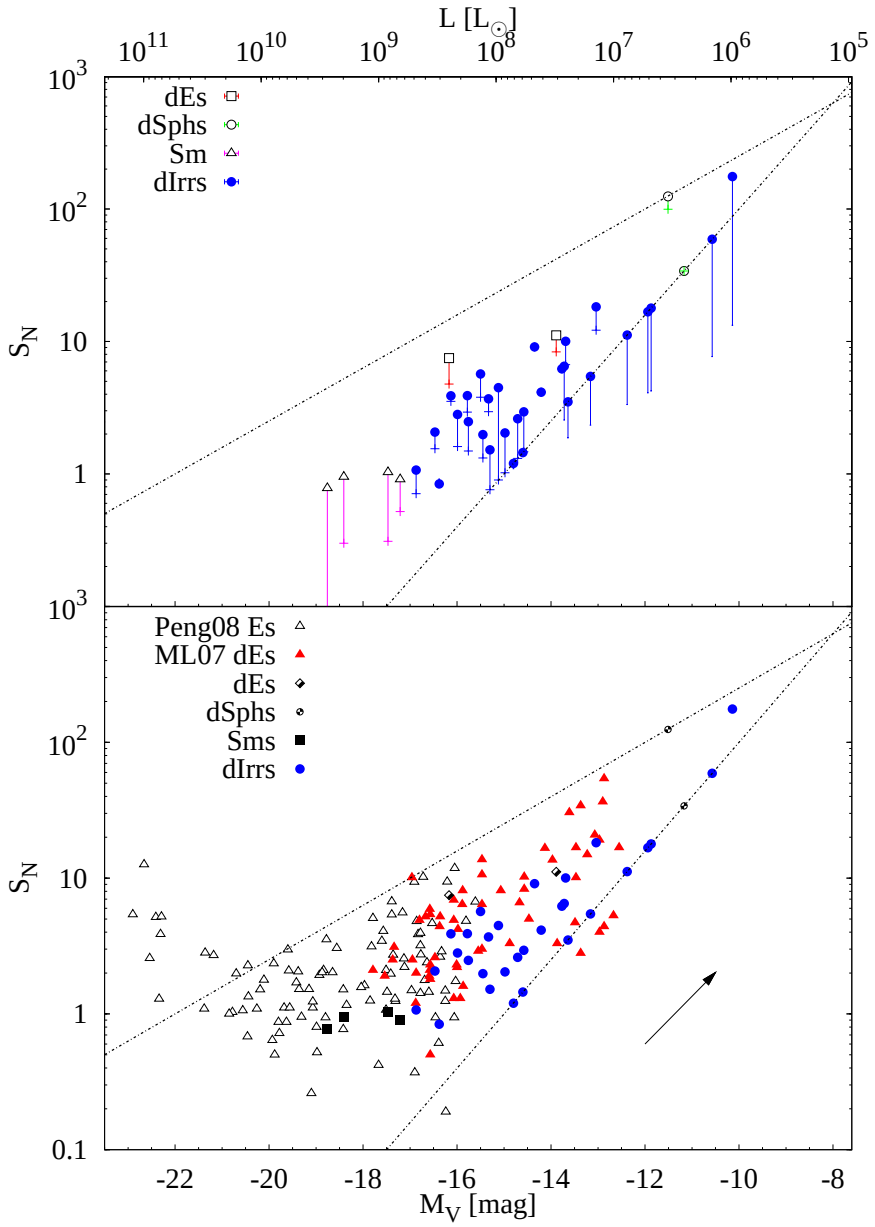

Figure 3.10: *Top panel*: Specific frequencies (S_N) versus absolute galaxy magnitude (M_V) for the dwarfs in our sample. Symbols are the (bGCC+rGCC) estimates of S_N, while plus sign denotes is the S_N estimated from the bGCC population only. *Bottom panel*: Comparison between the specific frequencies of early-type (dEs and Es) galaxies (Miller & Lotz 2007; Peng et al. 2008) and the dwarfs in our sample. The S_N values represent their present day values. The arrow indicates the evolution of the S_N value given a passive evolutionary fading of the host. In both panels the upper log linear relation is the maximum S_N at given luminosity defined from the galaxies in the bottom panel. The lower relation is defined by Equation 3.8 assuming that a galaxy hosts one GC (see Sect. 3.4.1).

Figure 3.10) seems to bracket the S_N-value galaxies at a given mass in our sample very well.

Looking at Fig. 3.10 there also seems to be an apparent maximum S_N value at a given galaxy luminosity. Such an upper boundary, if real, can be understood as the maximum number of clusters per unit galaxy luminosity of the form:

$$\log(S_N) = 4.4 + 0.2 \times M_V = 5.366 - 0.5 \times \log(L) \tag{3.9}$$

and from eqs. (3.7) and (3.9) we can derive the $N_{\rm GC,max}$

$$N_{max} = 10^{-0.2(M_V+8)} = 2.72 \times 10^{-3} (L/L_\odot)^{0.5}. \tag{3.10}$$

With the upper dashed line in Fig. 3.10 we indicate this limit. Interestingly, this will imply that an object with $M_V = -8$ mag, i.e. $1.36 \times 10^5 L_\odot$, can have one GC, i.e. an $S_N = 631$, which is below the relation. In other words, a typical GC can be thought of as a "galaxy" that own one GC (itself). For example ω Cen, which has $M_V = -10.3$ mag ($L = 1.13 \times 10^6 L_\odot$) will have a specific frequency of $S_N = 76$, which is below the upper relation and right on top of the lower limit in Fig. 3.10. Also an interesting example is the Milky Way Galaxy with $M_V = -20.5$ mag and $S_N = 0.9$, which is below the upper S_N bound.

The behavior of the GC specific frequency could be understood as due to GCs forming proportionally to the galaxy luminosity according to the above mentioned relation and the upturn of the S_N value in the high-mass regime can be understood due to dissipationless accretion of high-S_N dwarfs which contributes mainly to the GC system rather than to the total galaxy luminosity, i.e. leading to an increase of the S_N. Thus assuming that galaxies form GCs according to the relation above and using equations (3.9) and (3.10) we can estimate what would be the total number of accreted GCs so that a galaxy with $M_{V_f} = M_{V,\rm max} = -22.5$ mag ($L = 0.86 \times 10^{11} L_\odot$) will increase its S_N from an initial value of $S_{N_i} = 0.7$ (at the relation) to the final $S_{N_f} = 5$ (the median value of the galaxies at $M_V = -22.5$ mag in Fig. 3.10):

$$N_{\rm acc} = N_{\rm tot} - N_{\rm max} \quad = \tag{3.11}$$

$$= S_{N_f} \times 10^{-0.4(M_{V_f}+15)} - 10^{-0.2(M_{V,\rm max}+8)} \tag{3.12}$$

hence $N_{\rm acc} = 4000$. Therefore, we can calculate how many galaxies ($N_{\rm G}$) and with what luminosities $M_{V,\rm max}$ having the maximum "allowed" specific frequency ($S_{N,\rm max} = N_{\rm max} \times 10^{0.4(M_{V,\rm max}+15)}$) are required to merge dissipationless ("dry" merger) to increase the observed specific frequency from S_{N_i} to S_{N_f} of the merger product, i.e.:

$$S_{N_f} = S_{N_i} + N_G \times S_{N,\rm max} \quad = \tag{3.13}$$

$$= S_{N_i} + N_G \times 10^{0.2(M_{V,\rm max}-22)} \quad = \tag{3.14}$$

$$= S_{N_i} + N_G \times 2.23 \times 10^{-5} (L/L_\odot)^{-0.5} \tag{3.15}$$

. Thus for the above example we obtain that a merger of a maximum of two galaxies ($N_G = 2$) with $S_{N,max} = 2$, i.e. $M_{V,max} = 5 \times \lg(S_{N,max}) - 22 = -20.5$ mag, can lead to an increase from 0.7 to 5 in its GC specific frequency. Alternatively, one can calculate a different number and mass fraction in merging galaxies to obtain the

same final galaxy. Following the same reasoning would mean that the Milky Way accreted few galaxies in order to be below the upper S_N bound.

The most interesting question is why such an upper bound (if real) of the maximum number of GCs, either formed *in situ* or later accreted, per unit luminosity of the host exists and what is driving the mechanisms of GC formation and dissolution as a function of the galaxy magnitude such that the observed relations? And why has the observed slope the value we assumed or is it steeper? The actual slope value can be tested via the probability of a galaxy at a given mass to experience a major merger or accretion event. Perhaps a reasonable approximation for the lower value of the slope would be a relation bordering the maximum S_N values of the dwarf galaxies. Such low-mass dwarfs are very unlikely to experience a merger/accretion event with a galaxy with the same or smaller mass. If the slope is steeper then more galaxies will fall above the suggested relation, thus "allowing" more mereger/accretion events for brighter (more massive) galaxies.

In general, any processes (internal or external for the galaxy) that can lead to a decrease of the galaxy luminosity can lead to an increase of its S_N without requiring accretion. Such processes are ram pressure stripping of the stellar and gaseous component (via galaxy-galaxy or galaxy-dense intracluster interaction, e.g. Mori & Burkert 2000; Brüggen & De Lucia 2008) which would lead to suppression of further starformation in a galaxy. Such mechanisms can be increasingly effective for low-mass, shallow-potential galaxies.

3.4.2 Specific mass in globular clusters

The advantage of using masses instead of luminosities is that it allows to compare between galaxies with different present day star formation which boosts their integrated light, i.e. actively star forming galaxies (spirals, Irrs) and galaxies lacking young stellar population (Es). Zepf & Ashman (1993) introduced the number of clusters per $10^9 M_\odot$, i.e. $T = N_{\rm GC}/(M_{\rm G\star}/10^9 M_\odot)$.

Perhaps the GC formation efficiency in a galaxy would be better understood in terms of the total mass of the galaxy including the available reservoir out of which field stars and star clusters are forming such as the HI mass of the host. Or in other words, the GCs formed in proportion to the total available gas supply (Blakeslee 1997; Kavelaars 1999). This will also imply that the number of or the total mass in GCs normalized to the total stellar plus gas mass, the GC formation efficiency (ϵ) introduced by McLaughlin (1999), must be a constant value. Indeed, McLaughlin (1999) showed for the case of three bright and cluster dominant (BCD) galaxies that this mass ratio is constant ($\epsilon = 0.0026$) once the hot X-ray emitting gas is taken into account and alleviates the S_N problem. In the case of such BCD galaxies, where the HI mass is extremely small or unmeasurable, the mass of hot X-ray gas is important. In the following we have considered only HI and stellar masses, which is an acceptable assumption for low-mass galaxies. Thus in the bottom panel in Figure 3.11 we show the specific mass of the GCS per $10^3 M_\odot$ of the total, HI ($M_{\rm HI}$) plus stellar ($M_\star$), mass of the galaxy:

$$S_M = 10^3 \times M_{\rm GCS}/(M_\star + M_{\rm HI}) \tag{3.16}$$

which is 10^3 times the McLaughlin ϵ parameter for the GC formation efficiency. The

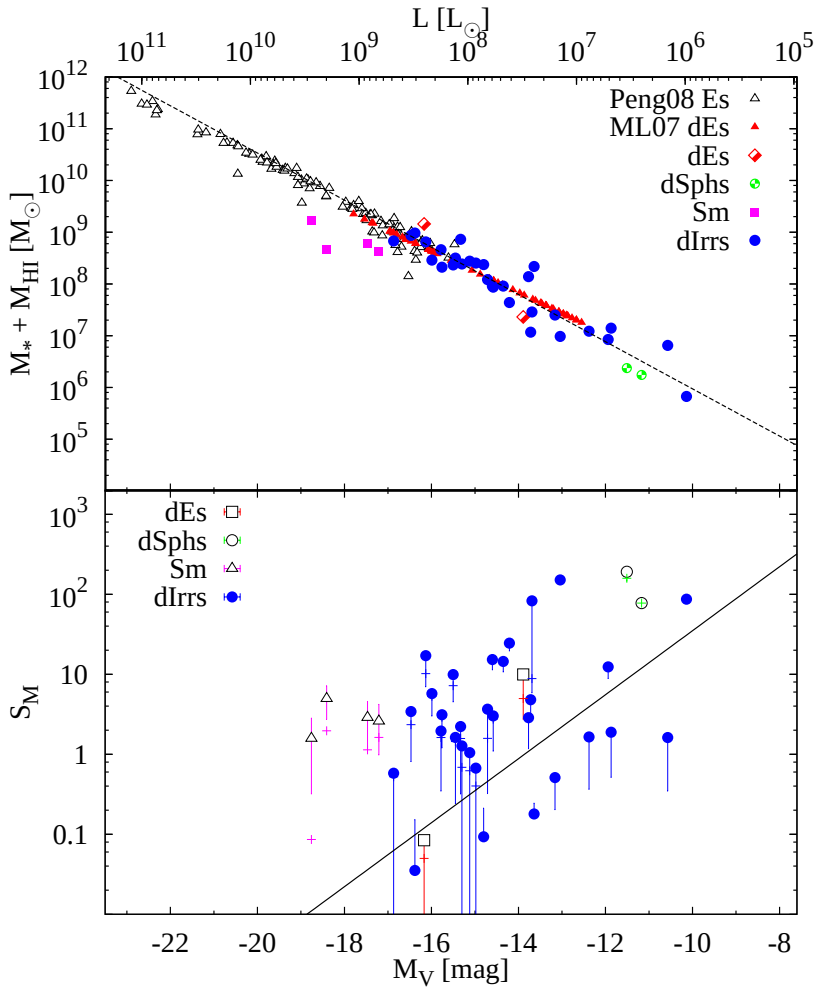

Figure 3.11: **Top:** Stellar plus HI mass versus absolute galaxy magnitude (M_V) for the dwarfs in our sample compared with early-type galaxies from the literature (Miller & Lotz 2007; Peng et al. 2008). The dashed line is the least-square fit to the data. **Bottom:** the specific total mass (S_M) of the GCs in our sample galaxies versus M_V. The solid line indicates a relation for a galaxy which formed GCs of which at least one (with mass $M_{\rm GCS} = 1$ [10^4 M$_\odot$] has survived for a Hubble time (see eq. 3.18).

GC number normalized to the same total mass ($S_{N,M}$) presented here is:

$$S_{N,\rm M} = 10^7 \times N_{\rm GC}/(M_\star + M_{\rm HI}) \tag{3.17}$$

where $M_{\rm GCS}$ is the total mass of the GCS and $M_{\rm HI}$ is the HI mass of the galaxy. The here defined $S_{N,\rm M}$ is becomes the $10^2\times$T-value (Zepf & Ashman 1993) for galaxies lacking $M_{\rm HI}$ such as ellipticals. To derive $M_{\rm GCS}$ we have converted the cluster absolute magnitudes to masses assuming $M/L_V = 1.8$ as explained in Sect. 3.3.3. The $M_{\rm HI}$ was calculated from the HI magnitudes in the LEDA database following Roberts & Haynes (1994). To convert from luminosity to galaxy mass we used the relation between the galaxy $B-V$ color and its $M/L-$ratio

$$\lg(M/L) = -0.942 + 1.737 \times (B-V).$$

The top panel in Figure 3.11 shows a linear relation between galaxy luminosity and galaxy massIt interestingly shows that the linear relation holds for a large dynamical

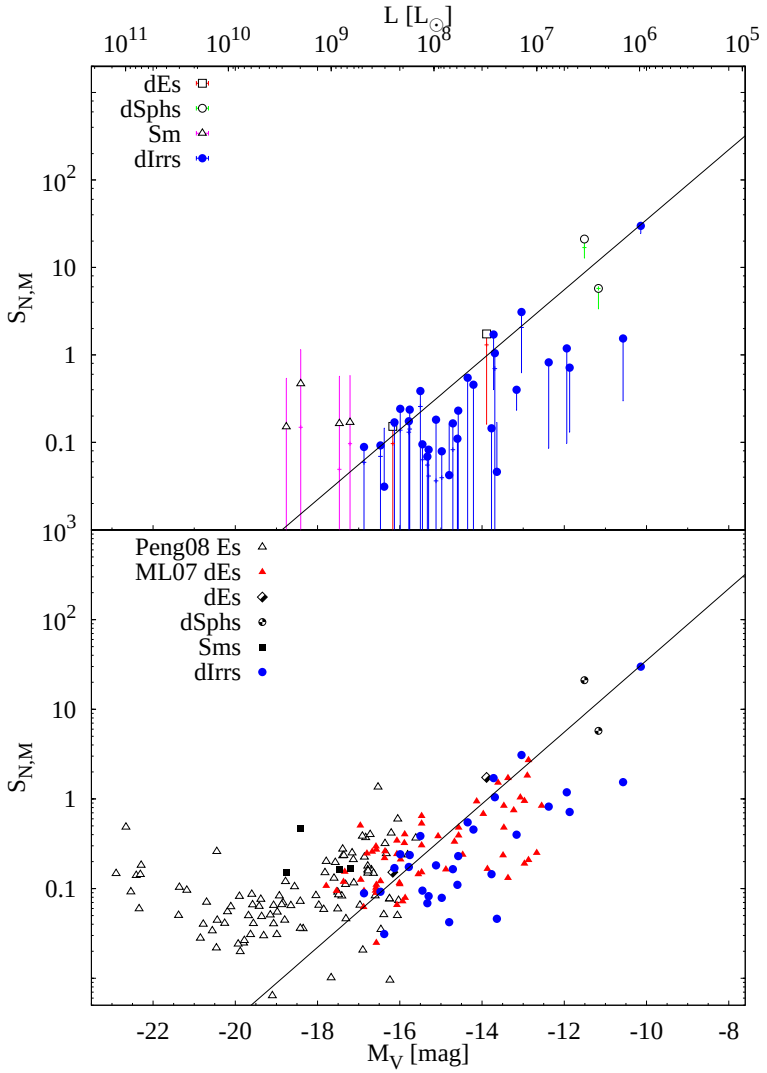

Figure 3.12: Specific cluster numbers $S_{N,M}$ (T-value) normalized to the total galaxy mass (stellar plus HI) as a function of galaxy luminosity. In the top panel are shown the dwarfs in our sample, while in the bottom panel are compared with early-type galaxies from the literature (Miller & Lotz 2007; Peng et al. 2008). The solid line indicates a relation for a galaxy which formed GCs of which at least one ($N_{\rm GC} = 1$) has survived for a Hubble time (see eq. 3.18).

range in galaxy masses and gas content (from HI rich to HI poor galaxies as the late-type dIrrs and early-type ellipticals). We note however, that the two spirals seem to deviate from the relation. This might be due to either wrong estimates of the M/L or large measurement errors. The low-mass dIrrs in our sample are faint but gas rich (from few to few tens $10^7 M_{\rm HI}$), while the ellipticals are bright but completely lacking HI (or at least it is very small in mass fraction). We note that we have used the Miller & Lotz (2007) magnitudes and $M/L = 2$ to obtain masses from the galaxy magnitudes listed in their table. The masses they report are calculated for $M/L = 5$ and they were offset from the relation defined by our and Peng et al. (2008) data sets. We have used the masses of Peng et al. (2008) which are calculated from galaxy color and are listed in their tables.

In Figure 3.12 is shown the mass normalized specific frequency $S_{N,M}$ (the $T-$value for HI deficient galaxies) for the dwarf galaxies in our sample (upper panel) and

comparison with early-type galaxies in the bottom panel. Again, the data for the ellipticals was collected from Miller & Lotz (2007); Peng et al. (2008). With crosses are indicated the respective value determined from the bGCs alone for the galaxies in our sample.

From equation (3.16) one can derive that

$$\log(S_M) = 3 - 0.4 \times (M_\odot - M_V) - \log(M/L) + \log(M_{\rm GCS}) \tag{3.18}$$

and if $M_{\rm GCS} = 1\ [10^4\,{\rm M}_\odot]$ and $M/L = 3$ we obtain the realtion shown with solid line in Figure 3.11 bottom panel.

Analogously from equation (3.17) one can also obtain that

$$\log(S_{N,M}) = 7 - 0.4 \times (M_\odot - M_V) - \log(M/L) + \log(N). \tag{3.19}$$

Then if $N_{\rm GC} = 1$ and $M/L = 3$ we obtain again a relation which is shown with solid line in Figure 3.12.

In other words the relations from the above two equations represent the lower GC formation efficiency or GC survival limit, i.e. when a galaxy managed to form GCs of which at least one ($N_{\rm GC} = 1$ with mass $M_{\rm GCS} = 1\ [10^4\,{\rm M}_\odot]$) survived dissolution processes for a Hubble time.

Here we have shown that the mass and the number of GCs inversly scales with the total galaxy mass (assuming that all of the baryon mass of a galaxy is in stars and HI gas). This interestng behavior have to be explained by processes involved in galaxy evolution and GC formation.

Table 3.1: General properties of all studied dwarf galaxies.

ID	R.A. (J2000.0)	Decl. (J2000.0)	Morph. T	Type[a]	D[b] Mpc	$m-M$[b] mag	M_V mag	$(V-I)_0$ mag	M_{HI} $10^7 M_\odot$
(1)	(2)	(3)	(4)	(5)	(6)	(7)	(8)	(9)	(10)
— Cen A/M83 complex —									
Cen N	13:48:09.2	−47:33:54.0	?	dSph	3.77	27.88	-11.15	1.24	–
ESO 059-01	07:31:19.3	−68:11:10	10	IB	4.57	28.30	-14.60	0.78	8.26
ESO 137-18	16:20:59.3	−60:29:15	5.0	SAsc	6.4	29.03	-17.21	0.79	34.14
ESO 215-09	10:57:30.2	−48:10:44	10	I	5.25	28.60	-14.08	0.80	64.21
ESO 223-09	15:01:08.5	−48:17:33	9.7	IAB	6.49	29.06	-16.47	0.88	63.89
ESO 269-58	13:10:32.9	−46:59:27	9.4	I	3.8	27.90	-15.78	0.98	2.31
ESO 269-66	13:13:09.2	−44:53:24	-5	dE,N	3.82	27.91	-13.89	1.00	–
ESO 274-01	15:14:13.5	−46:48:45	6.6	Scd	3.09	27.45	-17.47[a]	1.03[a]	20.18
ESO 320-14	11:37:53.4	−39:13:14	10	I	6.08	28.92	-13.67	0.80	2.25
ESO 381-18	12:44:42.7	−35:58:00	9	I	5.32	28.63	-13.39	0.72	2.71
ESO 381-20	12:46:00.4	−33:50:17	9.8	IBm	5.44	28.68	-14.80	0.63	15.71
ESO 384-16	13:57:01.6	−35:20:02	-5	dSph/Im	4.53	28.28	-13.72	0.87	–
ESO 443-09	12:54:53.6	−28:20:27	10	Im	5.97	28.88	-12.19	0.74	1.44
ESO 444-78	13:36:30.8	−29:14:11	9.9	Im	5.25	28.60	-13.48	0.86	2.06
HPSS 1348-37	13:48:33.9	−37:58:03	10	I	5.75	28.78	-10.80	0.79	0.78
HPSS 1351-47	13:51:22.0	−47:00:00	10	I	5.73	28.79	-11.55	0.68	2.69
IC 4247	13:26:44.4	−30:21:45	1.6	Sab	4.97	28.48	-14.69	0.66	3.45
IKN	10:08:05.9	+68:23:57	-3	dSph	3.75	27.87	-11.51[c]	0.7[c]	–
KK 189	13:12:45.0	−41:49:55	-5	dE	4.42	28.23	-11.99	0.92	–
KK 196	13:21:47.1	−45:03:48	9.8	IBm	3.98	28.00	-10.72	0.71	–
KK 197	13:22:01.8	−42:32:08	10	Im	3.87	27.94	-13.04	1.16	0.17
KKS 55	13:22:12.4	−42:43:51	-3	dSph	3.94	27.98	-11.17	1.22	–
KKS 57	13:41:38.1	+42:34:55	-3	I	3.93	27.97	-10.73	1.08	–
NGC 5237	13:37:38.9	−42:50:51	1.4	dSph/I	3.4	27.66	-15.45	0.91	3.10
— Sculptor group —									
ESO 349-31	00:08:13.3	−34:34:42	10	IB	3.21	27.53	-11.87	0.66	1.34
NGC 247	00:47:06.1	−20:39:04	6.7	SABd	3.65	27.81	-18.76[a]	0.85[a]	37.60
— Mafei 1 & 2 —									
KKH 6	01:34:51.6	+52:05:30	10	I	3.73	27.86	-12.66	0.80	1.34
— IC 342 group —									
KKH 37	06:47:46.9	+80:07:26	10	I	3.39	27.65	-12.07	0.80	0.48
UGCA 86	03:59:48.3	+67:08:18.6	9.9	Im	2.96	27.36	-16.13[d]	0.80[d]	48.25
UGCA 92	04:32:04.9	+63:36:49.0	10	Im	3.01	27.39	-14.71	0.51	7.62
— NGC 2903 group —									
D 564-08	09:19:30.0	+21:36:11.7	10	I	8.67	29.69	-12.76	1.00	1.93
D 565-06	09:19:29.4	+21:36:12	10	I	9.08	29.79	-12.88	0.95	0.54
— CVn I cloud —									
NGC 4068	12:04:02.4	+52:35:19	9.9	Im	4.31	28.17	-15.25	0.63	11.22
NGC 4163	12:12:08.9	+36:10:10	9.9	Im	2.96	27.36	-14.21	0.80	1.42
UGC 8215	13:08:03.6	+46:49:41	9.9	Im	4.55	28.29	-12.51	0.82	1.84
UGC 8638	13:39:19.4	+24:46:33	9.9	Im	4.27	28.15	-13.69	0.74	1.17
— Field? —									
D 634-03	09:08:53.5	+14:34:55	10	I	9.46	29.90	-11.94	0.92	0.49
DDO 52	08:28:28.5	+41:51:24	10	I	10.28	30.06	-14.98	0.80	19.99
ESO 121-20	06:15:54.5	−57:43:35	10	I	6.05	28.91	-13.64	0.68	11.49
HPSS 1247-77	12:47:32.6	−77:35:01	10	Im	3.16	27.50	-12.86	0.20	1.05
HS 117	10:21:25.2	+71:06:58	10	I	3.96	27.99	-11.31	0.91	–
IC 4662	17:47:06.3	−64:38:25	9.7	IBm	2.44	26.94	-15.58	0.66	12.58
KK 182	13:05:02.9	−40:04:58	10	I	5.78	28.81	-13.10	0.63	4.45
KK 230	14:07:10.7	+35:03:37	10	I	1.92	26.42	-9.06	0.74	0.17
KK 246	20:03:57.4	−31:40:54	10	I	7.83	29.47	-13.77	0.83	11.92
KKH 77	12:14:11.3	+66:04:54	10	I	5.42	28.67	-14.58[a]	0.7[c]	4.67
NGC 4605	12:39:59.4	+61:36:33	4.9	SBc	5.47	28.69	-18.41[a]	0.7[c]	25.88
UGC 7369	12:19:38.8	+29:52:59	7.6	dE/dE,N?	11.6	30.32	-16.17	1.03	–
VKN	08:40:08.9	+68:26:23	-3	dSph?	3.4	–	-10.52[c]	0.7[c]	–

[a] From LEDA/NED

[b] Distance and distance modulus from Karachentsev et al. (2006, 2007)

[c] Estimated from the total B magnitudes assuming average $B-V=0.45$ and $V-I=0.7$ mag (see Sect.3.3.1).

Chapter 4

Outlook and future directions: Nuclear Globular Clusters in Dwarf Galaxies

Contents

4.1 Bright and nuclear GCs in dIrrs

An interesting finding from the analysis of our HST/ACS data (Georgiev et al. 2008a,b, Ch. 3) is that we not only observe GCs in sub-luminous dIrrs, but these dIrrs also managed to form bright and nuclear GCs (nGCs, $M_V \sim -8$ to -11 mag). Currently, a comparison between the integrated photometric properties of nGCs and structural parameters and those with extended horizontal branch Galactic GCs is being performed (Georgiev et al. 2008c). Preliminary results indicate that nGCs have a lot in common with Galactic EHB-GCs when looking at the distribution of their colors, magnitudes and structural parameters. Their colors are consistent with old ages (e.g. Sharina et al. 2005; Georgiev et al. 2008a) and they are found to populate a similar magnitude versus cluster half-light radius (M_V vs. $r_{\rm h}$) region as EHB-GCs (Fig. 4.1). This supports the idea that nGCs might be the analogs/progenitors of such EHB-GCs.

The cluster escape velocity ($v_{\rm esc}$) can be used to probe the common origin between nGCs and EHB-GCs. We have calculated the present day $v_{\rm esc}$ for Galactic GCs and plot them versus their metallicities (Fig. 4.2). It can be seen that the present-day $v_{\rm esc}$ correlates with [Fe/H], especially for EHB-GCs. Unfortunately, we do not have metallicity measurements for nGCs in our sample dIrrs to perform a direct comparison in the same parameter space. The best we can do so far with the existing data of our nGCs is to calculate their $v_{\rm esc}$ using the M_V and $r_{\rm h}$ measurements from our broadband HST/ACS study (Georgiev et al. 2008a,c, in prep.) and adopting an average $M/L = 1.8$ representative for old LMC GCs (McLaughlin & van der Marel 2005). As shown in Figure 4.2, the nGCs (open squares) coincide with Galactic EHB-GCs in this parameter space.

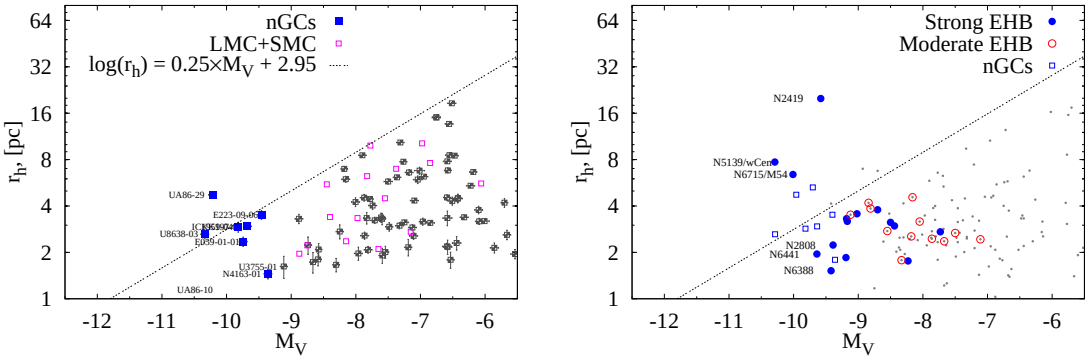

Figure 4.1: Comparison between Galactic globular clusters (GC) with extended horizontal branches (EHB-GC) and nuclear GCs (nGC) in dwarf Irregular (dIrr) galaxies (data from Georgiev et al. 2008a,b,c, in prep). The EHB-GCs and nGCs are shown with circles and squares in both panels, respectively. As can be seen, nGCs in dIrrs overlap with EHB-GCs and populate the region connecting compact and extended EHB-GCs. Besides four of the nGCs observable from Paranal (shown with labels) 21 additional bright GCs are targets for the proposed spectroscopic observations.

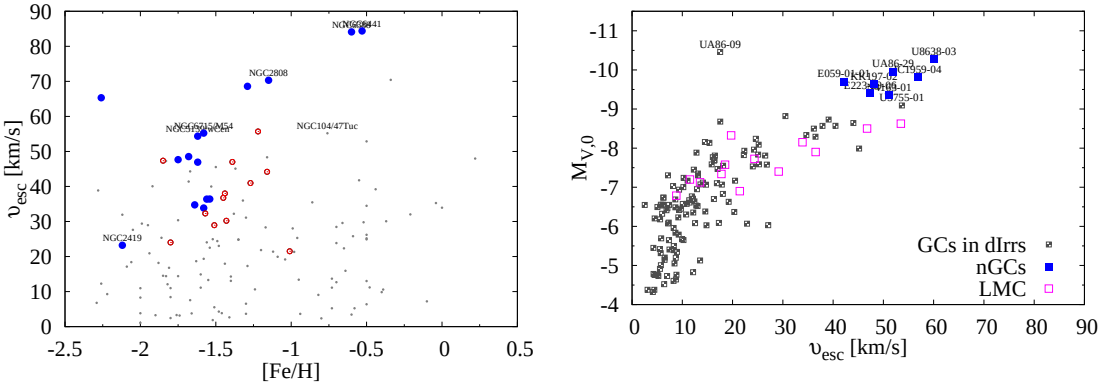

Figure 4.2: **Left:** Internal escape velocities ($\upsilon_{\rm esc}$) of Galactic GCs versus their metallicity ([Fe/H]). The observed correlation between $\upsilon_{\rm esc}$ and [Fe/H] for EHB clusters indicates that clusters with higher masses are more likely to retain stellar ejecta, thus leading to a higher degree of self-pollution. **Right:** $M_V - \upsilon_{\rm esc}$ for Galactic EHB clusters (big filled and open circles) and nGCs (open squares). As can be seen nGCs occupy a similar region as ω Cen and M 54. However, precise metallicity and mass estimates are required for a direct comparison between nGCs and EHB-GCs (to appear in Georgiev et al. 2008c).

Future spectroscopic follow-up observations will allow to perform a direct comparison in the metallicity–radius–mass parameter space.

4.2 Cluster horizontal branch morphology and mass - metallicity relation

Studies of Galactic GCs have shown that 25% of them exhibit unusually hot, extended horizontal branches (Lee et al. 2007). Those clusters are among the most massive clusters (e.g. ω Cen, M 54, NGC 2808, NGC 2419, etc.) and show an indication for the presence of multiple stellar populations as seen in their deep Hubble Space Telescope color-magnitude diagrams (e.g. Bedin et al. 2004). They also form a kinematically distinct population along with the metal-poor "Young Halo" Galactic GCs. This suggests that they might have a unique origin in the formation history of our Galaxy, being clusters which formed in the cores of massive pre-Galactic dwarf-sized building blocks and subsequently were accreted into the Galactic halo (e.g. Zinn 1993; Lee et al. 2007). Promising candidates to test the formation history of Galactic EHB-globular clusters are the bright and nuclear globular clusters (nGC) in dwarf galaxies.

Recent photometric studies of bright and nGC in dIrr galaxies indicated that they have a lot in common with Galactic EHB-GCs when looking at the distribution of their colors, magnitudes and structural parameters. Their colors are consistent with old ages (Sharina et al. 2005; Puzia & Sharina 2008; Georgiev et al. 2008a, e.g.), and are found to populate a similar M_V vs. $r_{\rm h}$ region as EHB-GCs, (see Fig. 4.1, data from Georgiev et al. 2008a, , Georgiev et al. 2008c in prep.). This supports the idea that nGCs might be the analogs/progenitors of such EHB-GCs. So far, spectroscopic analyses of GCs in dwarf galaxies are mainly performed for early-type dEs and dSphs (e.g. Strader et al. 2003; Sharina et al. 2006; Beasley et al. 2006; Puzia & Sharina 2008). Similar analyses of late-type dwarfs are very sparse (Beasley et al. 2002, : LMC GCs); (Puzia & Sharina 2008, : dIrr UGC 3755 with 4 old GCs). Therefore, a large systematic spectroscopic study of GCs in dIrrs is required.

Deriving ages and chemical compositions from integrated broadband photometry is very challenging due to the well known age–metallicity degeneracy. This degeneracy can be broken by measuring Lick indices (Worthey et al. 1994) and comparing these with single stellar population (SSP) models (e.g. Thomas et al. 2003, 2004). Constraining clusters ages, metallicities and [α/Fe] will help us to assess how similar are (n)GCs in dwarf galaxies to EHB-GCs in terms of their star-formation time scales and chemical enrichment. Further, a comparison with available Lick index measurements of nGCs and nuclei of early-type dwarfs will be useful to test the possible evolutionary connection between late- and early-type dwarfs.

It is worth mentioning that observational and theoretical studies of GCs in the LMC and our Galaxy (de Freitas Pacheco & Barbuy 1995; Beasley et al. 2002; Schiavon et al. 2004, e.g.) clearly showed the known caveat of underestimating cluster ages ($\leq$ 5 Gyr) due to the presence of hot HB stars contributing to the Balmer lines strength. Schiavon et al. (2004) demonstrated that the HB degeneracy can be lifted from the combination of Hβ and Hδ_F, making it possible to distinguish HB from age effects using integrated spectra.

Although it is well known that the horizontal branch (HB) morphology is a

function of metallicity the latter is not the sole parameter that is able to explain it, as there are Galactic GCs with identical metallicities and ages, but completely different HBs. This is the so called "second parameter problem". Recently, Recio-Blanco et al. (2006) showed that a very important parameter driving the HB morphology is the cluster mass, accounting for up to 60% of the HB variation. The line of reasoning is: the more massive the GC, the higher its escape velocity ($v_{\rm esc}$) is. The most massive GCs therefore will be more capable to retain low-velocity stellar ejecta, from which a second generation of stars might be formed (explaining GCs with multiple stellar populations). According to self-enrichment models the ejecta of massive AGB stars (e.g. Ventura & D'Antona 2008) and of fast rotating stars Decressin et al. (2007 a,b) can provide He-enriched material. These are one of the most discused explanations for the existence of very hot stars on the extreme extension of the HB.

One way to quantify and test the viability of this scenario is to look at the $v_{\rm esc}$ of the clusters. Calculating $v_{\rm esc}$ involves knowledge of the cluster's half-light radius $r_{\rm h}$ and mass $M_{\rm cl}$ ($v_{\rm esc} \propto \sqrt{M_{\rm cl}/r_{\rm h}}$). For clusters with similar masses, the one with the smaller $r_{\rm h}$ will have a higher $v_{\rm esc}$, therefore will more efficiently retain enriched material from stellar winds, hence providing an explanation for the different chemical evolution of clusters with the same mass.

The recently discovered puzzling relation between GC luminosity (mass) and its color (metallicity), i.e. the mass–metallicity relation has also been suggested to be due to self-enrichment occurring in GCs (e.g. Harris et al. 2006b; Mieske et al. 2006; Strader et al. 2006). This phenomenon can also be approached by looking at $v_{\rm esc}$, representing the cluster mass, and the cluster metallicity (Z). Our work in progress indicates that the $v_{\rm esc}-$ Z relation holds for Galactic metal-poor GCs and especially the EHB-GCs (cf. Fig. 4.2, Sect. 4.1). We aim to investigate this relation and compare $v_{\rm esc}$ and spectroscopic metallicities for nGCs in our sample dIrrs with GCs of comparable masses and metallicities in massive galaxies.

These ideas are new and thusfar observationally unexplored. We are pursuing those in our GCs in dIrrs project.

Chapter 5

Acknowledgements

Completing a PhD is trully a marathon event! And the successful end of my PhD project would not have been possible without the aid and support in the form of careful supervision, scientific and friendly discussions and the pure friendly support by every single person I have met throughout until this moment. Thank you all!

In particular, I would like to express my deep and sincere gratitude to my direct and scientific supervisors **Prof. Klaas de Boer** and **Dr. Michael Hilker** who gave me the opportunity to come from the little Bulgaria and start in the world of professional astronomy at the former Sternwarte and current "Argelander Institut für Astronomie" (AIfA) der Universität Bonn. I am extremely delighted experiencing such professionals and great persons as mentor. The wonderful multi-wavelength, deep dataset provided to me by Michael of the dwarf irregular galaxy NGC 1427A from the 8 m "European Southern Observatory – Very Large Telescope" was the best possible start for an observer as me. And I am very thankful to Klaas for his general advices on policy matters. He also very brightly corrected my English and the writing style of my thesis and papers without whose edits very few people would have "enjoyed" reading my work.

I am extremely thankful for the opportunity I have been given through the "Space Telescope Science Institute" (STScI) graduate student fellowship to work in collaboration, learn, be under the supervision and have the pleasure to meet the experienced professionals and good persons **Paul Goudfrooij** and **Thomas Puzia**. In the two years spent together at STScI I have learned from them how to master Hubble Space Telescope image reduction and analysis techniques and also benefited through discussions with other colleagues in our group for whom I am greatly thankful, namely **Rupali Chandar, Peter Pessev** and **Aparna Maybhate**.

A big thanks goes to **Prof. Pavel Kroupa** who provided me with a stimulating environment for my final year at the AIfA. His views and different approach to the pressing questions in Astrophysics always stimulate active thinking and searches for alternative and often new and innovative solutions to problems.

It is not possible to name all the colleagues who I met throughout the years at the AIfA and STScI whose useful discussions greatly improved my knowledge and my work. I am very thankful for many enlightening discussions in particular with **Holger Baumgardth, Jann Pflamm-Altenburg, Ulf Löckman, Manuel Metz** at AIfA, **Anton Koekemoer, Henry Ferguson, Eric Peng** at STScI and the countless number of friends who I met during the time spent at either instituions.

The countless dicussions with colleagues at various conferences, workshops and meetings were inseparable part of my scientiffic progress. I greatly enjoyed discussions in particular with **William and Gretchen Harris, Dean McLaughlin, Steffen Mieske, Mark Gieles, Markus Kissler-Patig, Sören Larsen, Cristiano Da Rocha** and many others.

My greatest thanks also goes to **Ole Marggraf, Oliver Cordes** and **Manuel Metz** whose prompt and kind technical support was extremely important for the successful compilation of all technical aspects throughout. I would like also to kindly thank our secretary at AIfA **Elisabeth Danne** from who I received a great help in dealing with all formalities and paper work.

I am also very thankful for the inspiration and initial support to my BSc and MSc supervisors **Prof. Georgi Ivanov, Dr. Todor Veltchev** at the Physics Department of Sofia University and **Dr. Tsvetan Georgiev** at the Insitute of Astronomy of the Bulgarian Academy of Sciences. I also thank the numerous colleagues and friends with who I had a great time in my university years.

And last, but not least, I am extremely thankful to **my family** who wholeheartedly and without reservation supported any of my personal decisions to pursue the knowledge abroad and faraway from all. For that I am enormously indebted to my **parents** and **grand parents** without whose encouragement and spiritual support I would not have come this far. But most of all I thank my **brother** who has served me as the greatest example for personality, pursuit for knowledge and ambition. His loving family, wife and lovely daughter, have been always serving me as inspiration.

I would like to also thank the financial support through grants from the "Deutsche Forschungsgemeinschaft" (DFG, German Science Foundation) Graduate Research School 787 on "Galaxy Groups as Laboratories for Baryonic and Dark Matter" and the support from a German Science Foundation Grant (DFG-Projekt BO-779/32-1). I am grateful for the award of a STScI Graduate Research Fellowship. Support for this work was provided in part by NASA through HST grant number GO-10550 from the Space Telescope Science Institute, which is operated by the Association of Universities for Research in Astronomy, Inc., under NASA contract NAS5-26555.

Bibliography

Aarseth S. J., Heggie D. C., 1998, MNRAS, 297, 794

Anders P., Bissantz N., Fritze-v. Alvensleben U., de Grijs R., 2004, MNRAS, 347, 196

Anders P., Fritze-v. Alvensleben U., 2003, A&A, 401, 1063

Ashman K. M., Zepf S. E., 1992, ApJ, 384, 50

Ashman K. M., Zepf S. E., 1998, Globular Cluster Systems. Cambridge University Press, 1998. (Cambridge astrophysics series ; 30) QB853.5 .A84 1998

Barmby P., Huchra J. P., 2001, AJ, 122, 2458

Barmby P., Huchra J. P., Brodie J. P., 2001, AJ, 121, 1482

Barmby P., McLaughlin D. E., Harris W. E., Harris G. L. H., Forbes D. A., 2007, AJ, 133, 2764

Bassino L. P., Cellone S. A., Forte J. C., Dirsch B., 2003, A&A, 399, 489

Baumgardt H., Hut P., Heggie D. C., 2002, MNRAS, 336, 1069

Baumgardt H., Kroupa P., Parmentier G., 2008, MNRAS, 384, 1231

Baumgardt H., Makino J., 2003, MNRAS, 340, 227

Beasley M. A., Baugh C. M., Forbes D. A., Sharples R. M., Frenk C. S., 2002, MNRAS, 333, 383

Beasley M. A., Hoyle F., Sharples R. M., 2002, MNRAS, 336, 168

Beasley M. A., Strader J., Brodie J. P., Cenarro A. J., Geha M., 2006, AJ, 131, 814

Bedin L. R., Piotto G., Anderson J., et al., 2004, ApJL, 605, L125

Bekki K., Forbes D. A., Beasley M. A., Couch W. J., 2002, MNRAS, 335, 1176

Bekki K., Yahagi H., Forbes D. A., 2006, ApJL, 645, L29

Bertin E., Arnouts S., 1996, A&AS, 117, 393

Blakeslee J. P., 1997, ApJL, 481, L59

Blakeslee J. P., Tonry J. L., 1996, ApJL, 465, L19

Böker T., Calzetti D., Sparks W., et al., 1999, ApJS, 124, 95

Böker T., Sarzi M., McLaughlin D. E., et al., 2004, AJ, 127, 105

Bournaud F., Jog C. J., Combes F., 2007, A&A, 476, 1179

Brodie J. P., Strader J., 2006, ARA&A, 44, 193

Brüggen M., De Lucia G., 2008, MNRAS, 383, 1336

Bruzual G., Charlot S., 2003, MNRAS, 344, 1000

Bundy K., Treu T., Ellis R. S., 2007, ApJL, 665, L5

Bureau M., Mould J. R., Staveley-Smith L., 1996, ApJ, 463, 60

Cardelli J. A., Clayton G. C., Mathis J. S., 1989, ApJ, 345, 245

Carney B. W., Harris W. E., 1998, Labhardt L., Binggeli B. (eds.), Star Clusters. Springer-Verlag, 2001, Berlin, p. 8, 2000 update

Cellone S. A., Forte J. C., 1997, AJ, 113, 1239

Chanamé J., Infante L., Reisenegger A., 2000, ApJ, 530, 96

Chandar R., Whitmore B., Lee M. G., 2004, ApJ, 611, 220

Conselice C. J., Rajgor S., Myers R., 2008, MNRAS, 446

Côté P., Marzke R. O., West M. J., 1998, ApJ, 501, 554

Côté P., West M. J., Marzke R. O., 2002, ApJ, 567, 853

Da Costa G. S., Armandroff T. E., 1990, AJ, 100, 162

de Freitas Pacheco J. A., Barbuy B., 1995, A&A, 302, 718

de Oliveira M. R., Bica E., Dottori H., 2000, MNRAS, 311, 589

de Vaucouleurs G., de Vaucouleurs A., Corwin H. G., Jr., et al., 1991, Third Reference Catalogue of Bright Galaxies. Volume 1-3, XII, 2069 pp. 7 figs.. Springer-Verlag Berlin Heidelberg New York

Decressin T., Charbonnel C., Meynet G., 2007, A&A, 475, 859

Decressin T., Meynet G., Charbonnel C., Prantzos N., Ekström S., 2007, A&A, 464, 1029

Dekel A., Silk J., 1986, ApJ, 303, 39

Di Criscienzo M., Caputo F., Marconi M., Musella I., 2006, MNRAS, 365, 1357

Dinescu D. I., Girard T. M., van Altena W. F., 1999, AJ, 117, 1792

Dirsch B., Richtler T., Geisler D., et al., 2003, AJ, 125, 1908

Djorgovski S., 1993, Physical Parameters of Galactic Globular Clusters, in Astronomical Society of the Pacific Conference Series, Vol. 50, Djorgovski S. G., Meylan G. (eds.), Structure and Dynamics of Globular Clusters, p. 373

Dolphin A. E., Walker A. R., Hodge P. W., et al., 2001, ApJ, 562, 303

Drinkwater M. J., Gregg M. D., Holman B. A., Brown M. J. I., 2001, MNRAS, 326, 1076

Durrell P. R., Harris W. E., Geisler D., Pudritz R. E., 1996, AJ, 112, 972

Ellis R. S., 1997, ARA&A, 35, 389

Elmegreen B. G., 1999, APSS, 269, 469

Fall S. M., Frenk C. S., 1985, Rotation and flattening of globular clusters, in IAU Symposium, Vol. 113, Goodman J., Hut P. (eds.), Dynamics of Star Clusters, p. 285

Fall S. M., Rees M. J., 1977, MNRAS, 181, 37P

Fall S. M., Zhang Q., 2001, ApJ, 561, 751

Ferguson H. C., Sandage A., 1990, AJ, 100, 1

Ferrarese L., Côté P., Jordán A., et al., 2006, ApJS, 164, 334

Firth P., Drinkwater M. J., Evstigneeva E. A., et al., 2007, MNRAS, 382, 1342

Forbes D. A., 2005, ApJL, 635, L137

Forbes D. A., Brodie J. P., Grillmair C. J., 1997, AJ, 113, 1652

Forbes D. A., Grillmair C. J., Williger G. M., Elson R. A. W., Brodie J. P., 1998, MNRAS, 293, 325

Freedman W. L., Madore B. F., Gibson B. K., et al., 2001, ApJ, 553, 47

Frenk C. S., Fall S. M., 1982, MNRAS, 199, 565

Gebhardt K., Kissler-Patig M., 1999, AJ, 118, 1526

Geisler D., Hodge P., 1980, ApJ, 242, 66

Georgiev I. Y., Goudfrooij P., Puzia T. H., Hilker M., 2008a, AJ, 135, 1858

Georgiev I. Y., Hilker M., Puzia T. H., et al., 2006, A&A, 452, 141

Georgiev I. Y., Hilker M., Puzia T. H., Goudfrooij P., 2008b, in prep.

Georgiev I. Y., Puzia T. H., Hilker M., Goudfrooij P., 2008c, in prep.

Gieles M., Athanassoula E., Portegies Zwart S. F., 2007, MNRAS, 376, 809

Gieles M., Baumgardt H., 2008, astro-ph/0806.2327, 806

Gieles M., Portegies Zwart S. F., Baumgardt H., et al., 2006, MNRAS, 371, 793

Giersz M., Heggie D. C., 1996, MNRAS, 279, 1037

Glatt K., Gallagher J. S., III, Grebel E. K., et al., 2008, AJ, 135, 1106

Gnedin O. Y., Ostriker J. P., 1997, ApJ, 474, 223

Goodman J., 1984, ApJ, 280, 298

Goudfrooij P., Gilmore D., Whitmore B. C., Schweizer F., 2004, ApJ, 613, L121

Goudfrooij P., Mack J., Kissler-Patig M., Meylan G., Minniti D., 2001, MNRAS, 322, 643

Goudfrooij P., Schweizer F., Gilmore D., Whitmore B. C., 2007, AJ, 133, 2737

Goudfrooij P., Strader J., Brenneman L., et al., 2003, MNRAS, 343, 665

Grebel E. K., Gallagher J. S., III, Harbeck D., 2003, AJ, 125, 1926

Grillmair C. J., 2006, ApJL, 651, L29

Haşegan M., Jordán A., Côté P., et al., 2005, ApJ, 627, 203

Hamuy M., Suntzeff N. B., Heathcote S. R., et al., 1994, PASP, 106, 566

Hamuy M., Walker A. R., Suntzeff N. B., et al., 1992, PASP, 104, 533

Han C., Ryden B. S., 1994, ApJ, 433, 80

Hanes D. A., 1977, MNRAS, 180, 309

Harris W. E., 1991, ARA&A, 29, 543

Harris W. E., 1996, AJ, 112, 1487

Harris W. E., 2001, Globular cluster systems, in Labhardt L., Binggeli B. (eds.), Saas-Fee Advanced Course 28: Star Clusters, p. 223

Harris W. E., 2003, Issues in E Galaxy Formation: Many Problems, Few Solutions, in Kissler-Patig M. (ed.), Extragalactic Globular Cluster Systems, p. 317

Harris W. E., Harris G. L. H., 2002, AJ, 123, 3108

Harris W. E., Harris G. L. H., Barmby P., McLaughlin D. E., Forbes D. A., 2006a, AJ, 132, 2187

Harris W. E., Harris G. L. H., McLaughlin D. E., 1998, AJ, 115, 1801

Harris W. E., van den Bergh S., 1981, AJ, 86, 1627

Harris W. E., Whitmore B. C., Karakla D., et al., 2005, ArXiv Astrophysics e-prints, astro-ph/0508195

Harris W. E., Whitmore B. C., Karakla D., et al., 2006b, ApJ, 636, 90

Heidt J., Appenzeller I., Gabasch A., et al., 2003, A&A, 398, 49

Hénon M., 1965, Annales d'Astrophysique, 28, 62

Hilker M., Bomans D. J., Infante L., Kissler-Patig M., 1997, A&A, 327, 562

Hilker M., Infante L., Richtler T., 1999, A&AS, 138, 55

Hilker M., Richtler T., 2000, A&A, 362, 895

Hughes J., Wallerstein G., 2000, AJ, 119, 1225

Hunter D. A., Elmegreen B. G., 2004, AJ, 128, 2170

Ibata R., Irwin M., Lewis G., Ferguson A. M. N., Tanvir N., 2001, Nature, 412, 49

Ibata R. A., Gilmore G., Irwin M. J., 1994, Nature, 370, 194

James P. A., Shane N. S., Knapen J. H., Etherton J., Percival S. M., 2005, A&A, 429, 851

Jerjen H., Binggeli B., Barazza F. D., 2004, AJ, 127, 771

Jordán A., Côté P., Blakeslee J. P., et al., 2005, ApJ, 634, 1002

Jordán A., McLaughlin D. E., Côté P., et al., 2007, ApJS, 171, 101

Kalirai J. S., Guhathakurta P., Gilbert K. M., et al., 2006, ApJ, 641, 268

Karachentsev I. D., Dolphin A., Tully R. B., et al., 2006, AJ, 131, 1361

Karachentsev I. D., Karachentseva V. E., Huchtmeier W. K., Makarov D. I., 2004, AJ, 127, 2031

Karachentsev I. D., Tully R. B., Dolphin A., et al., 2007, AJ, 133, 504

Kavelaars J. J., 1999, On the Relation Between Globular Cluster Specific Frequency and Galaxy Type, in Astronomical Society of the Pacific Conference Series, Vol. 182, Merritt D. R., Valluri M., Sellwood J. A. (eds.), Galaxy Dynamics - A Rutgers Symposium, p. 437

Khochfar S., Silk J., Windhorst R. A., Ryan R. E., Jr., 2007, ApJL, 668, L115

King I., 1962, AJ, 67, 471

Kissler-Patig M., 2000, Extragalactic Globular Cluster Systems: A new Perspective on Galaxy Formation and Evolution, in Schielicke R. E. (ed.), Reviews in Modern Astronomy, p. 13

Kissler-Patig M., Ashman K. M., Zepf S. E., Freeman K. C., 1999, AJ, 118, 197

Knapen J. H., Stedman S., Bramich D. M., Folkes S. L., Bradley T. R., 2004, A&A, 426, 1135

Koekemoer A. M., Fruchter A. S., Hook R. N., Hack W., 2002, MultiDrizzle: An Integrated Pyraf Script for Registering, Cleaning and Combining Images, in Arribas S., Koekemoer A., Whitmore B. (eds.), The 2002 HST Calibration Workshop, p. 337

Kontizas E., Kontizas M., Sedmak G., Smareglia R., 1989, AJ, 98, 590

Kontizas E., Kontizas M., Sedmak G., Smareglia R., Dapergolas A., 1990, AJ, 100, 425

Kravtsov A. V., Gnedin O. Y., 2005, ApJ, 623, 650

Krist J., Hook R., 2004, "The TinyTim Manual":
, http://www.stsci.edu/software/tinytim/tinytim.html

Kroupa P., Boily C. M., 2002, MNRAS, 336, 1188

Kundu A., Whitmore B. C., 2001, AJ, 121, 2950

Kundu A., Whitmore B. C., Sparks W. B., et al., 1999, ApJ, 513, 733

Lamers H. J. G. L. M., Gieles M., 2006, A&A, 455, L17

Lamers H. J. G. L. M., Gieles M., Portegies Zwart S. F., 2005, A&A, 429, 173

Landolt A. U., 1992, AJ, 104, 340

Laney C. D., Stobie R. S., 1994, MNRAS, 266, 441

Larsen S. S., 1999, A&AS, 139, 393

Larsen S. S., 2006, "An ISHAPE User's Guide":
, http://www.astro.uu.nl/∼larsen/baolab/

Larsen S. S., Brodie J. P., Huchra J. P., Forbes D. A., Grillmair C. J., 2001, AJ, 121, 2974

Lee M. G., Freedman W. L., Madore B. F., 1993, ApJ, 417, 553

Lee Y.-W., Gim H. B., Casetti-Dinescu D. I., 2007, ApJL, 661, L49

Liu C., Hu J., Zhao Y., 2006, astro-ph/0612173

Lotz J. M., Davis M., Faber S. M., et al., 2008, ApJ, 672, 177

Lotz J. M., Miller B. W., Ferguson H. C., 2004, ApJ, 613, 262

Luck R. E., Moffett T. J., Barnes T. G., III, Gieren W. P., 1998, AJ, 115, 605

Mackey A. D., Gilmore G. F., 2003a, MNRAS, 338, 120

Mackey A. D., Gilmore G. F., 2003b, MNRAS, 338, 85

Mackey A. D., Gilmore G. F., 2004, MNRAS, 355, 504

Mackey A. D., van den Bergh S., 2005, MNRAS, 360, 631

Martin N. F., Ibata R. A., Bellazzini M., et al., 2004, MNRAS, 348, 12

Martinez-Delgado D., Penarrubia J., Gabany R. J., et al., 2008, ArXiv e-prints, 805

Mastropietro C., Moore B., Mayer L., et al., 2005, MNRAS, 364, 607

McLaughlin D. E., 1999, AJ, 117, 2398

McLaughlin D. E., 2003, The Globular Cluster Luminosity Function, in Extragalactic Globular Cluster Systems, p. 329

McLaughlin D. E., Fall S. M., 2008, ApJ, 679, 1272

McLaughlin D. E., van der Marel R. P., 2005, ApJS, 161, 304

Meylan G., Heggie D. C., 1997, A&ARv, 8, 1

Mieske S., Jordán A., Côté P., et al., 2006, ApJ, 653, 193

Miller B. W., Lotz J. M., 2007, ApJ, 670, 1074

Miller B. W., Lotz J. M., Ferguson H. C., Stiavelli M., Whitmore B. C., 1998, ApJL, 508, L133

Moore B., Lake G., Katz N., 1998, ApJ, 495, 139

Mori M., Burkert A., 2000, ApJ, 538, 559

Neilsen E. H., Jr., Tsvetanov Z. I., 1999, ApJL, 515, L13

Olsen K. A. G., Miller B. W., Suntzeff N. B., Schommer R. A., Bright J., 2004, AJ, 127, 2674

Ostrov P. G., Forte J. C., Geisler D., 1998, AJ, 116, 2854

Parmentier G., Goodwin S. P., Kroupa P., Baumgardt H., 2008, ApJ, 678, 347

Peng E. W., Jordan A., Cote P., et al., 2005, ArXiv Astrophysics e-prints, astro-ph/0509654

Peng E. W., Jordan A., Cote P., et al., 2008, astro-ph/0803.0330, 803

Piotto G., Bedin L. R., Anderson J., et al., 2007, ApJL, 661, L53

Pipino A., Puzia T. H., Matteucci F., 2007, ApJ, 665, 295

Purcell C. W., Bullock J. S., Zentner A. R., 2007, ApJ, 666, 20

Puzia T. H., Kissler-Patig M., Brodie J. P., Huchra J. P., 1999, AJ, 118, 2734

Puzia T. H., Kissler-Patig M., Thomas D., et al., 2004, A&A, 415, 123

Puzia T. H., Sharina M. E., 2008, ApJ, 674, 909

Puzia T. H., Zepf S. E., Kissler-Patig M., et al., 2002, A&A, 391, 453

Recio-Blanco A., Aparicio A., Piotto G., de Angeli F., Djorgovski S. G., 2006, A&A, 452, 875

Rejkuba M., Dubath P., Minniti D., Meylan G., 2007, A&A, 469, 147

Rhode K. L., Zepf S. E., Santos M. R., 2005, ApJL, 630, L21

Richtler T., 2003, LNP Vol. 635: Stellar Candles for the Extragalactic Distance Scale, 635, 281

Richtler T., Grebel E. K., Domgoergen H., Hilker M., Kissler M., 1992, A&A, 264, 25

Roberts M. S., Haynes M. P., 1994, ARA&A, 32, 115

Robin A. C., Reylé C., Derriére S., Picaud S., 2003, A&A, 409, 523

Ryan R. E. J., Hathi N. P., Cohen S. H., et al., 2007, ApJ, 668, 839

Sandage A., 2005, ARA&A, 43, 581

Schiavon R. P., Rose J. A., Courteau S., MacArthur L. A., 2004, ApJL, 608, L33

Schlegel D. J., Finkbeiner D. P., Davis M., 1998, ApJ, 500, 525

Schweizer F., 1987, Star formation in colliding and merging galaxies, in Faber S. M. (ed.), Nearly Normal Galaxies. From the Planck Time to the Present, p. 18

Schweizer F., 2002, Evolution of Globular Clusters Formed in Mergers, in IAU Symposium, Vol. 207, Geisler D., Grebel E. K., Minniti D. (eds.), Extragalactic Star Clusters, p. 630

Searle L., Zinn R., 1978, ApJ, 225, 357

Seth A., Olsen K., Miller B., Lotz J., Telford R., 2004, AJ, 127, 798

Sharina M. E., Afanasiev V. L., Puzia T. H., 2006, MNRAS, 372, 1259

Sharina M. E., Puzia T. H., Makarov D. I., 2005, A&A, 442, 85

Sirianni M., Jee M. J., Benítez N., et al., 2005, PASP, 117, 1049

Spitler L. R., Larsen S. S., Strader J., et al., 2006, AJ, 132, 1593

Spitzer L., 1987, Dynamical evolution of globular clusters. Princeton, NJ, Princeton University Press, 1987, 191 p.

Spitzer L. J., Thuan T. X., 1972, ApJ, 175, 31

Stetson P. B., 1987, PASP, 99, 191

Stiavelli M., Fall S. M., Panagia N., 2004, ApJ, 600, 508

Strader J., Brodie J. P., Forbes D. A., Beasley M. A., Huchra J. P., 2003, AJ, 125, 1291

Strader J., Brodie J. P., Spitler L., Beasley M. A., 2006, AJ, 132, 2333

Tamura N., Sharples R. M., Arimoto N., et al., 2006, MNRAS, 373, 588

Thomas D., Maraston C., Bender R., 2003, MNRAS, 339, 897

Thomas D., Maraston C., Korn A., 2004, MNRAS, 351, L19

Tully R. B., Rizzi L., Dolphin A. E., et al., 2006, AJ, 132, 729

van den Bergh S., 1993, ApJ, 411, 178

van den Bergh S., 2000a, PASP, 112, 932

van den Bergh S., 2000b, PASP, 112, 932

van den Bergh S., 2006, AJ, 131, 304

van den Bergh S., Mackey A. D., 2004, MNRAS, 354, 713

van Dokkum P. G., 2001, PASP, 113, 1420

Ventura P., D'Antona F., 2008, MNRAS, 255

Vesperini E., 2000, MNRAS, 318, 841

Wehner E., Harris B., Whitmore B., Rothberg B., Woodley K., 2008, astro-ph/0802.1723, 802

West M. J., Côté P., Marzke R. O., Jordán A., 2004, Nature, 427, 31

Whitmore B. C., Schweizer F., 1995, AJ, 109, 960

Worthey G., Faber S. M., Gonzalez J. J., Burstein D., 1994, ApJS, 94, 687

Yahagi H., Bekki K., 2005, MNRAS, 364, L86

Zepf S. E., Ashman K. M., 1993, MNRAS, 264, 611

Zinn R., 1993, The Galactic Halo Cluster Systems: Evidence for Accretion, in Smith G. H., Brodie J. P. (eds.), ASP Conf. Ser. 48: The Globular Cluster-Galaxy Connection, p. 38

Appendix A

Appendix

A.1 List of publications

Refereed papers

Georgiev, I. Y., Goudfrooij, P., Puzia, T. H., Hilker, M., 2008, AJ, 135, 1858 :
"*Old Globular Clusters in Magellanic-type Dwarf Irregular Galaxies*"

Georgiev, I. Y., Hilker, M., Puzia, T. H., Chanamé, J., Mieske, S., Goudfrooij, P., Reisenegger, A., Infante, L. 2006, A&A, 425, 141:
"*The old globular cluster system of the dIrr galaxy NGC 1427A in the Fornax cluster*"

Georgiev, T.B., Georgiev, I.Y., Koleva, N.A., Nedialkov, P.L., Stanchev, O.I. 2005, ARBl[1] 20, 145:
"*Decomposition of the profiles of 20 galaxies*"

Georgiev, T.B., Georgiev, I.Y., Koleva, N.A., Nedialkov, P.L., Stanchev, O.I. 2005, ARBl[1], 20, 138:
"*Analysis of the color-magnitude diagrams of the dwarf galaxies UGCA 105 and UGCA 86*"

Refereed papers in preparation

Georgiev, I. Y., Puzia, T. H., Hilker, M., Goudfrooij, P., 2008:
"*Specific frequencies and structural parameters of old globular clusters from 68 nearby dwarf galaxies*"

Georgiev, I. Y., Hilker, M., Puzia, T. H., Goudfrooij, P., 2008:
"*Nuclear Globular Clusters in Dwarf Irregular Galaxies from HST/ACS imaging*"

Not refereed papers

Georgiev, I., Veltchev, T., Nedialkov, P., Ovcharov, R., Stanev, I., Dyulgerov, Ch.,

[1] Aerospace Research in Bulgaria.

Stanchev, O. 2005, PASRB[2], 4, 167:
"*BVR photometry of the outer regions of the starburst galaxy M82*"

Stanchev, O.I., Nedialkov, P., Georgiev, Ts., Georgiev, I. 2005, PASRB[2], 4, 281:
"*Calibration of diameter-HI line width relation for edge-on spiral galaxies*"

Tzenev, L., Ovcharov, E., Stanev, I., Georgiev, Ts., Georgiev, I., Nedialkov, P., 2004, ATel, 346, 1:
"*Nova in M31*"

Tzenev, L., Georgiev, I., Ovcharov, E., Stanev, I., Kostov, A., Georgiev, Ts., Nedialkov, P., 2004, ATel, 334, 1:
"*Nova in M31*"

Tzenev L., Georgiev, I., Ovcharov, E., Stanev, I., Georgiev, Ts., Nedialkov P., 2004, ATel, 330, 1:
"*Nova in M31*"

[2]Publications of the Astronomical Society "Rudjer Boskovic".